CFD Modelling of Sewage Sludge Vitrification Plant

A Thesis submitted in fulfilment of the requirement for the Degree of a Master in Engineering specialising in Chemical and Process Engineering at the University of Canterbury

Author: David Howey Walker

Department of Chemical and Process Engineering

University of Canterbury

Christchurch, New Zealand

2008

Acknowledgements

I would like to thank my company mentor, Rick Dobbs, Technical Manager, Lemar Environmental Ltd for his support and guidance throughout the past few years. I have gained a lot of knowledge and expertise through working alongside him. He has taught me a lot about being an engineer which has been invaluable. I would also like to thank my two co-supervisors, Associate Professor John Abrahamson, and Ian Gilmour for their ongoing support and guidance during this project.

I would like to thank the Foundation for Research, Science and Technology (FRST) for their Technology for Industry Fellowship (TIF) and the financial assistance they provided me for the project.

I am very grateful for the technical help and ongoing support I received from Tony Allen who was always willing to lend a hand - especially when there were computer problems.

Thank you to all my colleagues in the Department of Chemical and Process Engineering who have made my time here interesting and enjoyable. A special thanks to Nathan Bushnell and John Gabites who continually helped out and assisted with the CFD modelling.

Thank you to June Walter and her mum Beryl Hampson for their accommodation whilst I was in Christchurch. It was always great to come back each night to a warm friendly smile.

A big thanks to my family and friends for putting up with the perpetual student in their midst and offering a welcome break from academic life when needed.

To those I have not named - a big thanks to you too!

CONTENTS

Abstract

This Technology in Industry Fellowship (TIF) funded Masters Project was structured around Computational Fluid Dynamics (CFD) modelling for Lemar Environmental Ltd (Lemar). This study is a component of a larger programme that is being undertaken by Lemar concerning the vitrification process. The modelling has built on an initial model developed by CSIRO for Lemar and has been carried out under the direction of Canterbury University.

The modelling involved computer simulations and detailed comparisons of the gas flow for both high and low swirl vanes, in both the steady state and transient modes. The output of this activity; velocity profiles (tangential and axial), vorticity, as well as particle tracking (in steady state mode only) were compared to literature and evaluated for both scenarios.

As the study was restricted to the gas flow in transient mode, no recommendations and extrapolated modifications to the burner geometry and plant equipment can be made as they have to be verified by the particle motion within the gas flow. The steady state particle simulations obtained through this project, did not provide sufficient evidence to conclude that particles attach to the outer wall and only demonstrated the influences that the high and low swirl had on the particles. Further investigations of transient particle tracking would provide an overall interpretation as to whether or not the dried sludge particles bounced or stuck to the viscous slag layer and a commentary as to their movement in the chamber.

Lemar's strategic vitrification programme is still active and the resulting redesign process is nearing completion and modifications to the plant are expected to be finalised by January 2008. Following extensive testing by Lemar it is understood that they would be looking to seek venture capital in order to progress the project to the market. In order for the final stage of the sewage sludge vitrification plant project to commence, Lemar has been in consultation with subject matter experts in the field, as well as undertaking trials on the plant, computer modelling and research into both the technical and international marketing prospects for the combustion technology.

The detailed analysis and research undertaken through the CFD modelling conducted for this Project, recommends that Lemar conducts further CFD modelling to investigate transient particle tracking before any plant or geometry modifications are proposed and undertaken in order to optimise the ash capture which is a key output of the vitrification process.

1. Introduction

1.1 Background to Study

Waste sludge is a major environmental hazard if not treated effectively. Its treatment and disposal represents a growing global dilemma due to increasingly restrictive legislation and environmental concerns. Sludge originates from the process of treatment of waste water. Due to the physical-chemical processes involved in the treatment, the sludge tends to concentrate heavy metals and poorly biodegradable trace organic compounds as well as potentially pathogenic organisms (viruses, bacteria etc) that are present in waste waters. However, sludge is rich in nutrients such as nitrogen and phosphorous and contains valuable organic matter that is useful when soils are depleted or subject to erosion. The organic matter and nutrients are the two main elements that make the spreading of this kind of waste on land a suitable fertilizer or an organic soil improver.

Lemar Environmental is a small New Zealand company situated on the site of the Kapiti Coast Waste Water Treatment Plant (WWTP), in Paraparaumu, north of Wellington – refer to Figure 1-1. Lemar has been active in effluent treatment, particularly in the wool scouring industry, over the past 25 years. Since 1996 the company has been developing a drying and vitrification process for the treatment of sewage sludge and has built a small plant which they wish to improve and eventually scale up.

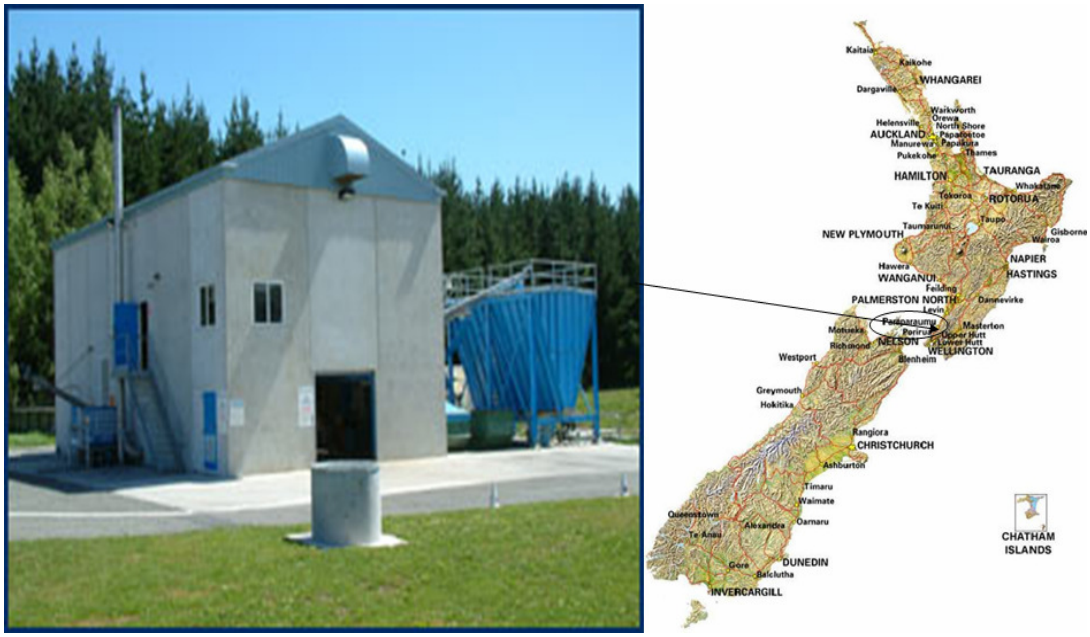

Figure 1-1: Shows the Lemar Environmental Plant (left) and the location in Paraparaumu (right)

The Lemar Environmental treatment for sludge consists of a drying system which incorporates two indirect dryers in series. The primary dryer is designed to take the sludge as a thin film through the sticky plastic phase, without the need for back-mixing and produces free flowing material with a solid content of between 55% and 65% - refer to Figure 1-2 (Dobbs 2003).

Figure 1-2: Shows the primary dryer situated at the Lemar plant (Dobbs 2003)

The dried material then passes into a secondary disc dryer which produces dried sludge with a dry solids content in excess of 93%. At this point, the sludge has been processed at sufficient temperature and residence time to ensure pathogen and bacteria removal. From here the dried sludge can be applied safely to the land as a fertiliser or alternatively the dried sludge can be vitrified.

1.2 The Vitrification Process

Vitrification is the process of converting a material into a glass-like amorphous solid which is free of any crystalline structure, either by the quick removal or addition of heat, or by mixing with an additive. During this process, the majority of contaminants initially present are volatilized, while the remainder are converted into a chemically inert, stable glass product. The high temperatures destroy any organic constituents, resulting in few by-products. Inorganics, such as heavy metals and radionuclides, are actually incorporated into a glass structure which is generally strong, durable and resistant to leaching.

The Lemar sludge vitrification process consists of three combustion chambers - a vertical downward primary chamber, an inclined secondary chamber and a vertical upward separating

chamber. A water slag quench bath is located at the bottom of the separating chamber. Gas exits at the top of the separating chamber passing though a water boiler, an air to air heat exchanger, a venturi scrubber and an ID fan. With the exception of the top section of the primary chamber, the combustion chambers are all water cooled with heat being recovered for use in the drying of the fuel. A schematic of the primary and secondary combustion chambers is shown in Figure 1-3.

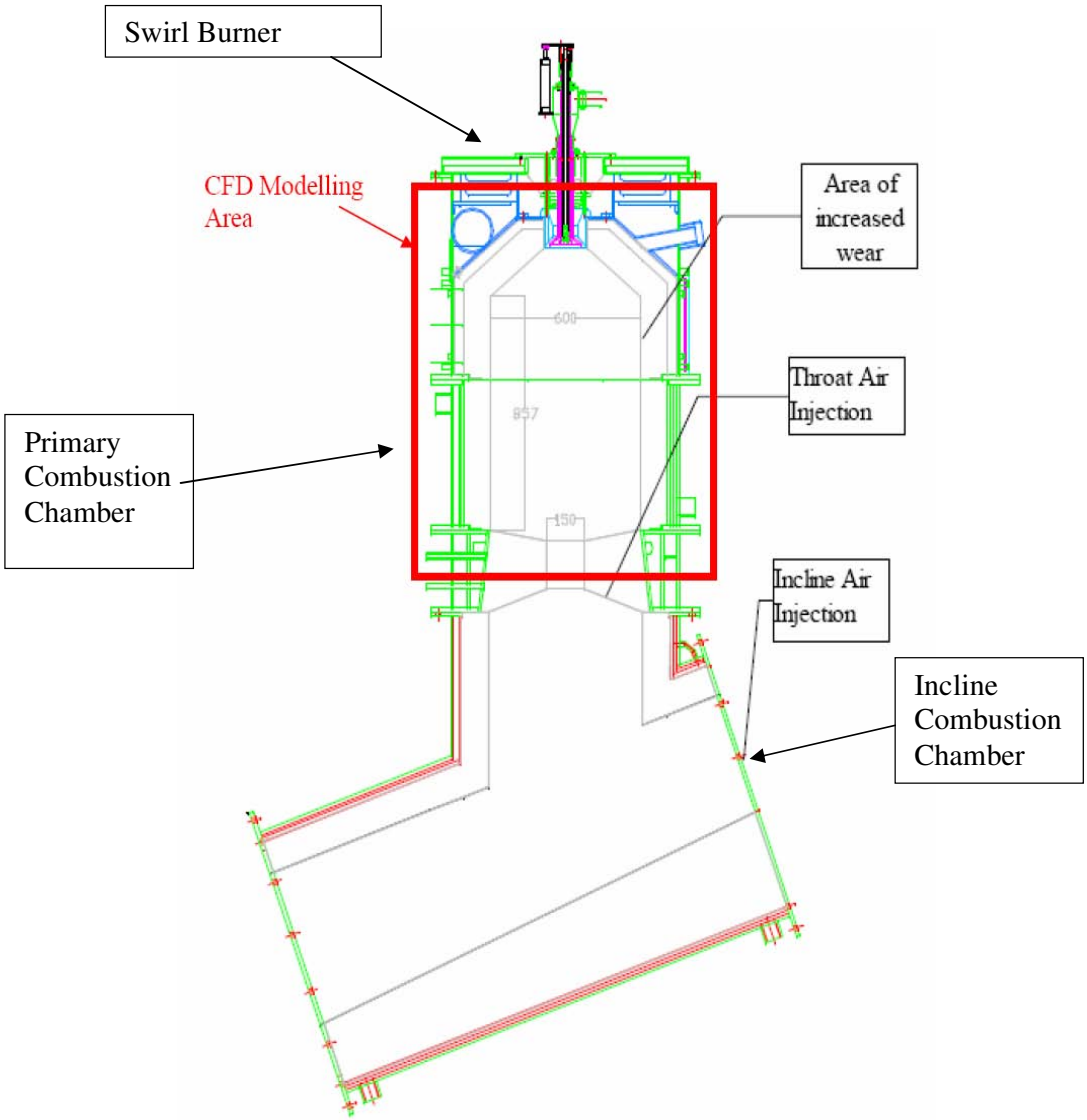

Figure 1-3: Schematic of primary and inclined combustion chambers (Stephens 2006)

Dried sludge passes through a grinder to the vitrification unit where it becomes the only fuel, after auxiliary fuelling (diesel) upon start-up. A vitrification temperature of approximately 1100 °C is maintained by the primary combustion chamber, as well as the incline combustion chamber, to melt the sludge, causing it to fuse and flow through the vitrification process.

In the primary combustion chamber, the dried and treated sludge particles are burnt using a swirl burner of a reasonable conventional design – refer to Figure 1-4. The swirl burner consists of a central auxiliary fuel pipe (used to heat the chamber during start-up), surrounded by an annulus through which the particles are pneumatically injected into the chamber – refer to Figure 1-5. Primary combustion air is injected through an outer annulus after swirl is imparted by a set of vanes. It was intended that the high swirl would cause the particles to be forced out to the sides of the primary chamber where they stick to the molten slag flowing down the sides. The pressure and flow patterns in the primary chamber are maintained by the use of an orifice (throat) through which the molten slag and gas must pass. After passing through the throat, the slag and flue gases flow into a secondary inclined chamber, and finally into a separating chamber where the slag is removed from the gas stream.

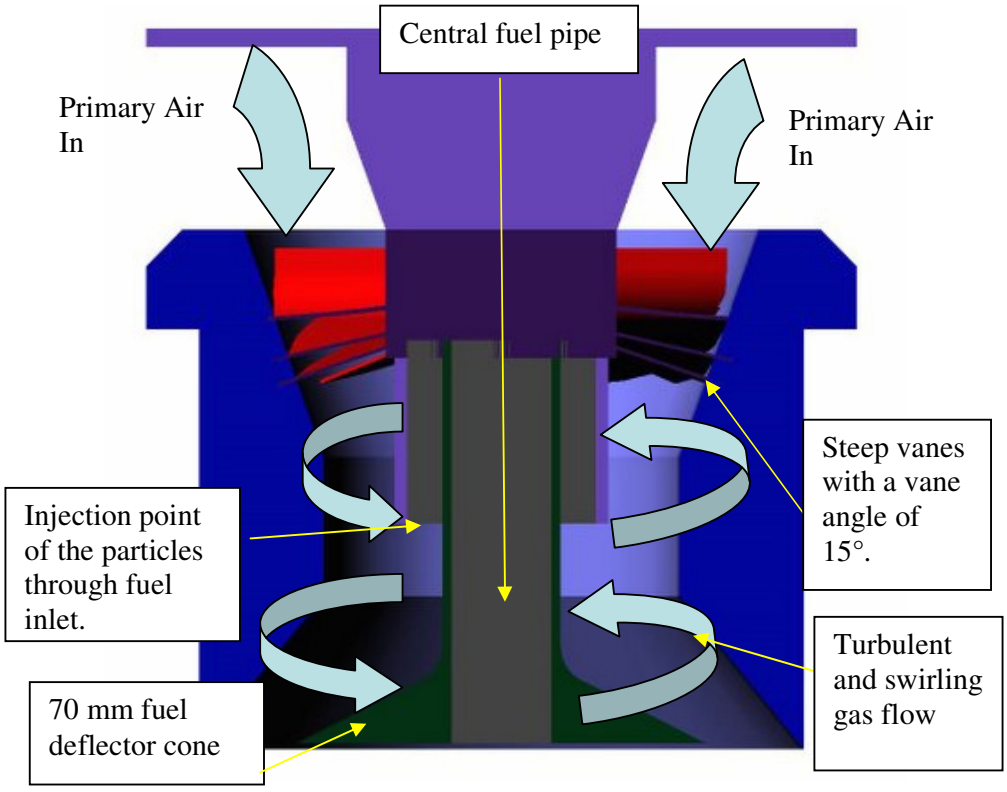

Figure 1-4: A sectioned view of the swirl burner setup and the vanes showing the circulation of the gas after passing through the set of vanes as well as the injection point of the particles

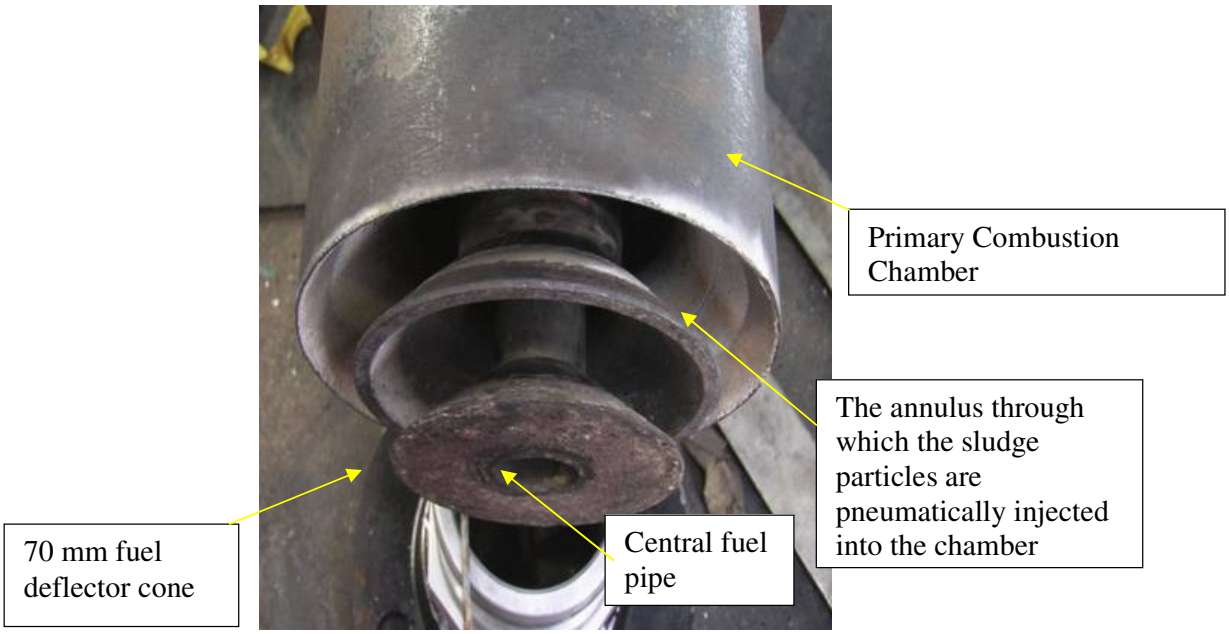

Figure 1-5: A side view of the actual swirl burner setup

From there, the sludge particles melt and flow down as a molten stream which is then water quenched to provide a granular product. The final 'product' is a glassy slag- refer to Figures 1-6 and 1-7.

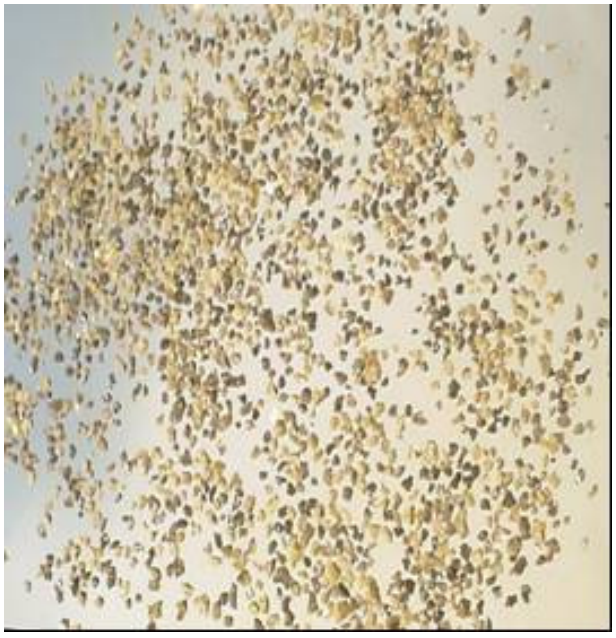

Figure 1-6: A microscopic sample of the slag product (1:1 magnification)

Figure 1-7: Shows the vitrified product travelling up the slag screw

1.3 Masters Project Synopsis

The project involves:

a) Computational Fluid Dynamics (CFD) modeling;
b) The optimisation of a generic swirl burner design for Lemar Environmental Ltd and;
c) Building on a model initially developed by CSIRO Minerals (a combustion research company in Melbourne under contract to Lemar).

Lemar has had some issues around the primary combustion chamber of the vitrification plant i.e. the inefficient capture of the particles in the slag layer, and believes that CFD modelling will be of assistance in allowing them to improve this area of the plant and specifically those parts of the plant immediately downstream, namely the secondary chamber and the separating chamber. It is intended that the CFD model will provide a picture of the swirl flow generated by the burner, and particle motion within the gas flow.

Analysis of the results should indicate possible modifications to the burner geometry or the chamber that should improve capture.

1.4 Assumptions for the Project

A complete description of the system is almost impossible and therefore several assumptions are made as a first approximation to simplify the problem. The following assumptions have been made:

- Particles are spherical.
- There is an absence of particle-particle interactions.
- There is a constant density of the sludge particles (1200 kgm^{-3}) due to no combustion.

2. Computational Fluid Dynamics and Swirl Burner Model

2.1 An Introduction to Computational Fluid Dynamics

Computational Fluid Dynamics (CFD) is a computer-based tool for simulating the behaviour of systems involving fluid flow, heat transfer and other related physical processes. It operates by solving the equations of fluid flow over a region of interest, with specified conditions on the boundary of that region.

Computers are used to perform the millions of calculations required to simulate the interaction of fluids and gases with the complex surfaces used in engineering. However, even with simplified equations and high speed supercomputers, only approximate solutions can be achieved in many cases. More specific codes that can accurately and quickly simulate even complex scenarios such as supersonic or turbulent flows are an ongoing area of research. Computers have been used to solve fluid flow problems for many years. Numerous programs have been written to solve either specific problems, or specific classes of problems. From the mid-1940s the complex mathematics required to generalise the algorithms began to be understood, and general purpose CFD solvers were later developed. These began to appear in the early 1980s and required what were then very powerful computers, as well as an in-depth knowledge of fluid dynamics, and large amounts of time to set up simulations. Consequently, CFD was a tool used almost exclusively in research.

Recent advances in computing power, together with powerful graphics and interactive three-dimensional manipulation of models have made the process of creating a CFD model and analyzing results much less labour intensive, thus reducing time and hence, costs. Advanced solvers contain algorithms which enable robust solutions of the flow field in a reasonable time. As a result of these factors, CFD is now an established industrial design tool.

CFD codes are structured around numerical algorithms that can tackle fluid flow problems. In order to provide easy access to their solving power, all commercial CFD packages include sophisticated user interfaces to input problem parameters and to examine the results. The commercial package used in this Masters Project is called CFX-10.0 from Ansys and the solution method used is the finite volume technique. This technique was originally developed as an implicit finite volume formulation to construct the discrete equations representing the Navier-Stokes equations for fluid flow. The finite volume technique is the easiest to understand and is

the most well-established and validated. When using this technique the region of interest is divided into small sub regions (control volumes) and the partial differential equations are discretised and solved iteratively for each control volume (Versteeg and Malalasekera 1995).

CFX-10.0 is a general purpose commercial CFD package. This code is capable of modelling steady state and transient flow, laminar and turbulent flow, subsonic and supersonic flow, heat transfer and radiation, and multiphase flow. A CFD package generally consists of three components; namely the pre-processor, solver and post-processor – refer to Figure 2-1.

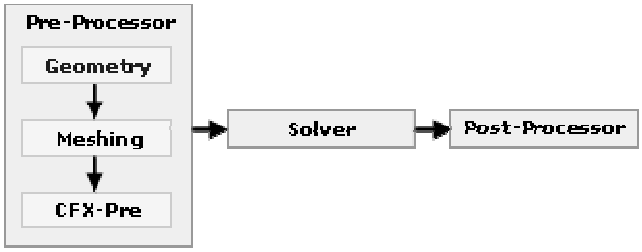

Figure 2-1: Shows the makeup of a CFD package; the pre-processor, solver and post-processor (Anon 2005).

CFX Pre-Processor

Pre-processing consists of the input of a flow problem to a CFD program by means of an operator-friendly interface and the subsequent transformation of this input into a form suitable for use by the solver. The user activities at the pre-processing stage include:

- Definition of the geometry of the region of interest: the computational domain.
- The sub-division of the domain into a number of smaller, non-overlapping sub-domains: a grid (or mesh) of cells (or control volumes or elements).
- Selection of the physical and chemical phenomena that need to be modelled.
- Definition of fluid properties.
- Specification of appropriate boundary conditions of cells which coincide with or touch the domain boundary.

CFX-Solver

Solver produces the required results in a non-interactive/batch process. It solves the CFD problem as follows:

1. The partial differential equations are integrated over all the control volumes in the region of interest. This is equivalent to applying a basic conservation law (e.g. for mass or momentum) to each control volume.
2. These integral equations are converted into a system of algebraic equations by generating a set of approximations for the terms in the integral equations.
3. The algebraic equations are solved iteratively. An iterative approach is required because of the non-linear nature of the equations, and as the solution approaches the exact solution, it is said to converge. For each iteration an error, or residual, is reported as a measure of the overall conservation of the flow properties. How close the final solution is to the exact solution depends on a number of factors, including the size and shape of the control volumes and the size of the final residuals.

Complex physical processes such as combustion and turbulence, are often modelled using empirical relationships. The approximations inherent in these models also contribute to differences between the CFD solution and the real flow. The solution process requires no user interaction and is therefore usually carried out as a batch process. The solver produces a results file which is then passed to the post-processor.

CFX-Post-Processor

The post-processor is the component used to analyse, visualise and present the results interactively. Post-processing includes anything from obtaining point values to complex animated sequences. As in pre-processing a significant amount of development work has recently taken place in the post-processing field. Owing to the increased popularity of engineering workstations, (many of which have outstanding graphics capabilities) the leading CFD packages are now equipped with versatile data visualisation tools. These include:

- Domain geometry and grid display
- Vector plots
- Line and shaded contour plots
- Two-dimensional and three-dimensional surface plots
- Particle tracking

2.2 The Mathematics of CFD

The equations which describe the processes of momentum, heat and mass transfer are partial differential equations which were derived in the early nineteenth century and have no known general analytical solution but which can be discretised and solved numerically. For a compressible Newtonian fluid the respective equations (Versteeg and Malalasekera, 1995) are:

Mass or Continuity Equation	$\frac{\partial \rho}{\partial t} + div(\rho U) = 0$	Equation 2-1
x-momentum	$\frac{\partial(\rho u)}{\partial t} + div(\rho u U) = -\frac{\partial \rho}{\partial x} + div(\mu \, grad u) + S_{Mx}$	Equation 2-2
y-momentum	$\frac{\partial(\rho v)}{\partial t} + div(\rho v U) = -\frac{\partial \rho}{\partial y} + div(\mu \, grad v) + S_{My}$	Equation 2-3
z-momentum	$\frac{\partial(\rho w)}{\partial t} + div(\rho w U) = -\frac{\partial \rho}{\partial z} + div(\mu \, grad w) + S_{Mz}$	Equation 2-4
Internal Energy	$\frac{\partial(\rho i)}{\partial t} + div(\rho i U) = -p \, div(U) + div(k \, grad T) + \phi + S_i$	Equation 2-5

Courtesy of (Versteeg and Malalasekera 1995)

Where ρ= fluid density; t = time; U = velocity vector = $[u,v,w]^T$; u = x-component velocity; v = y-component velocity; w = z-component velocity; μ = dynamic viscosity; S_M = momentum source term in x, y, z direction; i = internal (thermal) energy; p = pressure; k = thermal conductivity; T = temperature; Φ = dissipation function; and S_i = internal energy source term.

The dissipation function is non-negative since it only contains squared terms and represents a source of internal energy due to deformation work on the fluid particle. The work is extracted from the mechanical agency which causes the motion and is converted into internal energy or heat.

If the density ρ is constant, as with incompressible flow, Equation 2-1 reduces to $div(U) = 0$ Equation 2-6.

2.3 CFD Model Description

The commercial CFD code, Ansys CFX-10.0, was used to develop both steady-state and transient simulations. These simulations were isothermal two-phase models of the gas and solid particle flow (dry sludge particles) within the swirl burner and primary chamber. Air properties used for the calculations were taken for air at the isothermal temperature of 240℃, which is the actual combustion air temperature used at Lemar Plant. To determine the gas flow field the model solved conservation equations for mass and momentum using a finite volume method. Transport of the solid particles was achieved through a Lagrangian tracking method.

2.3.1 Gas Phase Model

A gas phase model was developed which is based on the Reynolds Averaged Navier-Stokes equations given below:

$$\nabla.(\rho u) = 0 \qquad \text{Equation 2-7}$$

$$\nabla.(\rho uu) = -\nabla p + \nabla.\mu\nabla u - \nabla(\overline{pu'u'}) \qquad \text{Equation 2-8}$$

where **u** is the gas velocity vector, ρ_{gas} density, p the pressure and μ_{gas} laminar viscosity.

Solution of the above equations by analytical techniques is not possible. CFX-10.0 uses a finite volume method to solve the above equations on an unstructured grid. To avoid chequer-board oscillations in the flow field variables, the Rhie and Chow interpolation procedure is used (Rhie and Chow 1983). Coupling between pressure and velocity in Equation 2-7 and 2-8 is handled implicitly by the coupled solver. The second order accurate "High Resolution Scheme" is used to discretise advection terms in the equations to improve solution accuracy. Density is calculated based on the ideal gas law and is a function of pressure and temperature. In this stage of the work the flow is assumed to be isothermal, hence the temperature is fixed at the primary air temperature (240°C).

2.3.2 Turbulence Model

The turbulence model used in this study was the SSG Reynolds Stress Model – where the differential equations for each component of the Reynolds stress terms were solved to obtain each stress component, thus allowing anisotropy in the turbulent stress tensor. The k-ε model, which is the most widely used turbulence model, was not used in this application because it does not model highly swirled flows (Stephens 2006). The SSG model solves for the turbulence eddy dissipation rate, ε, and the transport of the Reynolds stresses using the following equations:

$$\nabla.\left(\rho u\overline{u'u'}\right)-\nabla.\left(\left(\mu+\frac{2}{3}C_s\rho\frac{k^2}{\varepsilon}\right)\left(\nabla\overline{u'u'}\right)\right)=P+\prod-\frac{2}{3}I\rho\varepsilon \qquad \text{Equation 2-9}$$

$$\nabla.\left(\rho u\varepsilon\right)-\nabla.\left(\mu+\frac{\mu_T}{\sigma_\varepsilon}\right)\nabla\varepsilon=\frac{\varepsilon}{k}\left(C_{\varepsilon 1}P-C_{\varepsilon 2}\rho\varepsilon\right) \qquad \text{Equation 2-10}$$

Π = pressure strain term, and **P** = the shear production term. Logarithmic wall functions are used to capture the steep velocity and shear gradients at the walls.

The six components of the Reynolds stress tensor and the rate of energy dissipation ε are solved using the Reynolds stress transport equation. Since the Reynolds stress tensor is no longer treated as an isotropic tensor, this makes it excellent for anisotropic flows with large streamline curvature (i.e. swirl), rotation, wall jets, round jets, planar jets, asymmetric channel, non-circular ducts and sudden changes in the strain rate (Versteeg and Malalasekera, 1995).

The additional seven transport equations require expensive computational time and storage. Compared to the more advanced eddy-viscosity models (for example the SST turbulence model), little improvements are gained unless there is strong curvature and secondary recirculation regions. Also the Reynolds stress transport model is not as widely validated as the mixing length and k-ε models (Hii 2004).

2.3.3 Solid Particle Model

Within the solid particle transport model, the total flow of the particle phase is modelled by tracking a small number of particles moving through the continuum fluid. The application of Lagrangian tracking involves the integration of particle paths through the discretised domain. Individual particles are tracked from their injection point until they escape the domain or some

integration limit criterion is met. Because each particle is tracked from its injection point to final destination, the tracking procedure is applicable to steady state flow analysis. The particle position is determined through integration of the following equation:

$$\frac{dr_p}{dt} = U_p \qquad \text{Equation 2-11}$$

Where $\mathbf{r_p}$ is the particle position vector and $\mathbf{U_p}$ is the particle velocity vector. The particle velocity vector is determined from a force balance on the particle:

$$m_p \frac{dU_p}{dt} = F_D + F_B \qquad \text{Equation 2-12}$$

where m_p is the mass of a particle, $\mathbf{F_D}$ and $\mathbf{F_B}$ are the body force vectors due to drag and buoyancy respectively. The body force vectors in Equation 2-12 represent the coupling between the particles and the gas. It has been assumed that this coupling is only "one-way" where the influence of the particles on the gas flow is negligible.

2.4 Three-Dimensional Model Geometry

Geometry for the primary chamber was provided by Lemar as a CAD file in IGES format. This geometry was imported into the Ansys Design Modeller to allow for the truncation of the geometry at the throat and for the addition of two two-dimensional regions for use as boundary condition locations. The internal diameter of the primary chamber is 0.6m and the modelled section of the primary chamber is approximately 1.7m including the swirl burner. Figure 2-2 shows the geometry included in the CFD model domain. One of the most common experimental size distribution fits for pulverised solid particles is the Rosin Rammler (Stephens 2006). A Rosin Rammler distribution can be used to determine the distribution of the mass flow amongst particle sizes. The mass fraction below with a given particle diameter, R, is calculated from:

$$R = 1 - \exp\left[-\left(\frac{d}{d_e}\right)^{\gamma}\right] \qquad \text{Equation 2-13}$$

where d is the particle diameter, d_e is a measure of the fineness and γ is the spread parameter, 273 μm and 1.3 respectively. These parameters are then used by CFX-10.0 to calculate a particle diameter for each of the solved particle tracks.

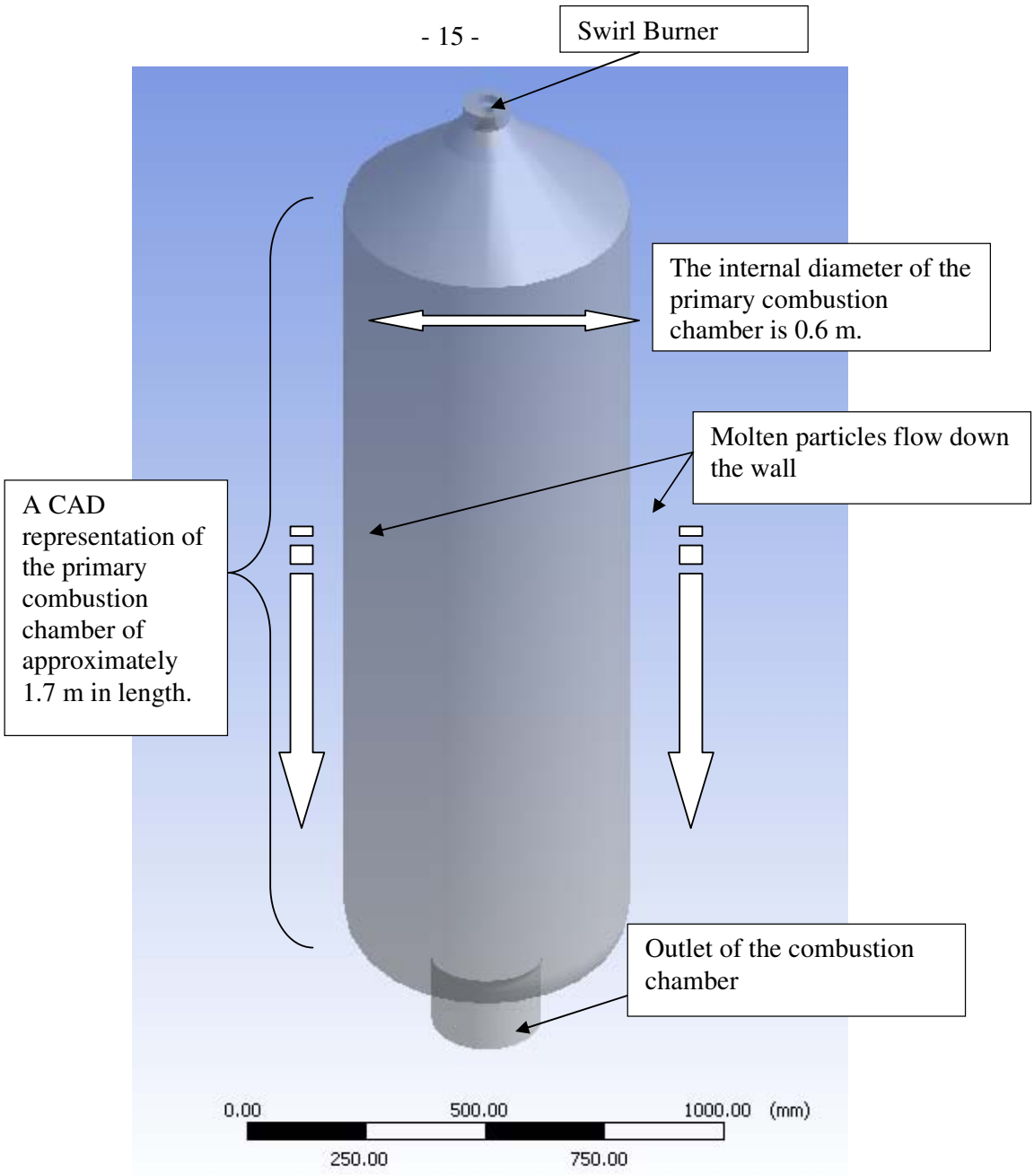

Figure 2-2: A CAD isometric view of the swirl burner setup used in the modelling undertaken at the University of Canterbury

3. Literature Review

The following chapter sets out a brief synopsis of relevant literature, key findings undertaken by other research personnel that impacts and influences the approach taken with this thesis.

3.1 Theory behind the Velocity Profiles

The velocity profile in a swirl burner setup is usually resolved into cylindrical components in the tangential, axial and radial directions. From past experimentation and through research conducted by Wakelin (1993), it has been found that the tangential component is the most dominant, as it often rises to nearly twice the inlet velocity away from the walls and the axis. The axial velocity in the swirl chambers is of the order of one half of the inlet velocity.

The tangential velocity profile is generally discussed in terms of a **forced vortex** (rigid body rotation) and a **free vortex** (potential vortex) – refer to Figure 3-1. Forced vortex flow is deemed a subset of rotational flow. Free vortex flow, which approximately describes the motion in tornadoes and whirl pools away from the core, is classified as an example of irrotational flow (Wakelin, 1993).

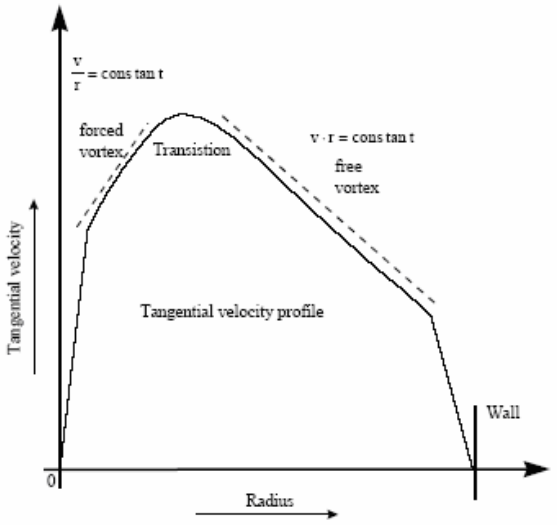

Figure 3-1: Illustration of how the tangential velocity profile consists of both a free and forced vortex swirl

The mean tangential velocity in the flow field tends to zero at the axis of symmetry. Hence, solid-body rotation necessarily exists in the centreline region. The two vortex distributions, patched together, form a resultant profile known as the Rankine vortex.

3.2 Background to Ash Deposition on a Furnace Wall

A range of operations in the chemical, pharmaceutical, food, agricultural, manufacturing and power industries involve the processing and transportation of particles; and within many systems particle impaction plays a major part in determining particle motion and hence, the overall system performance. Therefore, an understanding of particle impact behaviour is rapidly increasing in importance as industries attempt to improve quality, efficiency and production rates (Miles, Baxter et al. 1995).

Ash particle accumulations on the walls occur via transport of particles to the refractory or heat-transfer surface and sticking of the particles. In a slagging combustor, the suspension combustion, particle deposition, and wall burning will take place in a certain position near the wall. The ash products form a slag layer, which flows down the refractory wall under gravity and out the bottom of the combustor into a water quenching system. Maintaining slag flow in cyclone-fired combustion systems is critical and is dependent on the viscosity that in turn is dependent upon the slag chemical composition and temperatures (Miles, Baxter et al. 1995).

The decrease or increase of ash deposition will change the wall boundary conditions and affect the heat transfer through the wall and the burning characteristics in the combustor. Many researchers have carried out studies on ash deposition during the past few decades – these people include (Wang and Harb, 1997) and (Davis, Rager et al. 2002) who developed models for the prediction of the deposition behaviour of fly-ash. Wang and Harb (1997) discovered that the fraction of impacting ash particles that stick to the surface is determined from the physical characteristics (viscosity) of both the particles and the deposit surface. The model that was developed included a description of the ash deposit growth which approximated both the physical properties and chemistry of the deposit as a function of combustion conditions (operating conditions). A key feature of the model was its ability to account for the effect of deposition on operating conditions in the boiler.

(Wang, Zhao et al. 2007) identified that if the temperature in a slagging combustor or furnace was high enough, the coal slag will melt and the molten layer will capture the particles more

effectively. If these particles contained combustible matter, they would continue to burn and flow with the running slag, which makes the total amount of ash deposition greater.

3.3 Background to Types of Particle-Wall Interactions

Particle-wall interactions have to be considered in any modelling of flow of particles in a cyclone or combustor. Particle-wall interactions can be in three forms - particle bouncing from a wall and the sticking and sliding of particles along the wall.

The parallel and perpendicular restitution coefficients describe the action of particles when they hit the wall. Coefficient values of one describe an elastic collision (i.e. particle bounce), while values less than one describe an inelastic collision. The parallel coefficient of restitution will almost always be one and the perpendicular coefficient will depend on the particle material (Anon 2005).

Particle bounce phenomena were investigated with respect to bounce of a model particle, limitations on dust collection (back mixing), and energy loss during the flow of suspensions by Ranz, Talandis et al, 1960. They discovered that particle bouncing occurs when there is an energy interchange between the particle and the surface (inelastic bounce) and between the translational and rotational energies of the particle.

Irregular particles bounce with randomly distributed angles of reflection. There is an increased probability that a particle striking at a low angle will bounce at a high angle and be carried far out into the main fluid flow. Much work has been undertaken on the mechanics of particle bounce from a surface. Ranz, Talandis et al (1960) used irregularly shaped ping-pong balls to demonstrate the bounce characteristics of irregularly shaped particles. They impacted five representative shapes of ping-pong balls at a constant incidence angle and measured the distribution of the angle of reflection. The angle of incidence and reflections were measured from the normal to the particle velocity vector before and after collision respectively. Later the incident angles were varied and the process repeated. Their results identified that particles striking at a low angle increased the probability that the particles would bounce off at a high angle.

For an angle of incidence of α', the reflection was α". The velocity after impact is a function of the elasticity of the bounce, the irregularity of the particle, and the friction encountered with the wall (Ranz, Talandis et al. 1960).

A simple diagram can represent the collisions of the particles with the walls of the cyclone or combustor in two dimensions as shown in Figure 3-2. In practical experimentation the wall is curved and has surface imperfections but for the purposes of this example it has been assumed to be both linear and smooth.

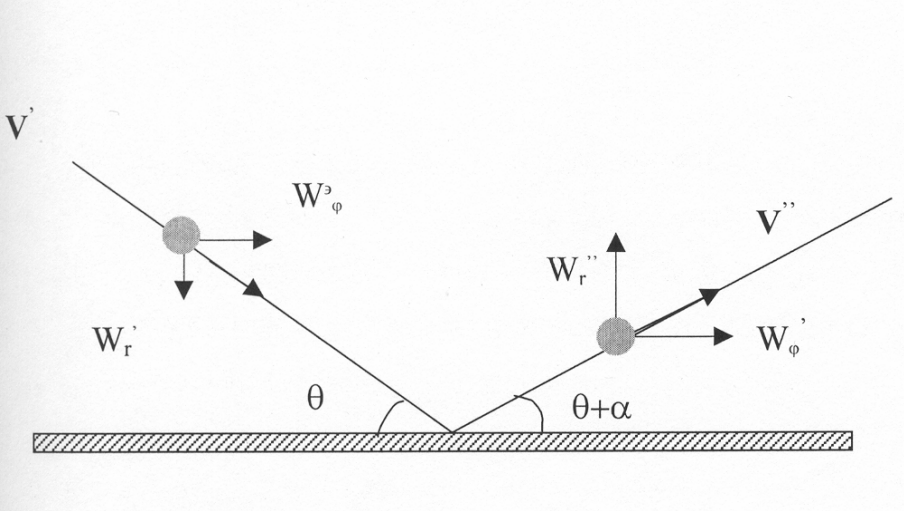

Figure 3-2: Particle Collision with a Cyclone Wall (Saruchera 1998)

The coefficient of restitution is given by:

$$W_r^{'} = \varepsilon W_r^{'} \qquad \textbf{Equation 3-1}$$

Where $W_r"$ is the velocity component in the radial direction and W_φ is in the tangential direction, α' and α" are the incident and reflected angles respectively. The magnitude of $W_r"$ affects the trajectory of the particle. For a particle whose collision with the wall is highly inelastic, the reflected velocity in the radial direction will be reduced and an increase of $W_r"$ will result in a slight increase in the coefficient of restitution. A low reflected angle would also cause the particle to stay close to the wall. It is important to note that the incident and reflected angles are also influenced by the particle shape factor. On the point of contact of the particle with the wall, a frictional force will act in the tangential direction.

When inelastic deformation occurs, (for example plastic flow, densification, fracture or visco-elastic effects), the normal coefficient of restitution will be less than one. Particles that stick to

the wall (e.g. water droplets or molten sludge particles) will have a perpendicular coefficient of zero (Anon 2005).

3.4 Background to the Mechanics of Small Particles Colliding with a Wet Surface

Davis, Rager et al. (2002) conducted experiments to measure the rebound velocities of small plastic nylon balls and stainless steel metal spheres impacting onto a smooth quartz surface coated with a thin layer of viscous fluid. The purpose of their study was to determine the apparent coefficient of restitution and how it depends on fluid and solid properties. It was identified that low impact velocity spheres adhered without rebounding, due to viscous dissipation in the thin fluid layer. The two fluids used by Davis, Rager et al were silicon-based oil with viscosities of 0.99 and 12.5 Pa.s and at 23 °C. For most experiments, an oil thickness of 80, 150 or 250 μm was used. Above a critical impact velocity, the lubrication forces in the thin layer caused elastic deformation and rebounding of the spheres. Davis, Rager et al identified that the apparent coefficient of restitution increased with the ratio of the Stokes number (St) to its critical value (St_c) for rebound, where the Stokes number is a dimensionless ratio of the inertia of the sphere to viscous forces in the fluid. Davis et al. (1986) showed that the collision and rebound process is governed by two dimensionless parameters:

Stokes number: $St = mv_o /(6\pi\mu a^2)$ **Equation 3-2**

Elasticity parameter: $\varepsilon = 4\theta\mu v_o a^{3/2} / x_o^{5/2}$ **Equation 3-3**

Where $m = 4\pi a^3 \rho_s / 3$, is the mass of the particle, a is its radius, ρ_s is its density, μ is the fluid viscosity, v_o is the impact velocity of the particle when starting at a separation Xo between the surfaces, $\theta = (1 - v_1^2)/(\pi E_1) + (1 - v_2^2)/(\pi E_2)$, and v_i and E_i are Poisson's ratio and the Young's modulus of elasticity for the ball (i = 1) and plane (i = 2).

Davis et al. (1986) showed that no rebound of the particle occurred when the Stokes number was less than a critical value ($St < St_c$), due to viscous dissipation of the initial kinetic energy of the sphere. Rebound was predicted for $St > St_c$. Gondret et al (2002), and Joseph et al (2001) discovered that no rebound of spheres occurred for Stokes numbers below a critical value of St_c of approximately 10.

3.5 Background to Turbulent Swirling Flows

Turbulent swirling flows are encountered in many chemical engineering applications and are highly three dimensional, unsteady and particularly complex. Swirling flows in both reacting and non-reacting conditions occur in a wide range of applications such as in gas turbine engines, diesel engines, industrial burners, and boilers.

Over the last decade, attention has focused on numerical predictions, but today due to the advent of fast digital computers, CFD studies are increasingly becoming an integral part of the design methodologies.

Swirling flows were originally used to improve and control the mixing rate between fuel and oxidant streams in order to achieve flame geometries and heat release rates appropriate to the particular process application (Weber et al, 1986). At a sufficient degree of swirl, an internal recirculation zone is generated which allows a high rate of heat release, as products of combustion are recirculated and ignite the incoming fuel streams. This provides a stable, compact flame (Swithenbank et al, 1969), with a good performance for difficult carboneous materials and poor quality gases (Syred and Beer, 1974).

For a swirling flow, the characteristics of the flow structures are dependent on two dimensionless parameters; the Reynolds number ***(Re)***, and the swirl number ***(S)***. The swirl number is defined as the ratio of the axial flux of momentum to the axial flux of axial momentum times the equivalent exit radius, and has been shown to have large-scale effects on flow fields (Gupta et al, 1984).

The basic characteristic of a weak swirl ($S < 0.3$) is to increase the width of a free or confined jet flow but not to develop any axial recirculation. This is due to low axial pressure gradients, whereas a strong swirl ($S > 0.6$) develops strong axial and radial pressure gradients, which assists in the formation of a recirculation zone (Ganesan, 1974). The recirculation zone geometry is a direct function of the swirl number (Huang and Tsai, 2001).

Turbulent swirling flows are invariably associated with two flow phenomena: ***vortex breakdown*** and ***precessing vortex core (PVC).***

Vortex breakdown is defined as an abrupt flow transition that occurs when the swirl intensity exceeds a critical value and it is characterised by a wave-like velocity profile with a stagnation point, followed by flow reversal. Vortex breakdown has been the subject of many experimental, numerical and theoretical investigations and has been reviewed extensively in literature (Hall, 1972; Leibovich, 1978; Escudier, 1987; Shtern and Hussain, 1999; Lucca-Negro and O'Doherty, 2001). Various mechanisms on the occurrence of vortex breakdown have been proposed and different types have been identified. Two forms seem to be predominant in turbulent flows, the ***axisymmetric or bubble breakdown*** and the ***spiral*** form. A number of researchers, such as Harvey (1962) and Sarpkaya (1971), have shown that the simplest first breakdown of a vortex takes the form of an axisymmetric bubble of circulating fluid. Initially this occurs several exit diameters downstream of the flow exit. The flow then re-establishes itself before finally breaking down into a spiral form, which is again symmetrical about the central axis. Sarpkaya (1971) also showed that this first stage of breakdown of a vortex may be helical in nature, forming a double helix.

Vortex breakdown can often be not only asymmetric, but also highly time dependent (Vonnegut, 1954), (Chanaud, 1965), (Syred and Beer, 1972), (O'Doherty et al, 1998) – refer to Figure 3-3. This is the result of the forced vortex region of the flow becoming unstable and starting to precess about the axis of symmetry thus forming a **'precessing vortex core' or PVC** (Syred and Beer, 1972). Syred and Beer (1972) found that the PVC lies on the boundary of the reverse flow zone between the zero velocity and zero streamline. Subsequent work has shown that the presence of a PVC distorts the reverse flow zone into a `kidney shape' which can lag behind the precessional centre of the vortex by up to 180° (Syred et al, 1997). Lucca-Negro (1999) showed that the reverse flow zone finally becomes shaped by the PVC forming a helical bubble.

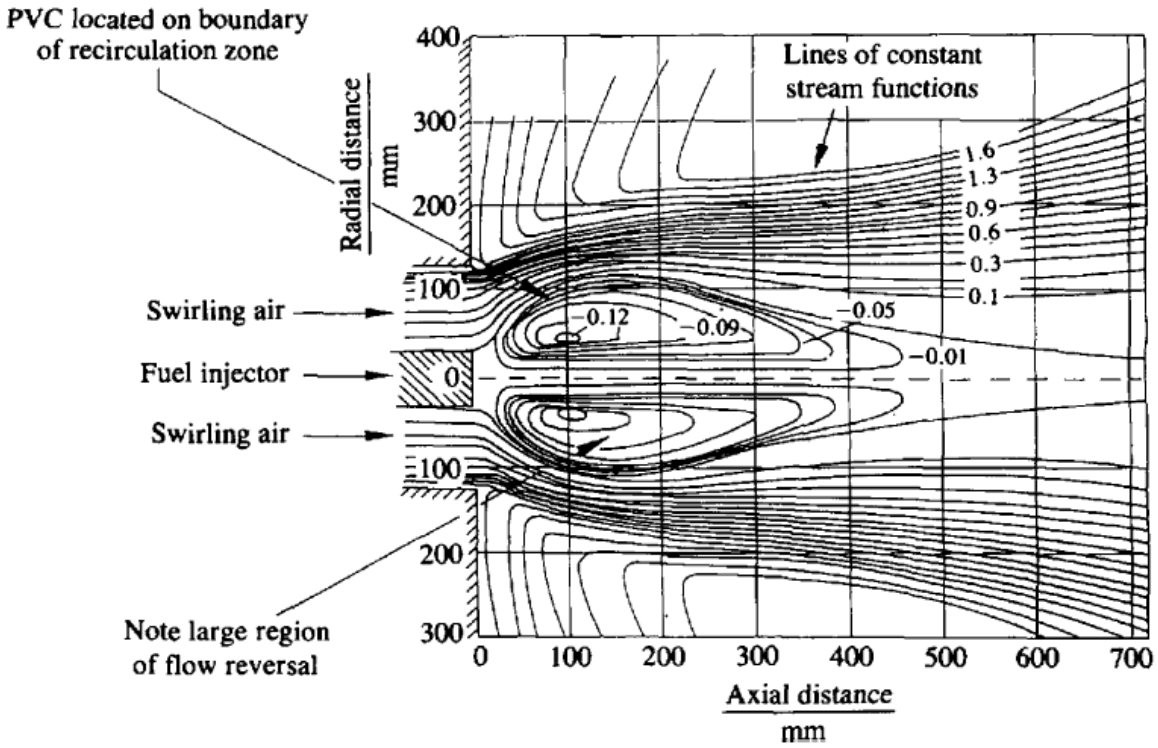

Figure 3-3 Stream function distribution at swirl burner exhaust showing typical recirculation zone set up in the exhaust of a swirl burner and isothermal conditions. PVC is located on the boundary of the reverse flow zone (Syred et al, 1997).

The existence of PVC has been observed within combustors and dust separation systems. While studies indicate that there may be a potential benefit in including PVC in combustion systems, this has been found to be detrimental in cyclone dust separators (O'Doherty et al, 1998). Despite the extensive experimental, numerical and theoretical research undertaken, the phenomenon of vortex breakdown remains controversial and no unequivocal explanation has emerged to date.

Characterising turbulent and swirling flows remains a challenge in fluid mechanics and a large selection of literature has been published dealing with various flow configurations (confined and unconfined, reacting and non-reacting) and/or specific phenomena such as flow structure and instabilities, flow precession and vortex breakdown. A comprehensive amount of related literature on swirl flows can be found in literature by Gupta et al, 1984.

4. Grid Independence Study

The Grid Independence Study was undertaken to prove grid independence for the high and low swirl steady state results. Three grid independence studies were undertaken and are discussed in the following sections:

Section 4.1

- 70 mm fuel-deflector cone with high swirl vanes (H 70 series)

Section 4.2

- 70 mm fuel-deflector cone with low swirl vanes (L 70 series)

Section 4.3

- 100 mm fuel-deflector cone with high swirl vanes (recreation of CSIRO's model) (H 100 series)

The mesh building code ICEM CFD HEXA was used for the unstructured meshing of the primary combustion chamber and swirl burner.

4.1 70 mm Fuel-Deflector Cone with High Swirl Vanes (H 70 series)

A mesh independence study was undertaken for a working mesh labelled the 'High Swirl Current Mesh'. This mesh had 2,298,392 elements, corresponding to 702,261 nodes. For grid independence purposes, two other meshes were created for comparison, one with more elements and nodes – 'High Swirl Fine Mesh', and the other with less elements and nodes – 'High Swirl Coarse Mesh'. The mesh referred to as 'High Swirl Fine Mesh' contained 3,389,703 elements corresponding to 1,114,290 nodes, whilst the mesh referred to as 'High Swirl Coarse Mesh' contained 1,763,015 elements corresponding to 586,136 nodes. Table 4-1 shows the mesh statistics for the H 70 series modelling.

Table 4-1: Shows the mesh statistics for the H 70 series modelling

	H 70 Coarse Mesh	H 70 Current Mesh	H 70 Fine Mesh
Tetrahedral elements	1,763,015	2,298,392	3,389,703
Nodes	586,136	702,261	1,114,290

To check mesh independence two lines in CFX-Post were created on the three respective meshes at consistent arbitrary points. Line 1 was created in the section of the swirl vanes in the high velocity region, and Line 2 was created in the main primary combustion chamber. Line 1 went

horizontally through the centreline to each vertical wall of the swirl vane section and had an axial position of 155 mm from the top of the chamber - refer to Figure 4-1. Line 2 went horizontally through the centreline to each vertical wall of the primary combustion chamber and had an axial position of 389 mm from the top of the chamber - refer to Figure 4-1. From here, axial velocity profiles were created and obtained in CFX-Post and exported as .csv files into Microsoft Excel, where the following graphs were created – refer to Figures 4-2 and 4-3.

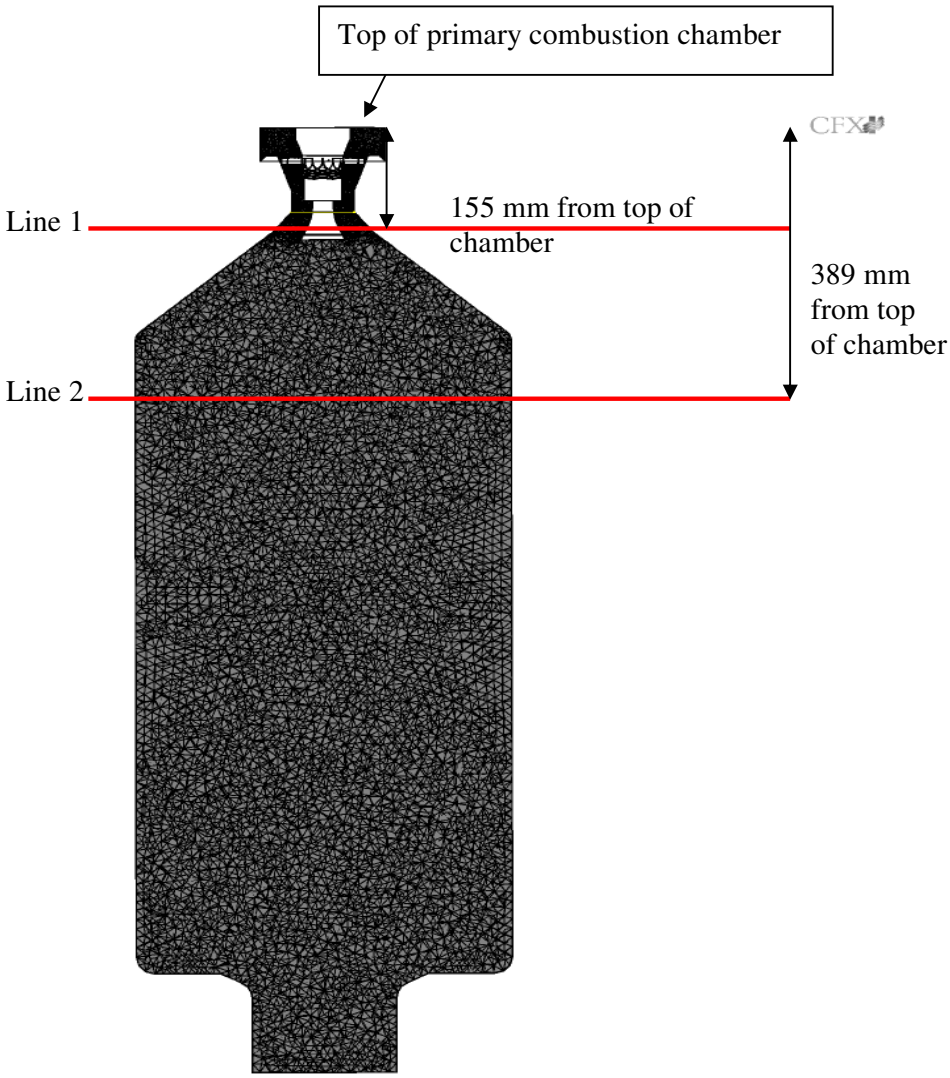

Figure 4-1: Shows the two lines created in CFX-Post. Line 1 had an axial position of 155 mm from the top of the chamber in the swirl vane section and Line 2 had an axial position of 389 mm from the top of the chamber in the main primary combustion chamber.

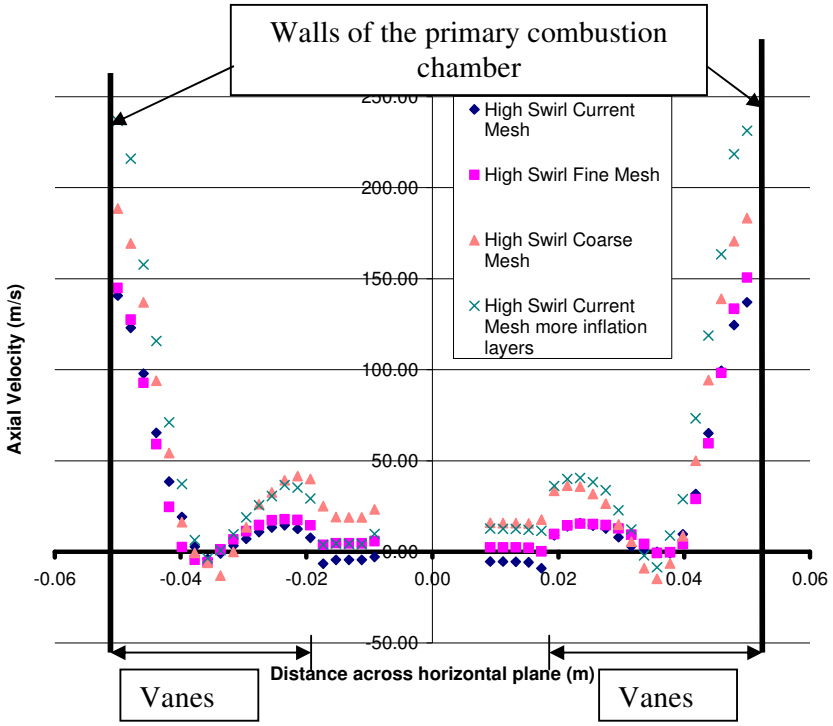

Figure 4-2: Graph showing the axial velocity profiles across Line 1

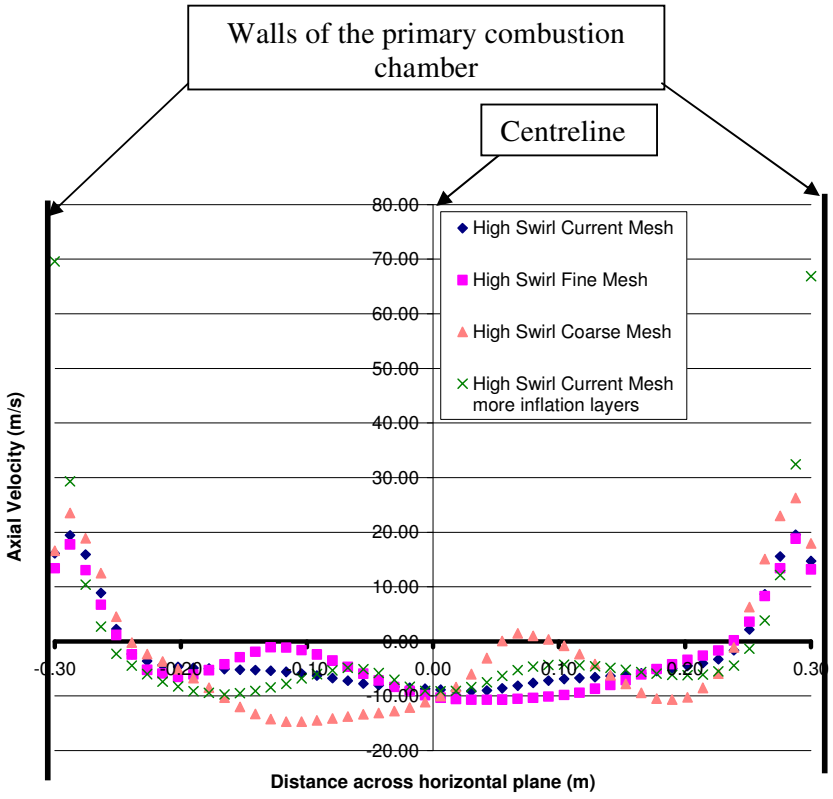

Figure 4-3: Graph showing the axial velocity profiles across Line 2

4.1.1 Swirl Region – Line 1

Figure 4-2 indicates that the axial velocity profiles in the swirler region of the chamber are similar in shape. All profiles are symmetric and uniform with no distorted or skewed profiles. The profiles have five inflation layers nearest the wall except for the 'High Swirl Current Mesh more inflation layers' which has seven inflation layers. The profile of the 'High Swirl Current Mesh more inflation layers' shows a velocity of approximately 225 m/s nearest the outer wall which is the largest of all the profiles. This depicts a more accurate solution because of these extra two inflation layers. The 'High Swirl Fine Mesh' and the 'High Swirl Current Mesh' have similar profiles and are similar to each other except near the 70 mm fuel-deflector cone. Near the wall the axial velocities are large and the 'High Swirl Fine Mesh' and the 'High Swirl Current Mesh' profiles are a 'match' in this region with velocities of approximately 140 m/s, which illustrates that the two meshes are well refined and that an accurate solution was generated.

4.1.2 Primary Combustion Chamber – Line 2

Figure 4-3 illustrates the axial velocity profiles for the four meshes in the primary combustion chamber. The profiles are non-symmetrical over the chamber and the profiles are slightly skewed. The shapes of the profiles are very similar in the range from 0.7R to 1R where R is the radius of the chamber. However nearest the wall on both sides of the graphs the mesh referred to as 'High Swirl Current Mesh more inflation layers' does not dip from the high velocity of 70 m/s unlike the other mesh profiles.

4.2 70 mm Fuel-Deflector Cone with Low Swirl Vanes (L 70 series)

In this second grid independence study, two meshes were created and modelled in CFX-10.0. The working mesh in this study was labelled the 'Low Swirl Current Mesh'. This working mesh had 1,655,086 elements, corresponding to 560,220 nodes – refer to Figure 4-4. The other mesh created, was referred to as 'Low Swirl Fine Mesh'. This contained 2,130,003 elements corresponding to 722,850 nodes. Table 4-2 shows the mesh statistics for the L 70 series modelling.

Table 4-2: Shows the mesh statistics for the L 70 series modelling

	L 70 current mesh	L 70 fine mesh
Tetrahedral elements	1,655,086	2,130,003
Nodes	560,220	722,850

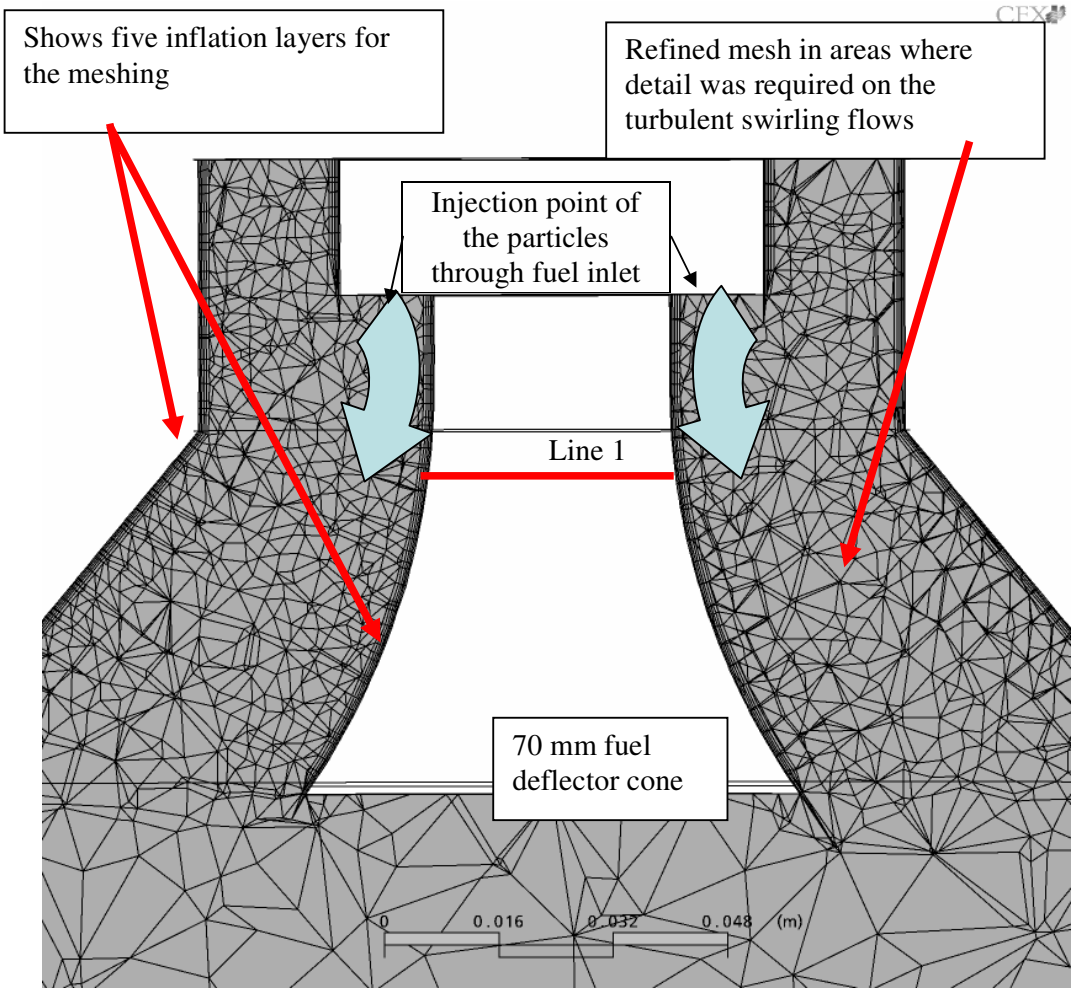

Figure 4-4: Shows the meshing on the outside of the fuel deflector cone as well as the inserted inflation layers for the 'Low Swirl Current Mesh'.

To prove mesh independence, two lines in CFX-Post were created on three respective meshes at consistent arbitrary points. Lines 1 and 2 were created (same as the H 70 series) – refer to Figure 4-5. From here, axial velocity profiles were created and obtained in CFX-Post and exported as .csv files into Microsoft Excel, where the following graph was created – refer to Figures 4-6 and 4-7.

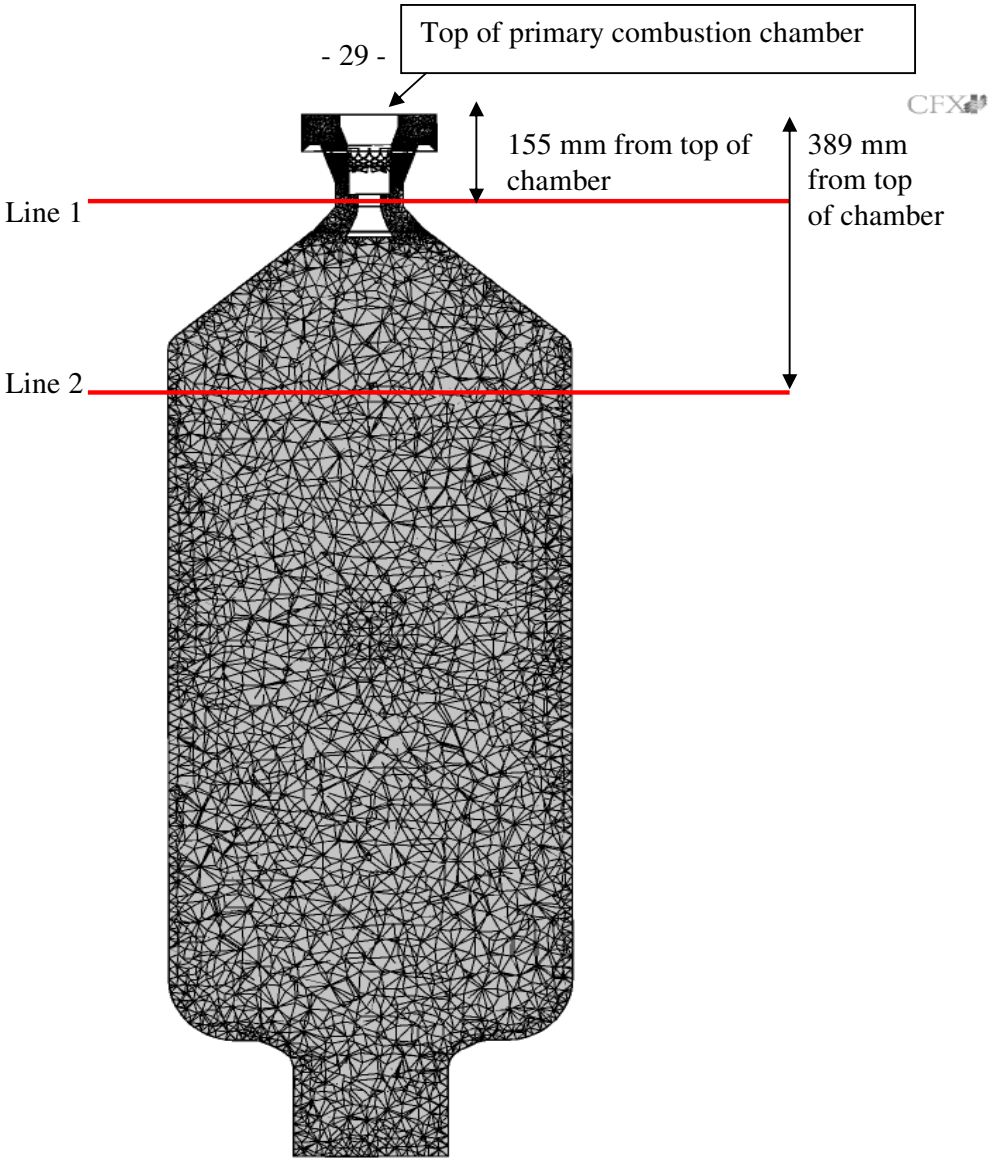

Figure 4-5: Shows the two lines created in CFX-Post. Line 1 is 155 mm from the top of the chamber in the swirl vane section and Line 2 is 389 mm from the top of the chamber in the main primary combustion chamber.

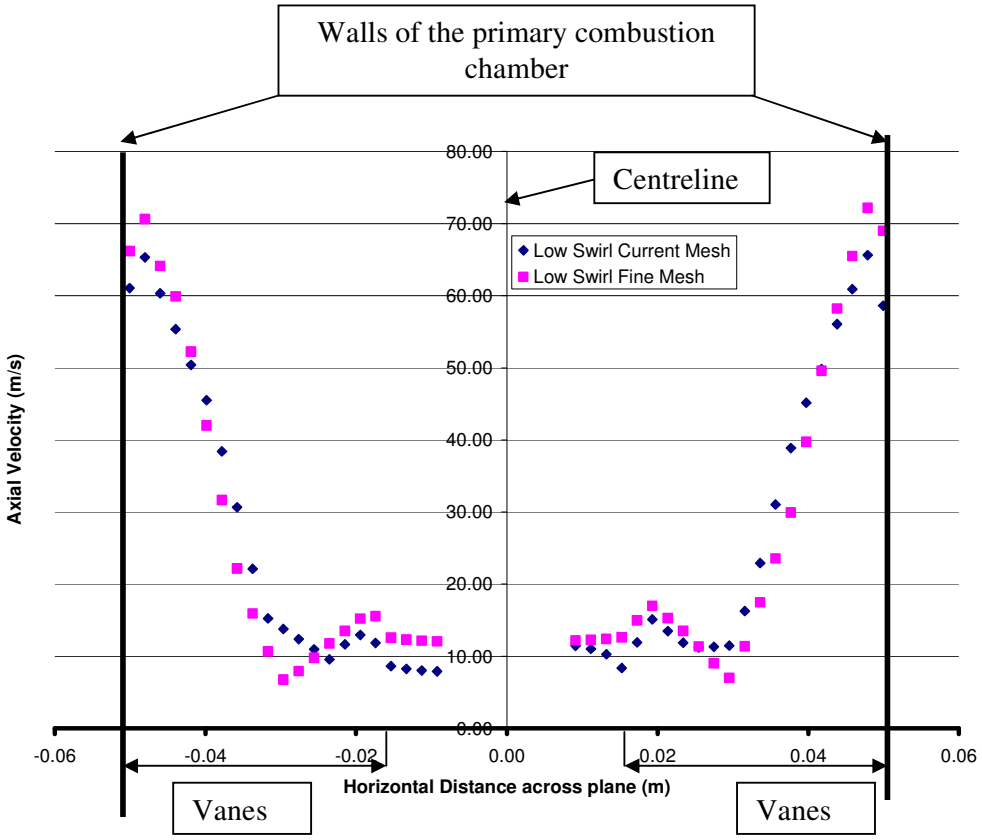

Figure 4-6: Graph showing the axial velocity profiles across Line 1 created for the two respective meshes.

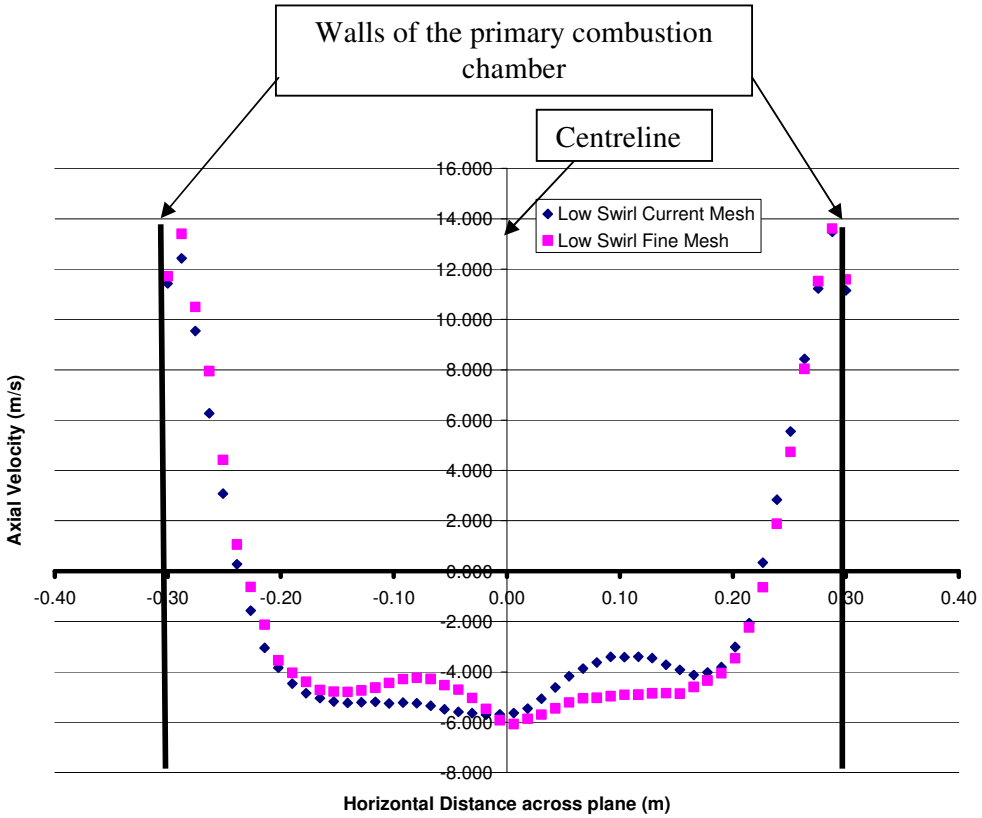

Figure 4-7: Graph showing the axial velocity profiles across Line 2 created for the two respective meshes.

4.2.1 Swirl Region – Line 1

The mesh referred to as 'Low Swirl Fine Mesh' effectively represents the 'Low Swirl Current Mesh'. Both meshes are very similar and have similar axial velocity plots; thus proving mesh independence in this region. The 'Low Swirl Fine Mesh' depicts higher velocities at the wall (approximately 70 m/s) compared to the 'Low Swirl Current Mesh' (approximately 65 m/s).

4.2.2 Primary Combustion Chamber- Line 2

The axial velocity profiles for both meshes in the primary combustion chamber are shown in Figure 4-7. In the outer third of the chamber radius the two meshes are matching one another. Both meshes dip in value near the wall; however between -0.2 m and 0.2 m there is some dissimilarity between the 'Low Swirl Current Mesh' and the 'Low Swirl Fine Mesh'.

4.3 100 mm Fuel-Deflector Cone with High Swirl Vanes (recreation of CSIRO's model) (H 100 series)

This case study builds on the CFD model initially developed by CSIRO Minerals, a combustion research company in Melbourne under contract to Lemar. The aim of this study was to evaluate the velocity profile plots of the tangential and axial velocities from the CSIRO model against a recreated model. To undertake this, velocity profiles within a 60 mm diameter annulus, 100 mm downstream of the swirl vanes were compared to verify the results obtained from CSIRO. CSIRO commenced their work on 30 January 2006 at the request of Lemar Environmental Limited. Lemar's objective in commissioning this project was to undertake Stage 1 in the development of a CFD model for predicting the behaviour in the primary combustion chamber.

4.3.1 CSIRO's CFD Model

The commercial CFD code, Ansys CFX-10.0, was used to develop a steady state isothermal two-phase model of the gas and solid particle flow (sludge particles) within the swirl burner and primary chamber. Air properties used for the calculations were taken for the isothermal temperature of 240°C. The turbulence model used in this study was the SSG Reynolds Stress Model and this was chosen by CSIRO. For the CSIRO model a total of approximately three and half million tetrahedron elements were used to represent the swirl burner, vanes and the primary chamber. The CFD model created in this present study for comparison used the same data and variables but only contained two and half million elements, corresponding to one hundred

thousand nodes. Figure 4-8 illustrates a CAD schematic of the annular geometry for the recreated model.

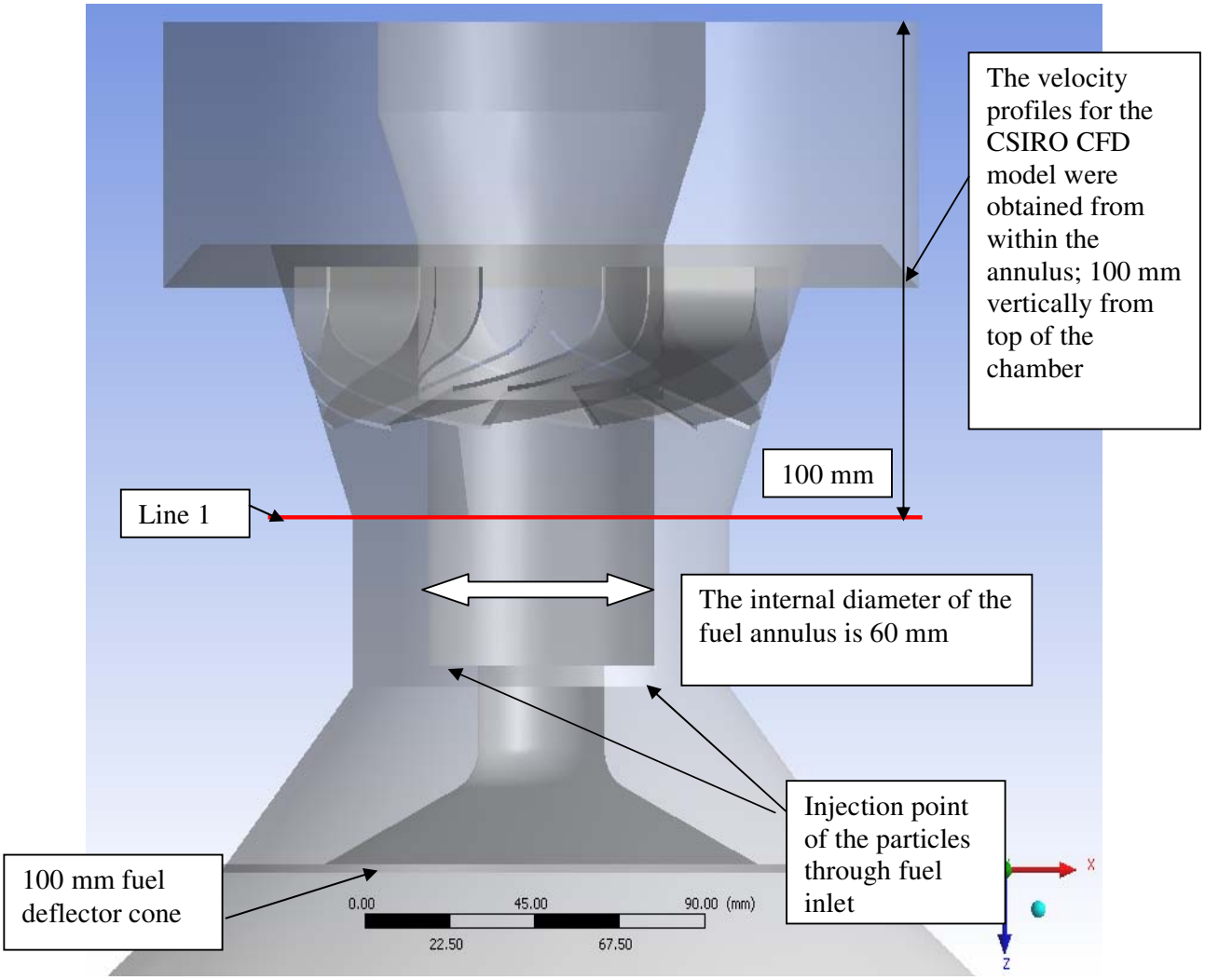

Figure 4-8: A CAD schematic of the annular geometry where the velocity profiles have been obtained

4.3.2 Velocity Profiles

This section compares plots of tangential and vertical velocity for CSIRO's results and the recreated results. In both the tangential and axial plots below, positive velocity is in the downward direction.

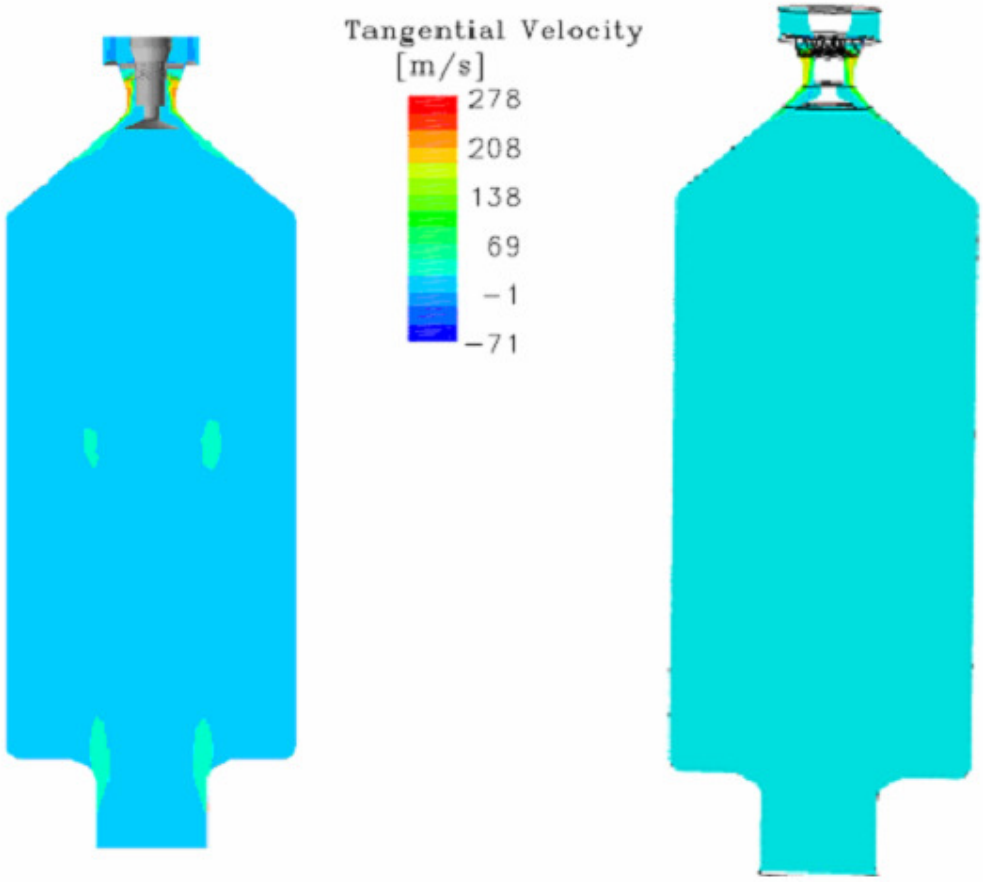

Figure 4-9 Plot of tangential velocity on a central plane for the CSIRO model (left), recreated model (right)

When analysing the velocity plots from CSIRO's modelling and the recreated model, both models show a strong region of downward flowing gas at the outer walls in the top section of the chamber. The CSIRO model demonstrates a lower tangential velocity zone through the centre of the chamber compared to recreated model – refer to Figure 4-9.

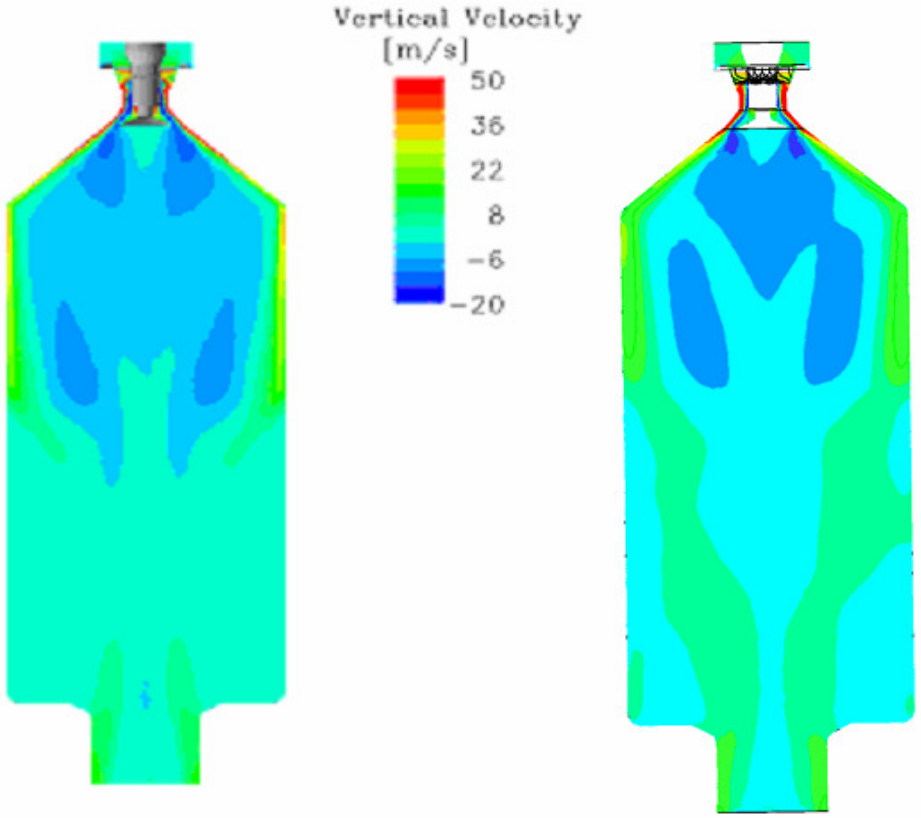

Figure 4-10: Plot of vertical velocity on a central plane for the CSIRO model (left), comparison model (right)

Figure 4-10 illustrates the vertical velocity (axial velocity) plotted on a central plane. Both models identify a central recirculation zone in the upper part of the chamber, which Syred et al (1997) likens to a pair of kidneys. Both models are similar to each other over the whole chamber and show an upward flow of gas along the centreline of the chamber with entrainment occurring through the throat.

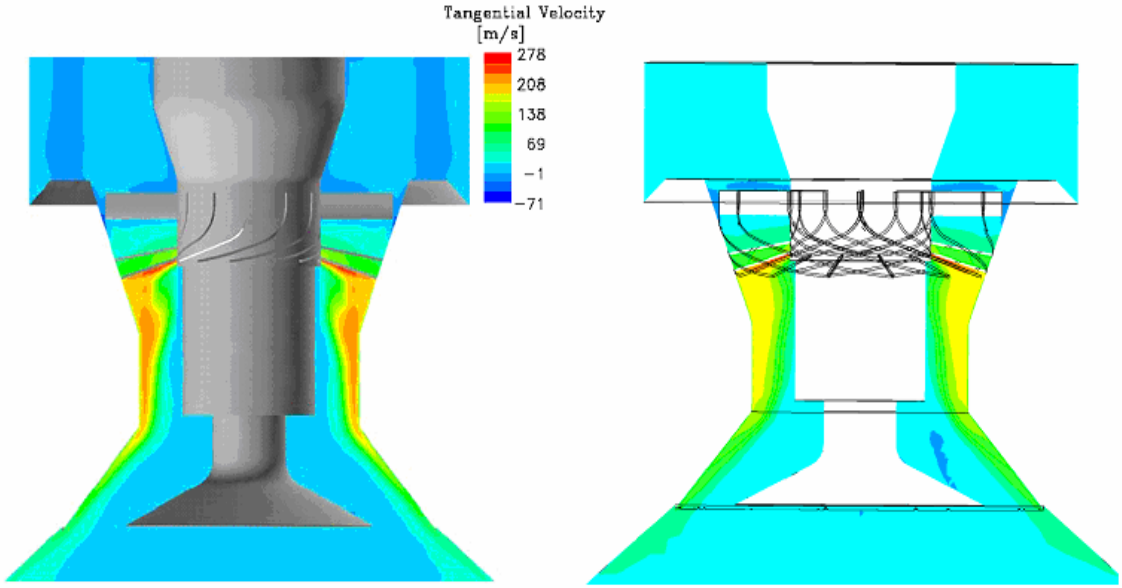

Figure 4-11: Plot of tangential velocity on a central plane for the swirl burner section. CSIRO model (left), comparison model (right)

Figure 4-11 shows the tangential velocity in the swirl burner section of both the CSIRO model and the recreated model. Both the CSIRO model and the recreated model show high tangential velocities of approximately 200 m/s near the wall. The CSIRO model more accurately illustrates the tangential velocity in the swirl region due to the more defined velocity contours in the high velocity regions.

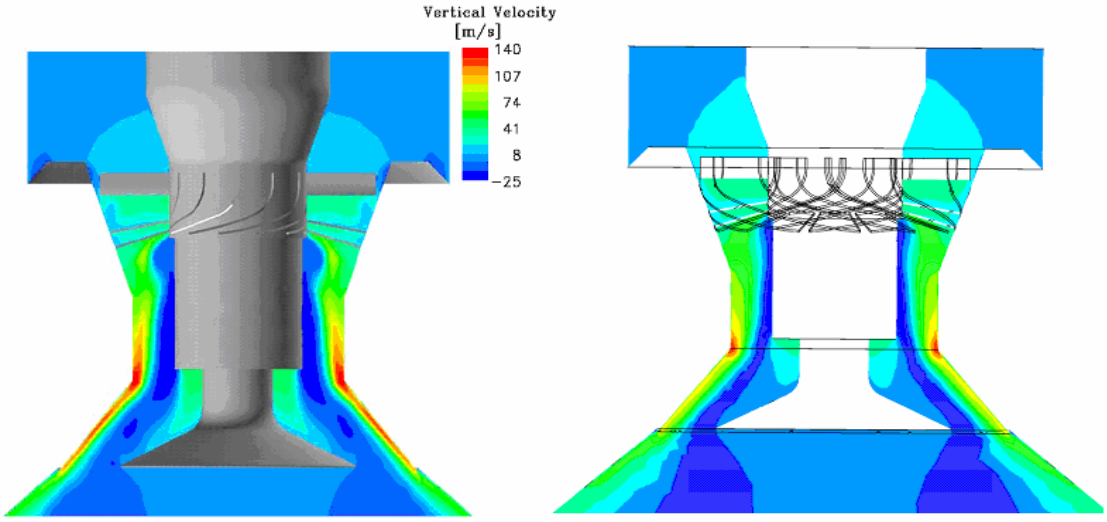

Figure 4-12: Plot of vertical velocity on a central plane for the swirl burner section. CSIRO model (left), comparison model (right)

Figure 4-12 shows axial velocities in the swirl burner section for both the CSIRO model and the recreated model. Both models show high axial velocities (greater than 100 m/s) near the wall (slightly higher in CSIRO model). The velocity profiles of the two models are very similar with the exception of the recirculation zone (negative velocity) beneath the fuel deflector cone in the recreated model.

4.3.3 Comparison of the Velocity Profiles in the Annulus

A comparison of tangential velocities between the CSIRO simulation and the recreated simulation is shown in Figure 4-13 and a comparison of axial velocities is illustrated in Figure 4-14. In both the tangential and axial profiles below, positive velocity is in the downward direction.

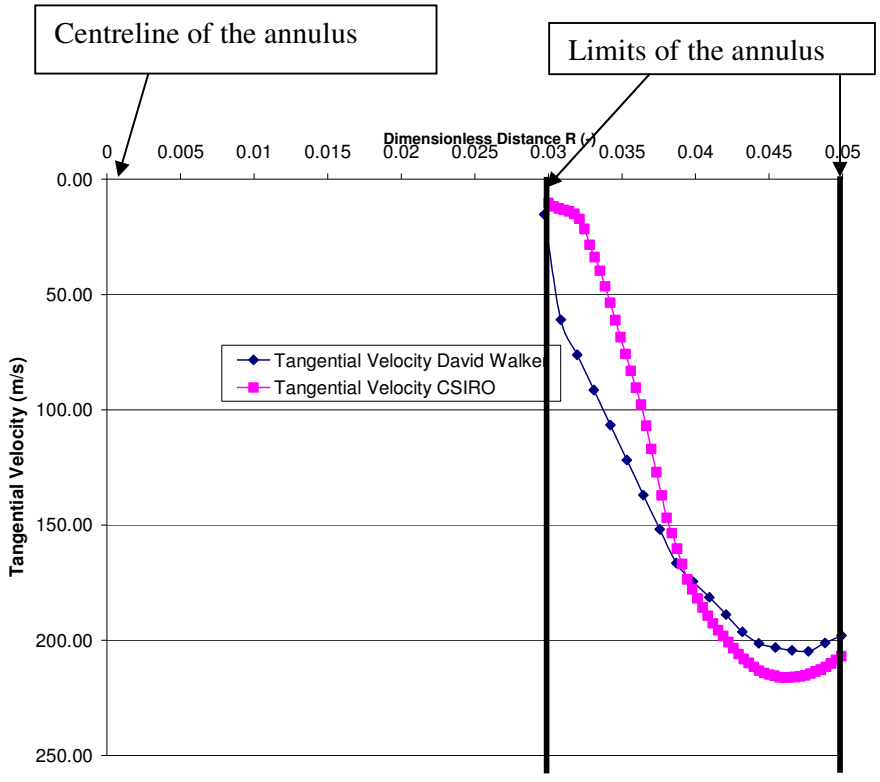

Figure 4-13: A radial profile of the tangential velocity

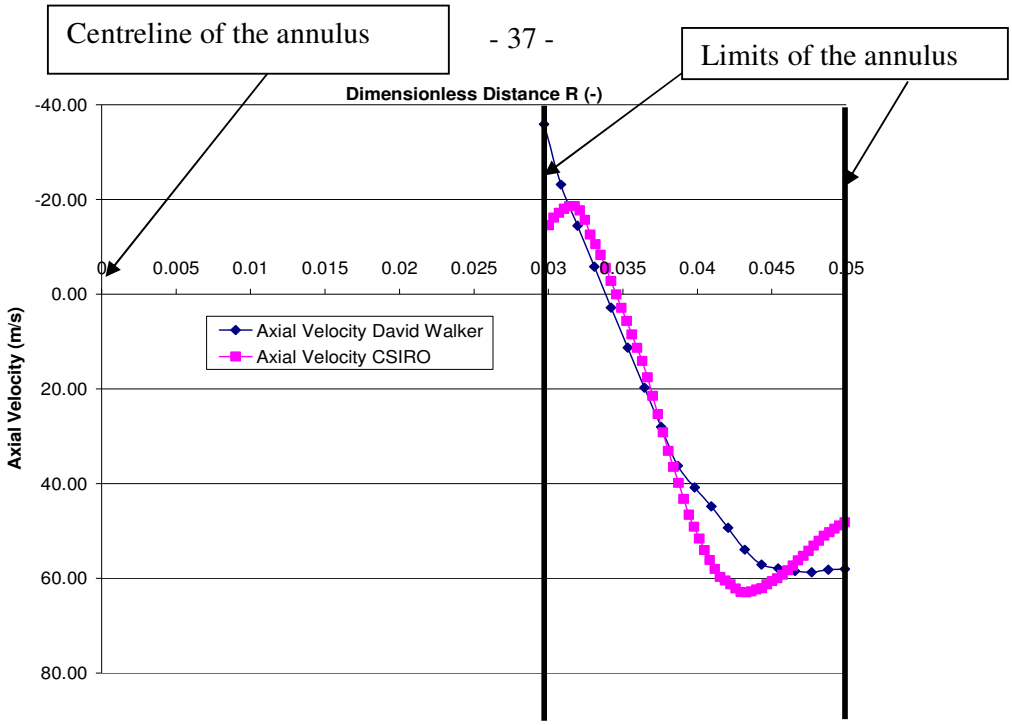

Figure 4-14: A radial profile of the axial velocity

The tangential velocity profiles for both the CSIRO and the recreated models results (Figure 4-13) show that the tangential velocity is increasing with an increasing radius. The CSIRO model results show a higher peak tangential velocity of approximately 215 m/s compared to the recreated model (approximately 200 m/s). Both models' results showed the tangential velocity in the flow field tended towards zero at the axis of symmetry. Points of variance between the two models are greatest between the dimensionless distances of 0.03 and 0.035.

In Figure 4-14 the axial profile from the CSIRO simulation was plotted alongside the profiles of the recreated simulation. Both profiles start with negative velocities – the recreated model with –35 m/s and the CSIRO model with –15 m/s. The CSIRO profile initially decreases before increasing in line with the recreated model. This initial decrease is not seen in the recreated model. Between the dimensionless distances of 0.0325 and 0.0375 both axial profiles are almost identical. Variance between the two models again occurs between the dimensionless distances of 0.04 and 0.045. The CSIRO model has a peak velocity of 65 m/s and then the axial velocity decreases before reaching the limits of the annulus. This decrease in the axial velocity before reaching the limits of the annulus does not occur in the recreated model. The recreated model has a peak velocity of 59 m/s.

4.4 Discussion of Grid Independence Study

A grid independence study was undertaken to prove grid independence for the high (H 70 Series) and low swirl (L 70 Series) steady state results. Due to the complex geometry of the primary combustion chamber and the swirl burner, there were a significant number of finite volume elements and nodes for both the high swirl and low vane set-ups. The significant number of finite volume elements and nodes were specified to ensure that an accurate solution was obtained in this particular region. For this study at least two other meshes were created – one being more coarse and the other being finer than the working mesh (Current Mesh).

As illustrated in Figure 4-2 grid independence is evident at Line 1 (swirl vane section) for the H 70 Series. The consistent axial velocities across the different horizontal arbitrary points for each of the meshes modelled, demonstrate grid independence.

Figure 4-3 shows that the profiles at Line 2 (primary combustion chamber) are non-symmetrical over the chamber and that the profiles are slightly skewed, but on the whole the profile patterns are very similar. However the 'High Swirl Current Mesh more inflation layers' profile differs slightly from the other mesh profiles near the wall - specifically it does not dip from the high velocity of 70 m/s unlike the other mesh profiles. This result was unexpected as this mesh contains two extra inflation layers, and therefore the solution should be more accurate when nearest the wall due to the extra boundary layers. However, despite the slight variance between the mesh profiles when nearest the wall, grid independence can still be assumed, as on the whole the profile patterns are very similar.

Figure 4-6 shows that the profiles obtained at Line 1 (swirl vane section) are very similar, i.e. they have matching arbitrary axial velocity points along Line 1, thus proving mesh independence in this region. The 'Low Swirl Fine Mesh' depicts higher velocities at the wall (approximately 70 m/s) compared to the 'Low Swirl Current Mesh' (approximately 65 m/s), which comes down to grid refinement, and a more accurate mesh in this region.

The profiles obtained at Line 2 (primary combustion chamber) are shown in Figure 4-7. The axial velocity profiles for the different meshes are a match in the outer third of the chamber radius. However between -0.2 m and 0.2 m there is a slight variance between the 'Low Swirl Current Mesh' and the 'Low Swirl Fine Mesh' due to the finer mesh creating a more accurate solution from the modelling. Despite the slight variance between the mesh profiles within this

small region, grid independence can be assumed, as on the whole the profile patterns are very similar.

A grid independence study was also undertaken for the modelling undertaken by CSIRO (H 100 Series). The aim of this study was to evaluate the velocity profile plots of the tangential and axial velocities from the CSIRO model against a recreated model. To do this, velocity profiles within a 60 mm diameter annulus, and 100 mm downstream of the swirl vanes were used to check the consistency of the results obtained from CSIRO.

Figures 4-9 to 4-12 show the comparison between the CSIRO model and the recreated model for tangential and axial velocity plots. Both models represent lower tangential velocities in the top section of the chamber weakening along the chamber length. High axial velocities near the wall in the swirl vane section and regions of negative axial velocities (i.e. recirculation zones) in both the swirl vane section and in the primary chamber were also identified.

Figure 4-13 shows the tangential velocity profiles for both the CSIRO and recreated models results inside the annulus under the swirler region. This Figure shows firstly the tangential velocity increasing for both profiles with an increasing radius, and secondly the characteristics of a Rankine vortex (Wakelin 1993) consisting of an outer free vortex and solid-body rotation at the core region – refer to Figure 3-1. Both profiles demonstrated that the tangential velocity in the flow field tends towards zero at the axis of symmetry, which is typical of the research conducted by Wakelin (1993).

Points of variance between the two models occurred because the CSIRO annular profile contained more data points, and additionally, a more refined mesh had been used to simulate this high turbulent region. Due to the complex geometry of the primary chamber and the swirl burner, the use of a more refined mesh was more applicable due to the high turbulent regions.

Figure 4-14 shows the axial profile from the CSIRO simulation plotted alongside the profile of the recreated simulation. Both profiles start with negative velocities – indicating a reversal of flow (recirculation zone). The CSIRO profile initially decreases before increasing in line with the recreated model. This initial decrease is not seen in the recreated model due to the CSIRO profile containing more data points and hence more detail in this region. Between the dimensionless distances of 0.0325 and 0.0375 both axial profiles are almost identical which indicates reliable mesh grids with similar grid solutions.

Noting the inability to validate the recreated model or CSIRO's model in practice, the length of the vortex and the strength of the recirculation cannot be identified. However, the consistent velocity profile plots of the tangential and axial velocities found in both models indicate reliable mesh grids and experimental validation should be undertaken to determine the model's validity. The variance between the two models is the result of the CSIRO mesh being more refined in high gradient regions which as a result leads to accurate solutions.

It is recommended that more refinement to the recreated model is carried out in the regions of high gradient, specifically in the swirler section, to justify the recreated model being comparable to the CSIRO model.

5. CFD Comparison Study between the Steady State High and Low Swirl Vane Modelling Results

5.1 Background to Steady State Simulations

The time dependence of the flow characteristics can be specified as either **steady state** or **transient**. Steady state simulations, by definition, are those whose characteristics do not change with time and whose steady conditions are assumed to have been reached after a relatively long time interval. They therefore require no real time information to describe them. Many practical flows can be assumed to be steady after initial unsteady flow development, for example, after the start-up of a rotating machine.

A detailed steady state CFD comparison study was undertaken between flows in the swirl chamber using (a) the high (H 70 series) and (b) the low swirl vanes (L 70 series), both feeding onto a 70 mm fuel deflector cone. The high swirl simulation was set up with 'high spin' vanes with a vane angle of 15° (to the tangential component of the vane direction), which gave rise to a high swirling flow. The high and low swirl setups are represented in Figures 5-2, 5-3a, and 5-3b.

Figure 5-2: The two different setups for the vanes; each geometry having a different vane angle

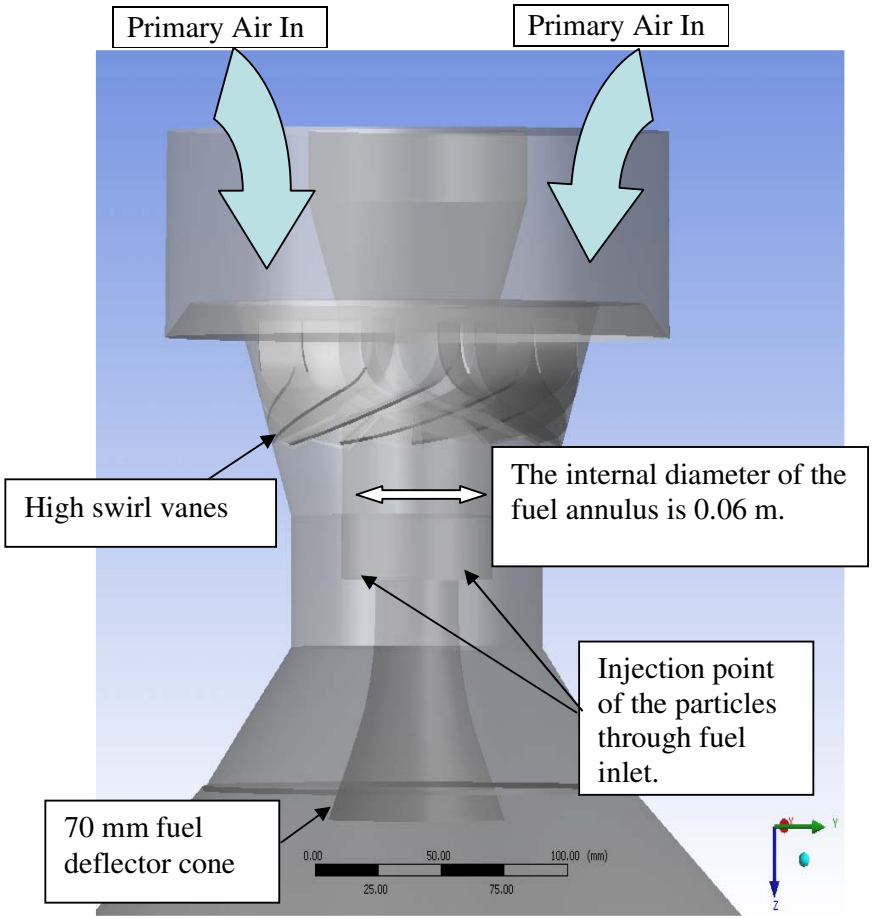

Figure 5-3a: A CAD schematic showing the H 70 series (high swirl vane setup)

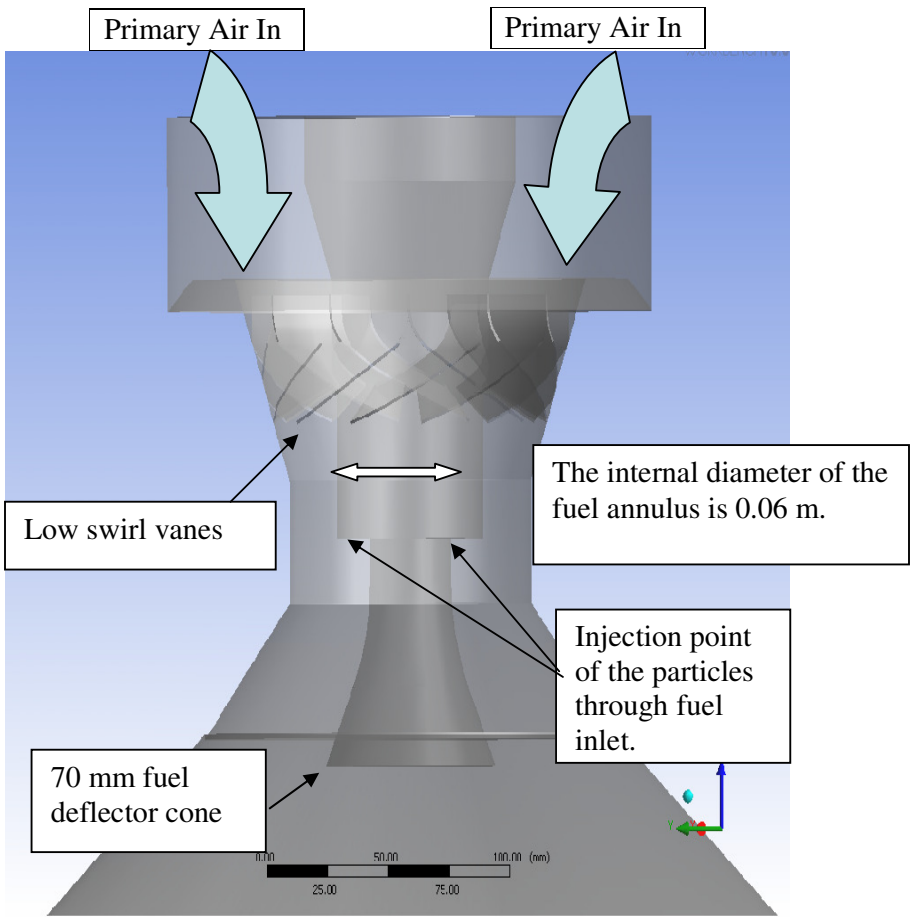

Figure 5-3b: A CAD schematic showing the L 70 series (low swirl vane setup)

5.2 The CFX Simulation

The internal diameter of the primary chamber is 0.6 m and the modelled section of the primary chamber is approximately 1.7 m long including the swirl burner. Unstructured meshing of the primary combustion chamber and swirl burner took place using the mesh building code ICEM CFD. Due to the complex geometry of the primary combustion chamber and swirl burner the determined number of finite volume elements and nodes were very large for both the high swirl and low swirl vane setup. The high swirl setup consisted of 2,298,392 finite volume elements corresponding to 702,261 nodes. The low swirl setup consisted of 1,655,086 elements corresponding to 560,220 nodes. The design of the control volumes was important because they had to be small enough to resolve the significant length scale of the flow. The swirl vane section (vanes, and fuel-deflector cone) of both scenarios required grid refinement because of their significantly high velocity gradient; as a more complex flow coupled with a high velocity gradient will require a higher cell density in order to capture the correct flow field.

The simulation was initiated as a steady-state calculation and continued to operate for sufficient iterations to establish a mass balance and a flow field. The solver eventually achieved a normalized residual of less than 10^{-4}, deemed as good convergence – refer to Figures 5-4a and 5-4b where Log RMS has been plotted against the number of iterations for both the high and low swirl setups.

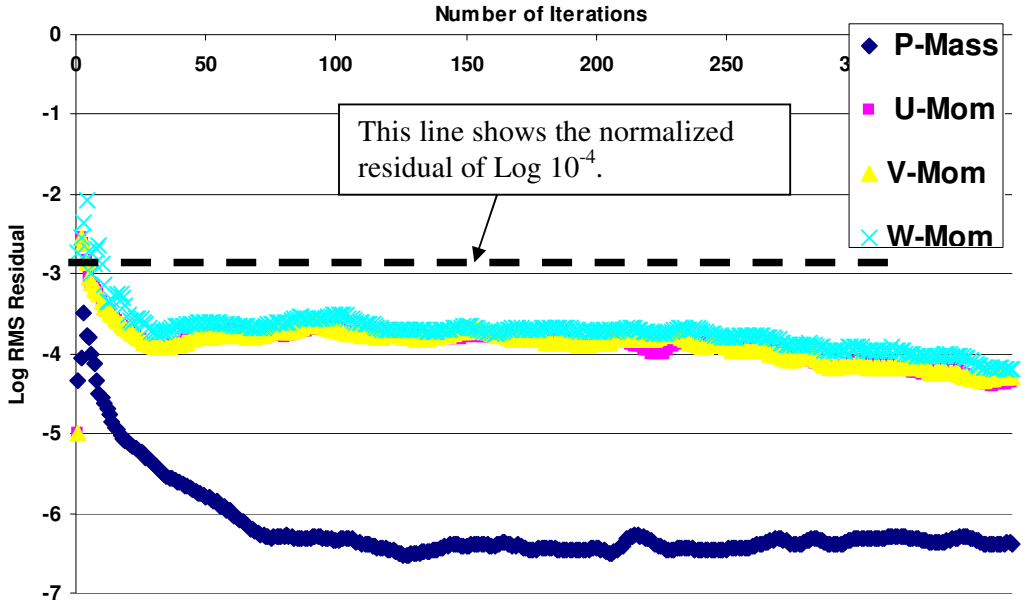

Figure 5-4a: Plot of Log RMS Residual against the number of iterations for the converged high swirl simulation obtained from the CFX output file .

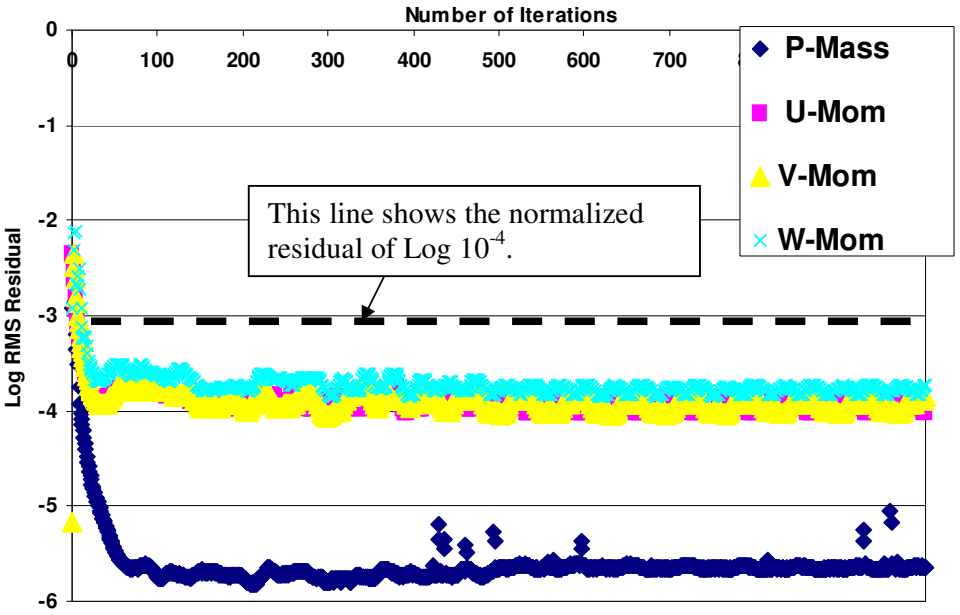

Figure 5-4b: Plot of Log RMS Residual against the number of iterations for the converged low swirl simulation obtained from the CFX output file

Figures 5-4a and 5-4b show plots of a converged solution for the Log RMS Residual satisfying the mass and momentum equations from CFX-Solver for both the high and low swirl scenarios.

The high swirl simulation was run for a maximum number of 360 iterations before solving compared to the low swirl setup, which took a number of 1000 iterations before solving.

The CFX model was set up so that the particles hit the fuel deflector cone and bounced off, whilst in the primary chamber the particles were forced to the sides and adhered to the walls. Specific physical parameters of the particles were required as a boundary condition for the particle tracking model (refer to Table 5-1). Since the primary chamber walls would have molten sludge flowing down them, the particles were allocated a coefficient of restitution of zero, indicating that a particle would be completely stopped if it came into contact with these walls (Anon, 2005). The remainder of the walls in the model were given a coefficient of restitution of one, which indicated that a particle would bounce upon striking the boundary (Anon, 2005). Figure 5-5 shows the walls with a defined coefficient of restitution of zero.

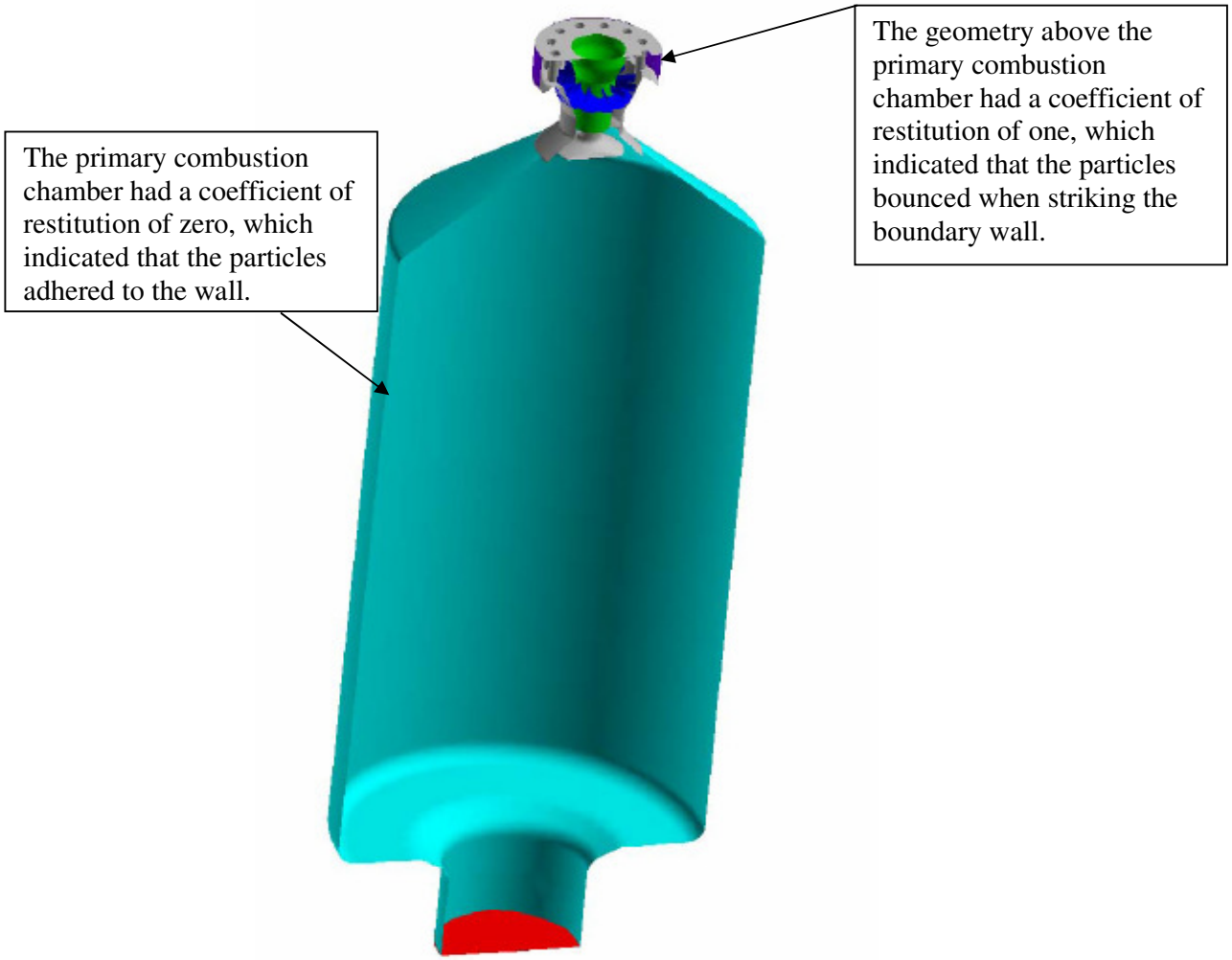

Figure 5-5: Plot showing walls defined with a zero coefficient of restitution, light blue section.

5.3 Boundary Conditions

The boundary conditions supplied by Lemar were the inlet mass flow rates as shown in Table 5-1. In addition to these boundary conditions the chamber operating pressure was specified as 1.01 bar. The particle density was 1200 kg/m³.

Table 5-1: CFD model boundary conditions provided by Lemar.

Location	Mass flow rate (kg/s)
Fuel Air	0.040
Primary Air	0.149
Diesel Air	0.001
Solid Particles	0.038

5.4 Velocity Profiles

Results of the two-phase CFD modelling of the primary chamber for both the high (H 70 series) and low swirl (L 70 series) vanes are presented below in a series of plots and graphs of the velocity profiles. The simulation results shown in this section are based on isothermal flow without combustion.

Profiles of tangential and axial velocities obtained from the CFD modelling (for both high and low swirl vanes) were determined downstream of the vanes. The velocity profiles were exported from lines drawn within the annulus (0.04 m downstream of the vanes), at the bottom of the fuel-deflector cone (0.115 m downstream of the vanes), and in the primary chamber (0.300 m downstream of the vanes), as shown in Figure 5-6.

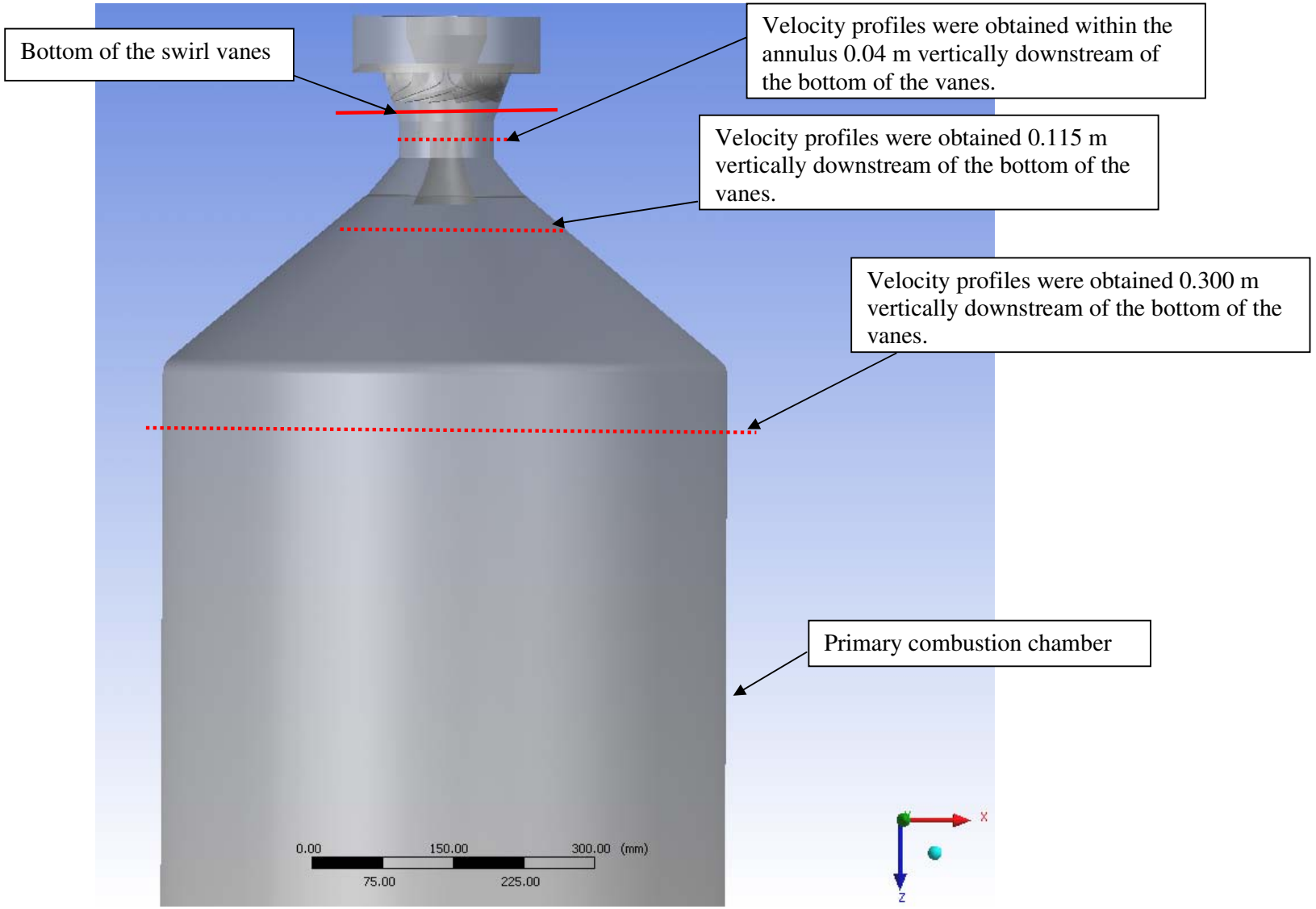

Figure 5-6: Shows the locations within the primary combustion chamber where the three velocity profiles were established

5.5.1 Comparing the High (H 70 Series) and Low Swirl (L 70 Series) Velocity Profiles (Figures 5-7 to 5-9)

Figure 5-7 shows that higher tangential velocities are found nearest to the wall of the annulus, being approximately 165 m/s for the high swirl and 70 m/s for the low swirl. Both tangential profiles dip in velocity at the wall, which is at a dimensionless distance of 0.05 shown on Figure 5-7. The high and low swirl results also show tangential velocity in the flow field tending to zero at the axis of symmetry. When comparing the axial profiles for both setups, it is obvious that the high swirl setup shows a higher peak velocity nearest the wall of approximately 140 m/s compared to 65 m/s for the low swirl. The high swirl setup illustrates a small region of negative flow (i.e. recirculation zone) between the dimensionless distances of 0.03 and 0.04, whilst the low swirl axial setup has a positive axial velocity throughout this region.

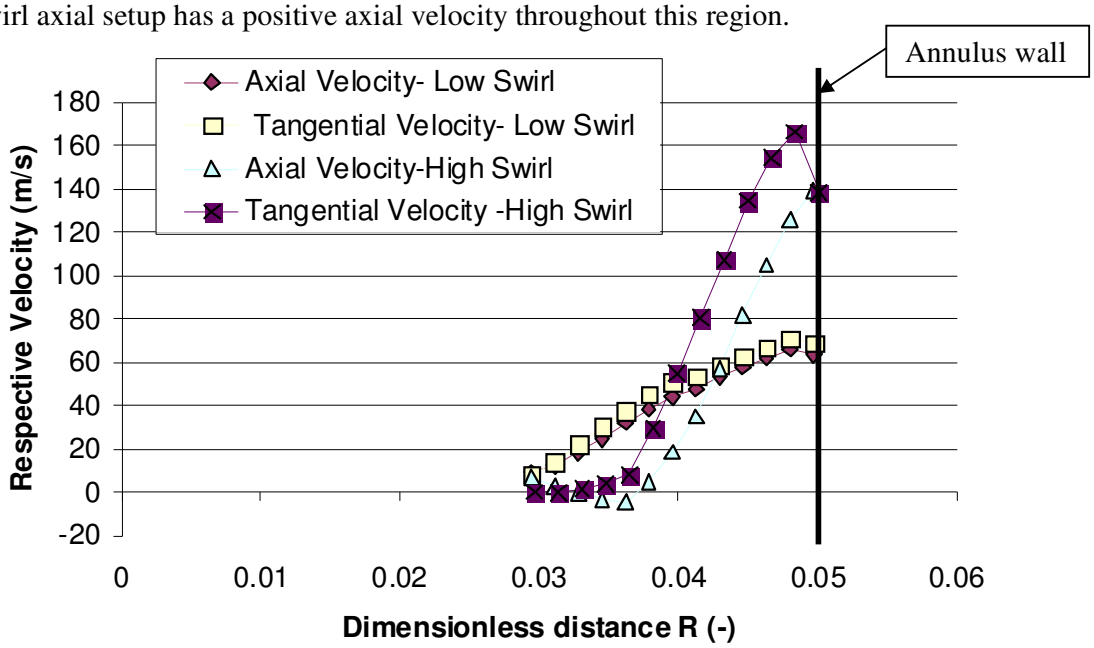

Figure 5-7: The velocity profiles inside the annulus (0.04 m below the vanes) for both the high and low swirl setups

When analyzing the velocity profiles below the fuel-deflector cone (0.115 m below the vanes) – refer to Figure 5-8, it can seen that the tangential velocity is again higher across the profile towards the wall (peak velocity of 55 m/s) compared to the low swirl setup peak velocity of 27 m/s. There is a slight dip in tangential velocity with both the high swirl and low swirl setups at the wall, which is at a dimensionless distance of approximately 0.1 as shown in Figure 5-8. Overall it can be said that the low swirl tangential velocity profile is a lot 'flatter' in shape, compared to the more 'vertical' profile of the high swirl setup. The two axial profiles show an

initial negative velocity indicating a reversal in flow which is opposite in rotational direction to the inlet flow.

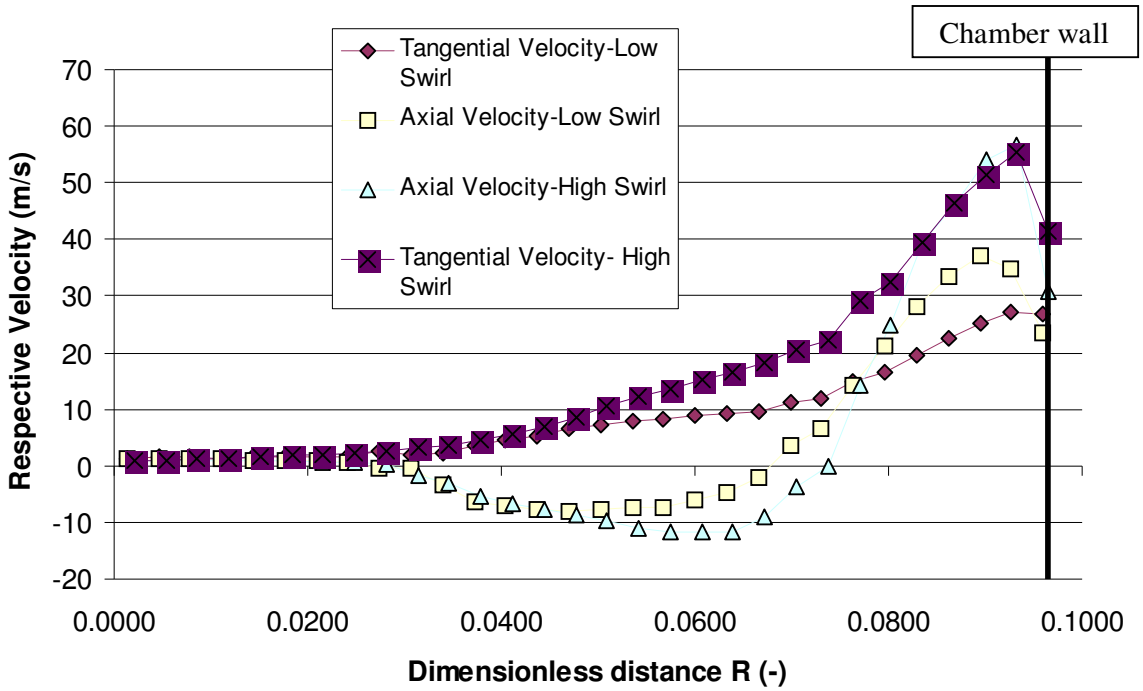

Figure 5-8: The velocity profiles below the fuel-deflector cone (0.115 m below the vanes) for both the high and low swirl setups

Figure 5-9 represents the velocity profiles in the primary combustion chamber (0.300 m below the vanes) for both the high and low swirl setups. The high swirl tangential profile strongly resembled the Rankine vortex as described previously. However, the low swirl plot tended negative approximately between 0.2 and 0.25 m away from the chamber wall. This profile tended positive from 0.25 until it reached the wall. The two axial profiles in the combustion chamber were negative until approximately 0.25 m from the centre of the chamber, and then turned positive. The high swirl axial velocity profile has the highest peak velocity, this being 17 m/s, compared to 14 m/s for the low swirl setup and from here both profiles dipped in value nearest the wall.

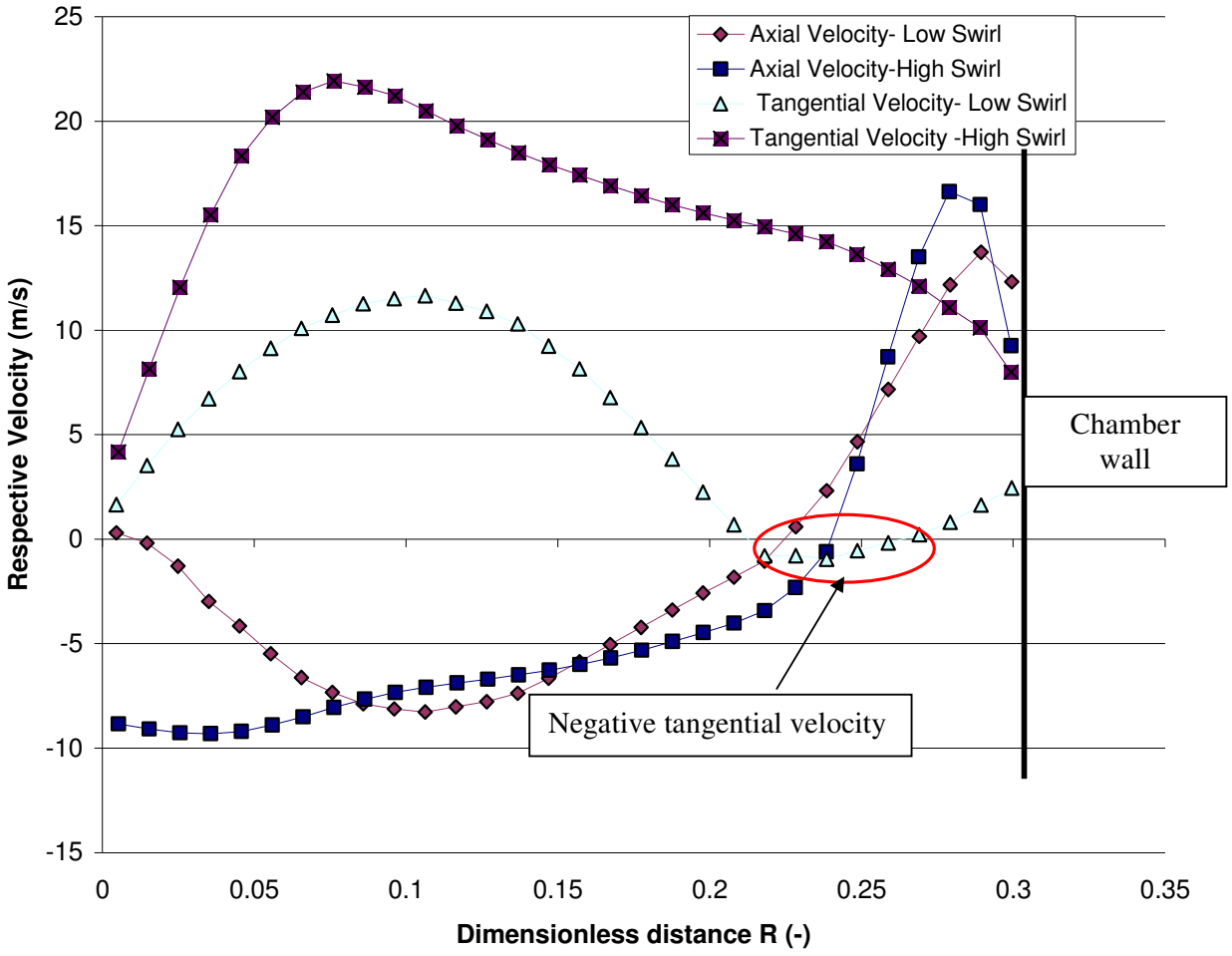

Figure 5-9: The velocity profiles in the primary combustion chamber (0.300 m below the vanes) for both the high and low swirl setups

5.5.2 Comparing the High (H 70 Series) and Low Swirl (L 70 Series) Velocity Profiles (Figures 5-10 to 5-13)

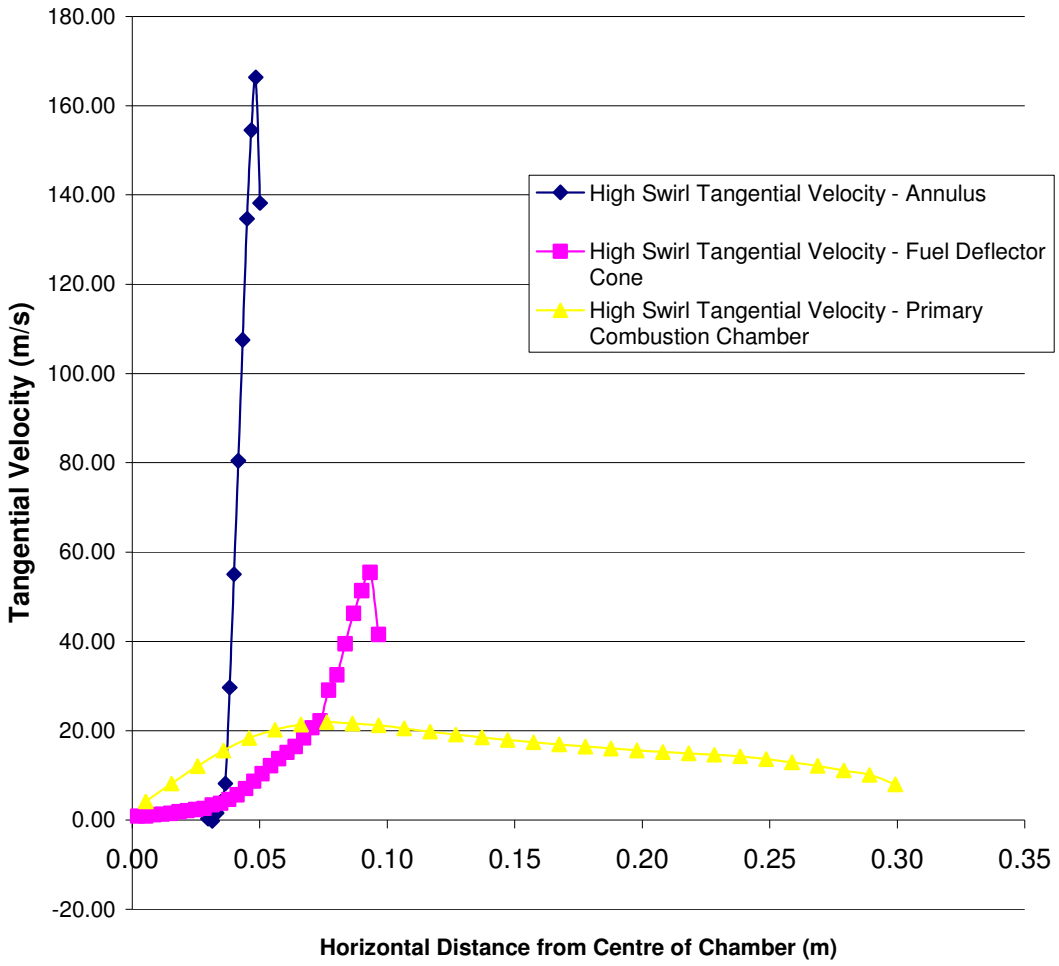

Figure 5-10: The high swirl tangential velocity profiles from within the annulus (0.04 m downstream of the vanes), at the bottom of the fuel-deflector cone (0.115 m downstream of the vanes), and in the primary combustion chamber (0.300 m downstream of the vanes).

Figure 5-10 shows the high swirl tangential velocity profiles within the annulus (0.04 m downstream of the vanes), at the bottom of the fuel-deflector cone (0.115 m downstream of the vanes), and in the primary combustion chamber (0.300 m downstream of the vanes). The profile taken from within the annulus peaks nearest the wall and has a very high velocity of 167 m/s. The profile taken below the fuel deflector cone shows a high velocity (approximately 57 m/s), dipping near the wall. The profile taken from the primary combustion chamber has a low peak tangential velocity of 22 m/s when 0.05 m away from the centre of the chamber. This profile is a lot 'flatter' in shape compared to the other two profiles.

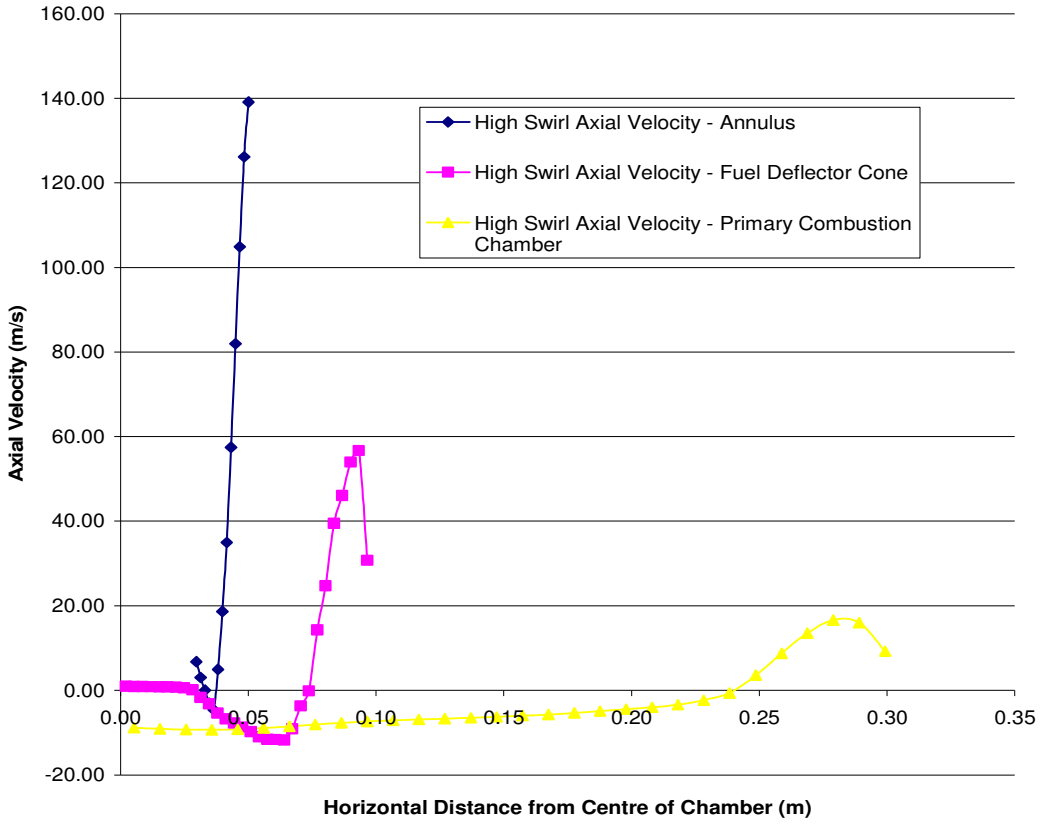

Figure 5-11: The high swirl axial velocity profiles from within the annulus (0.04 m downstream of the vanes), at the bottom of the fuel-deflector cone (0.115 m downstream of the vanes), and in the primary combustion chamber (0.300 m downstream of the vanes).

Figure 5-11 shows the high swirl axial velocity profiles within the three locations (refer to Figure 5-6). The axial velocity profile within the annulus has no dip in velocity near the wall whereas the remaining two profiles in Figure 5-11 demonstrate a peak in axial velocity just before the wall, after which this velocity dips in value. As with the high swirl tangential velocities, the axial velocities are significantly higher nearer the wall of the annulus (140 m/s), compared to the 58 m/s under the fuel deflector cone and 17 m/s in the primary combustion chamber.

1. Initially the annulus profile demonstrates negativity for a short distance from the centre of the chamber and then tends positive for the remainder of the profile.
2. The profile under the fuel deflector cone demonstrates negativity but tends positive at an approximate distance of 0.075 m away from the centre of the chamber.
3. The profile in the combustion chamber is negative until approximately 0.25 m from the centre of the chamber, and then turns positive.

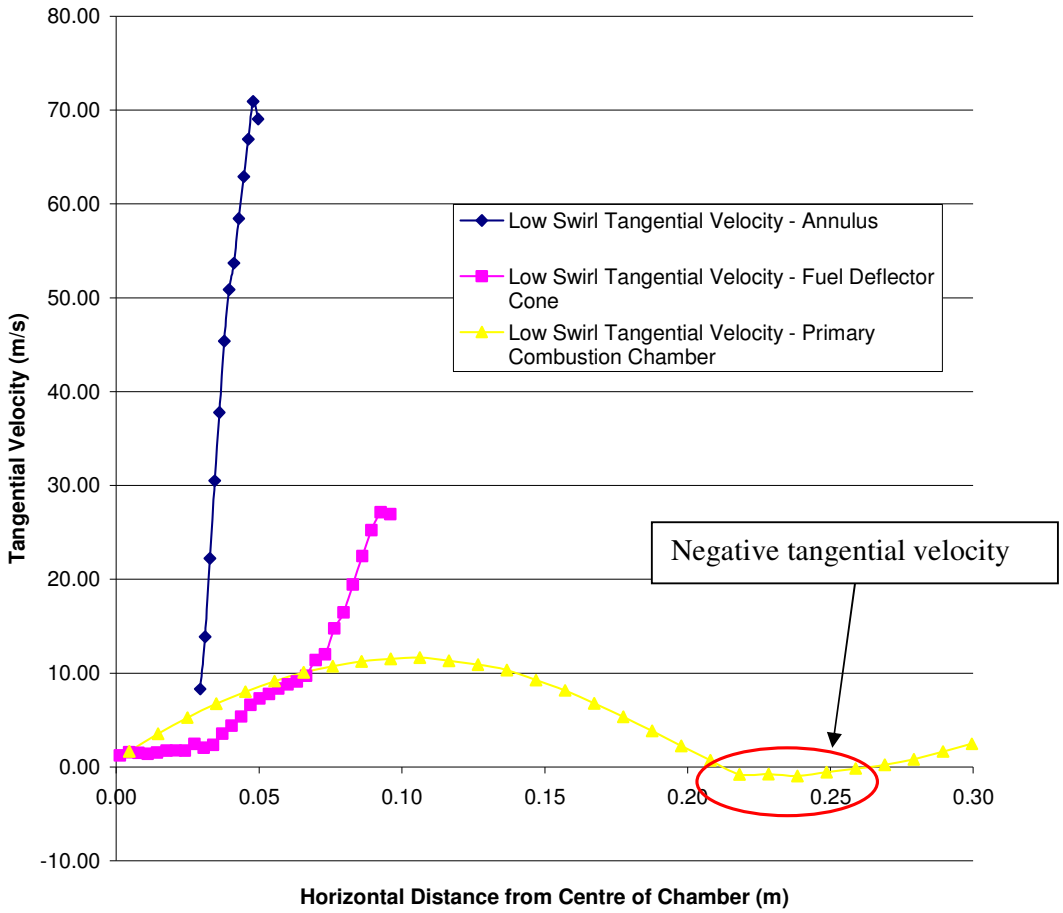

Figure 5-12: The low swirl tangential velocity profiles from within the annulus (0.04 m downstream of the vanes), at the bottom of the fuel-deflector cone (0.115 m downstream of the vanes), and in the primary combustion chamber (0.300 m downstream of the vanes).

Figure 5-12 shows the low swirl tangential velocity profiles. The tangential velocities of the low swirl vane setup are approximately half the value of that of the high swirl vanes (refer to Figure 5-10). The shape of the curves produced for both the annulus location and the fuel deflector location are similar to that of the high swirl; i.e. both the tangential velocity and the radius are increasing. The profile taken within the primary combustion chamber tends negative approximately between 0.2 and 0.25 m away from the chamber wall.

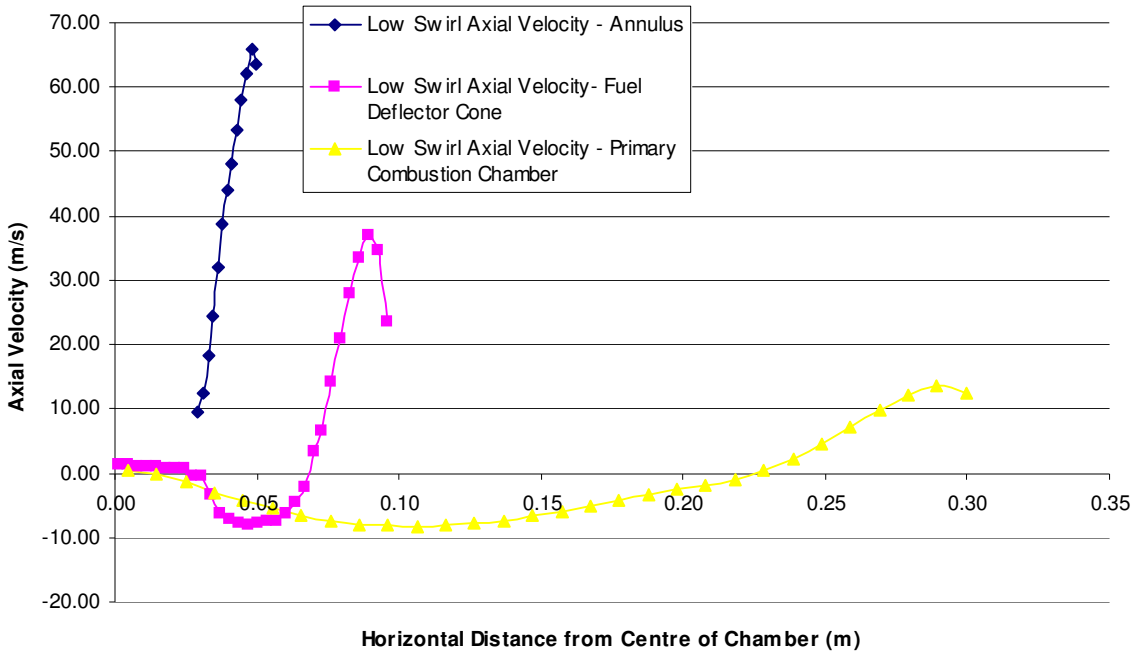

Figure 5-13: The low swirl axial velocity profiles from within the annulus (0.04 m downstream of the vanes), at the bottom of the fuel-deflector cone (0.115 m downstream of the vanes), and in the primary combustion chamber (0.300 m downstream of the vanes).

Figure 5-13 shows the low swirl axial velocity profiles. It can be seen that the axial velocity profile within the annulus has the highest peak velocity, this being 66 m/s, and from here this dips in value nearest the wall. The profile taken from under the fuel deflector cone has a peak velocity of approximately 37 m/s and tends negative over the profile. The profile taken from the primary combustion chamber has a peak velocity of approximately 13 m/s and also tends negative over the profile.

5.5.3 Comparing the Low and High Swirl Tangential Velocity Plots

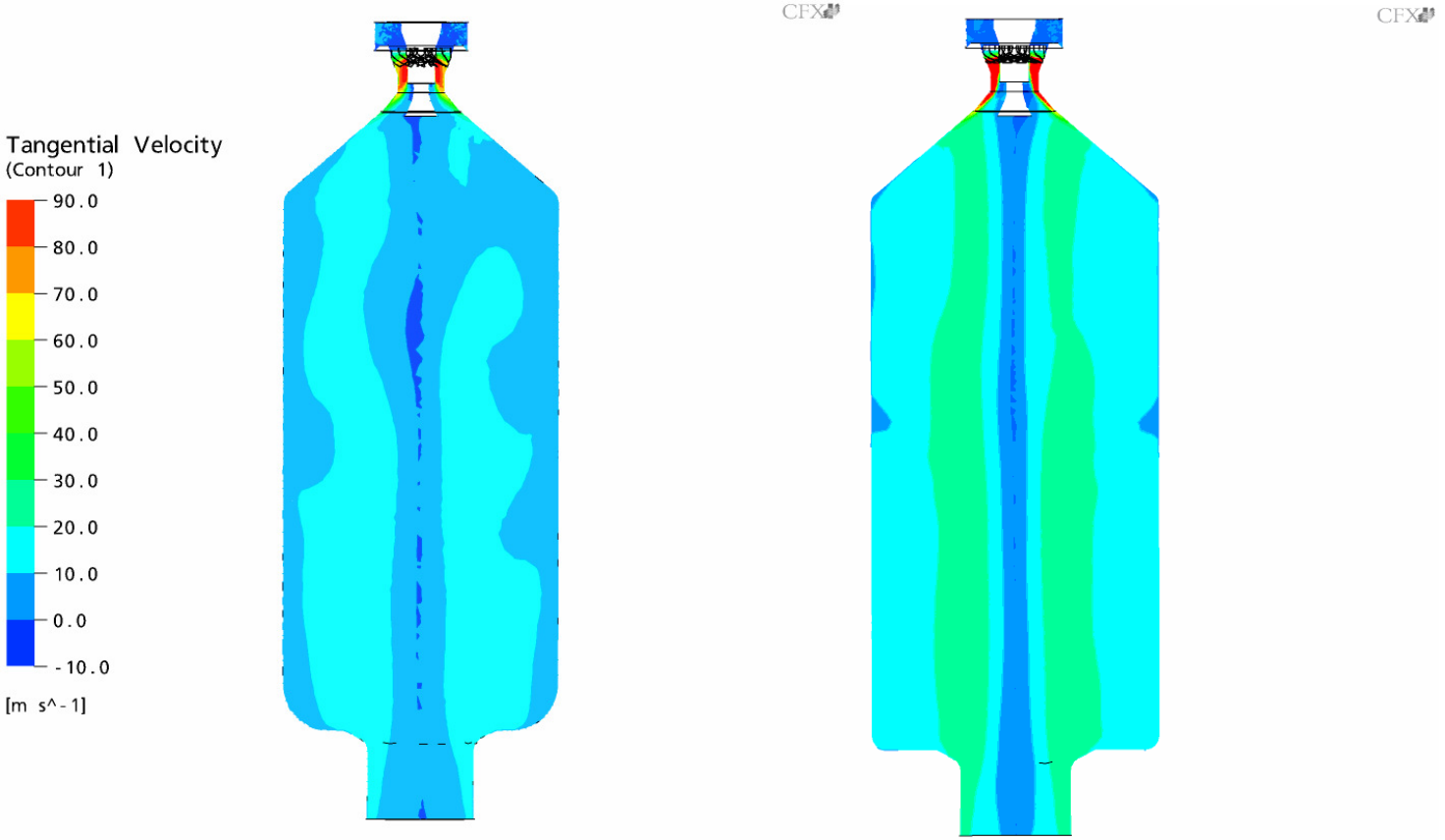

Figure 5-14: Plot of tangential velocity on a central plane for the low swirl vanes (left), and high swirl vanes (right)

The high swirl tangential velocity plot illustrates a central core vortex extending the length of the entire chamber. In the core region the tangential velocity ranges between 0-10 m/s. The two regions on either side of the central core are approximately symmetrical, having velocities between 20-30 m/s. Although the low swirl plot shows no definite central region there are low velocity regions on either side of the body of the chamber, between 10-20 m/s, and these extend the length of the chamber.

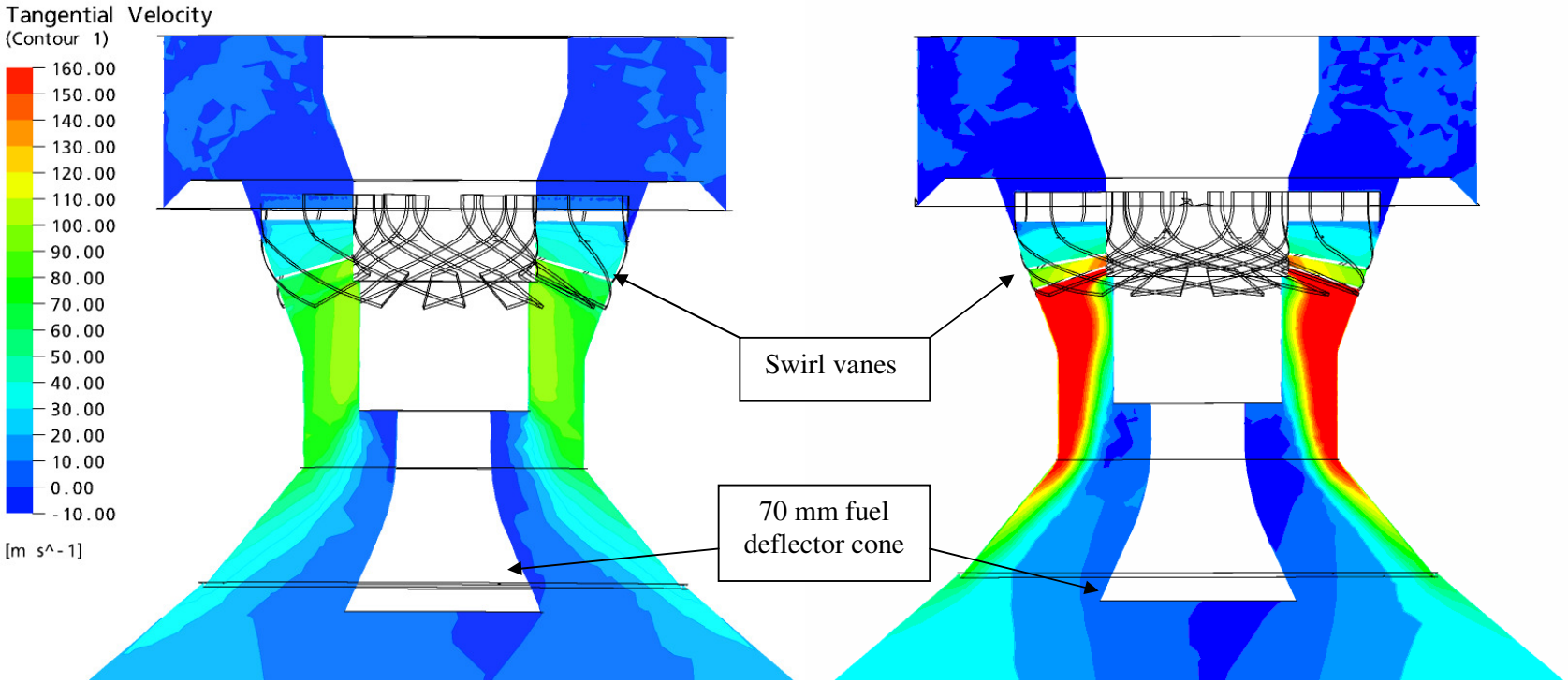

Figure 5-15: Plot of tangential velocity on a central plane for the swirl burner section. Low swirl vanes (left), and high swirl vanes (right)

In the swirl section, the high swirl setup indicates high gas velocities near the wall which are approximately 160 m/s compared to 70 m/s in the low swirler. The high swirl setup, unlike the low swirl, demonstrates a high tangential velocity that is imparted to the gas stream as it passes through the vane passage.

5.5.4 Comparing the Low and High Swirl Axial Velocity Plots

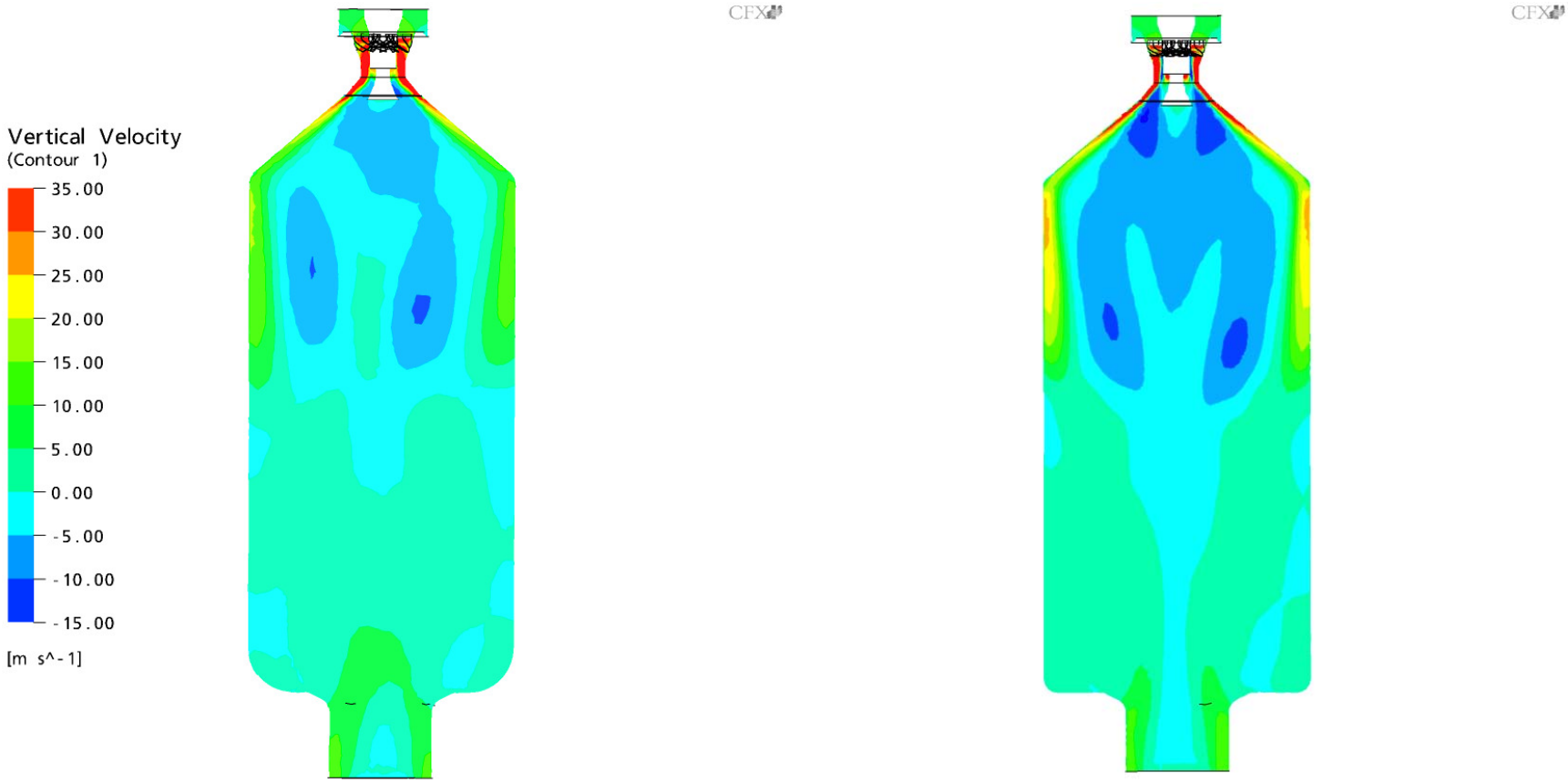

Figure 5-16: Plot of vertical (axial) velocity on a central plane for the low swirl vanes (left), and high swirl vanes (right)

The high swirl vanes demonstrate higher gas velocities (20-25 m/s) near the wall of the main chamber compared to the low swirl vanes (10-15 m/s). Both swirler setups have produced recirculation zones in the top half of the chamber - with the high swirl vanes showing a definite zone on either side of the fuel deflector cone, as well as similar velocities in the lower half of the chamber, with a definite recirculation surge. The velocities in this lower section are between -5 m/s to 5 m/s and both have similar outlet velocities, which are approximately 15 m/s.

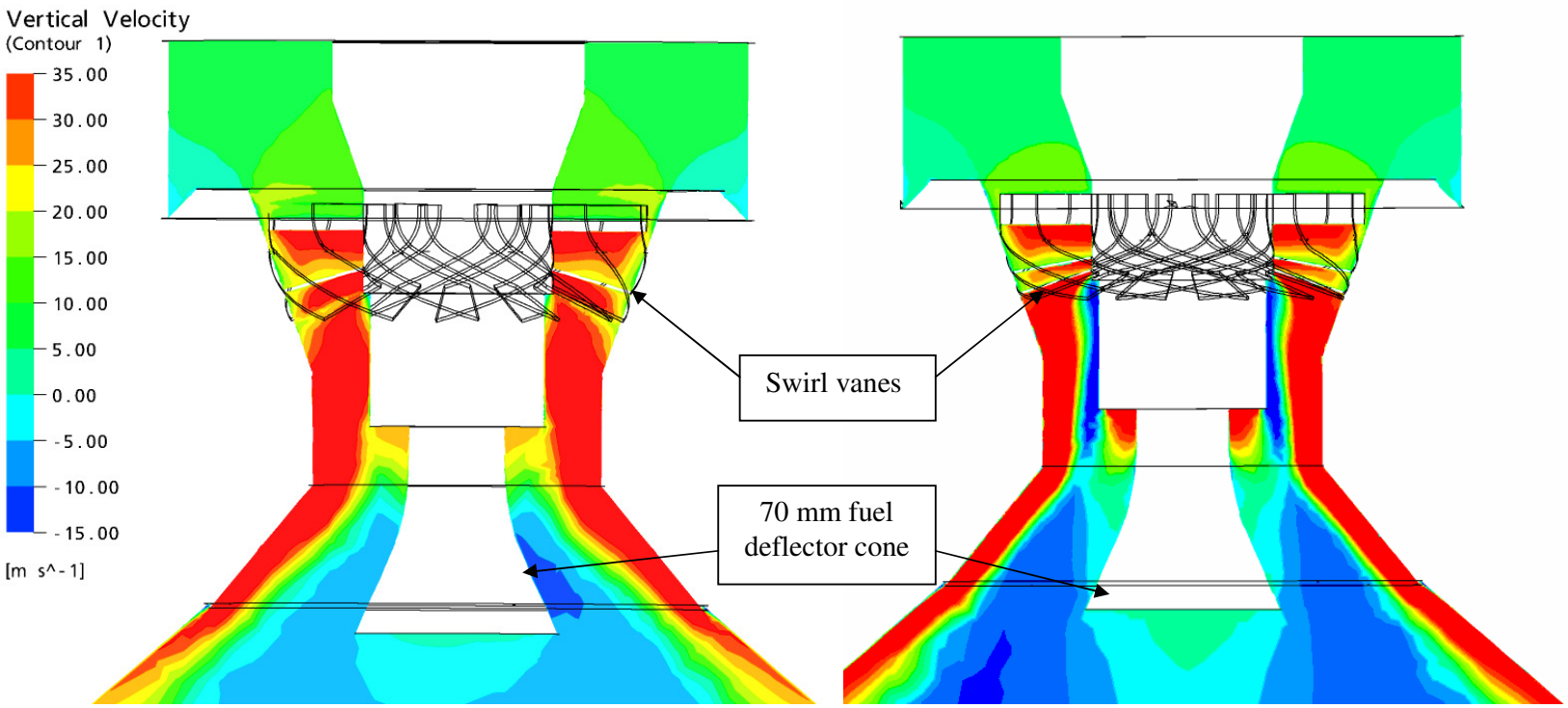

Figure 5-17: Plot of vertical (axial) velocity on a central plane for the swirl burner section. Low swirl vanes (left), and high swirl vanes (right)

In both setups high gas axial velocities in excess of 35 m/s are present at the outer chamber walls in the top section just below the swirl burner. The high swirl profile shows a region of upward flow gas both near the inner wall of the annulus by the swirler, and also on either side of the fuel deflector cone. The velocities directly beneath the fuel annulus are dissimilar. The low swirl plot shows velocities between 25-30 m/s decreasing to values between -5 – 0 m/s, whereas the high swirl plot demonstrates an axial velocity of approximately 35 m/s, which suddenly changes to a negative velocity indicating a recirculation point in the chamber.

5.5.5 Comparing the Low and High Swirl Velocity Vector Plots

Both the low and high swirl vane setups show velocity vector plots on a central plane. Both plots in Figure 5-18 demonstrate a reversal of flow in the main chamber and this is shown by the upward direction of the velocity vector arrows in the top half of the chamber. The low swirl setup has a reversal of flow in the range of 0 to -10 m/s which has no effect in the lower section of the chamber. Its large recirculation zone in the middle on the right hand side of the chamber is highlighted by the direction of the vectors.

In comparison, the high swirl setup shows a more turbulent swirling motion in the chamber (velocities range from 10 m/s to 55 m/s). The scattered vectors in the right-hand plot in Figure 5-18 illustrate the highly turbulent flow in the bottom section of the chamber generated by the high swirl setup. Figure 5-19 shows a three dimensional representation of the turbulent vector direction in both setups.

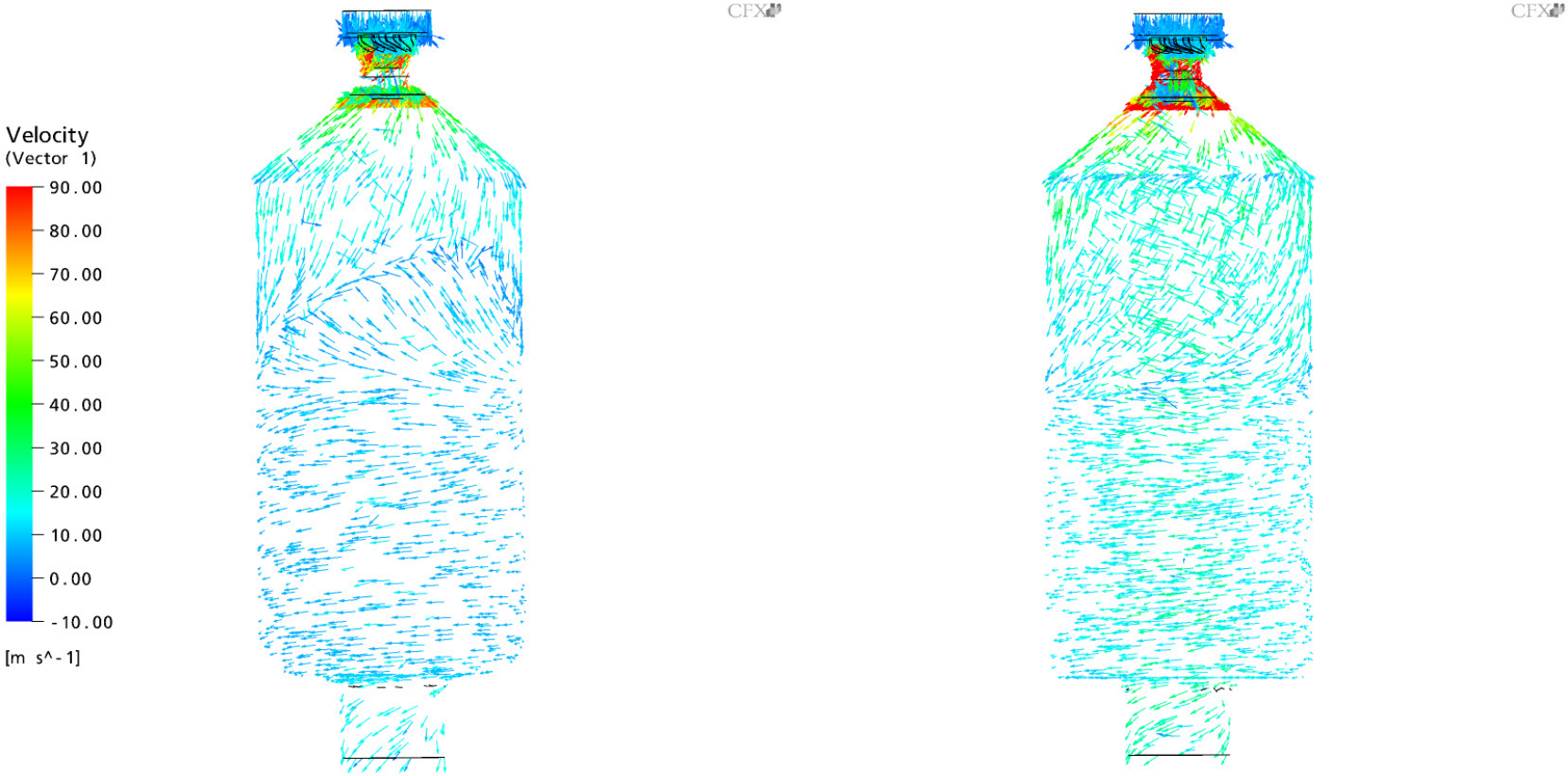

Figure 5-18: Vector plot of velocity on a central plane for the low swirl vanes (left), and high swirl vanes (right)

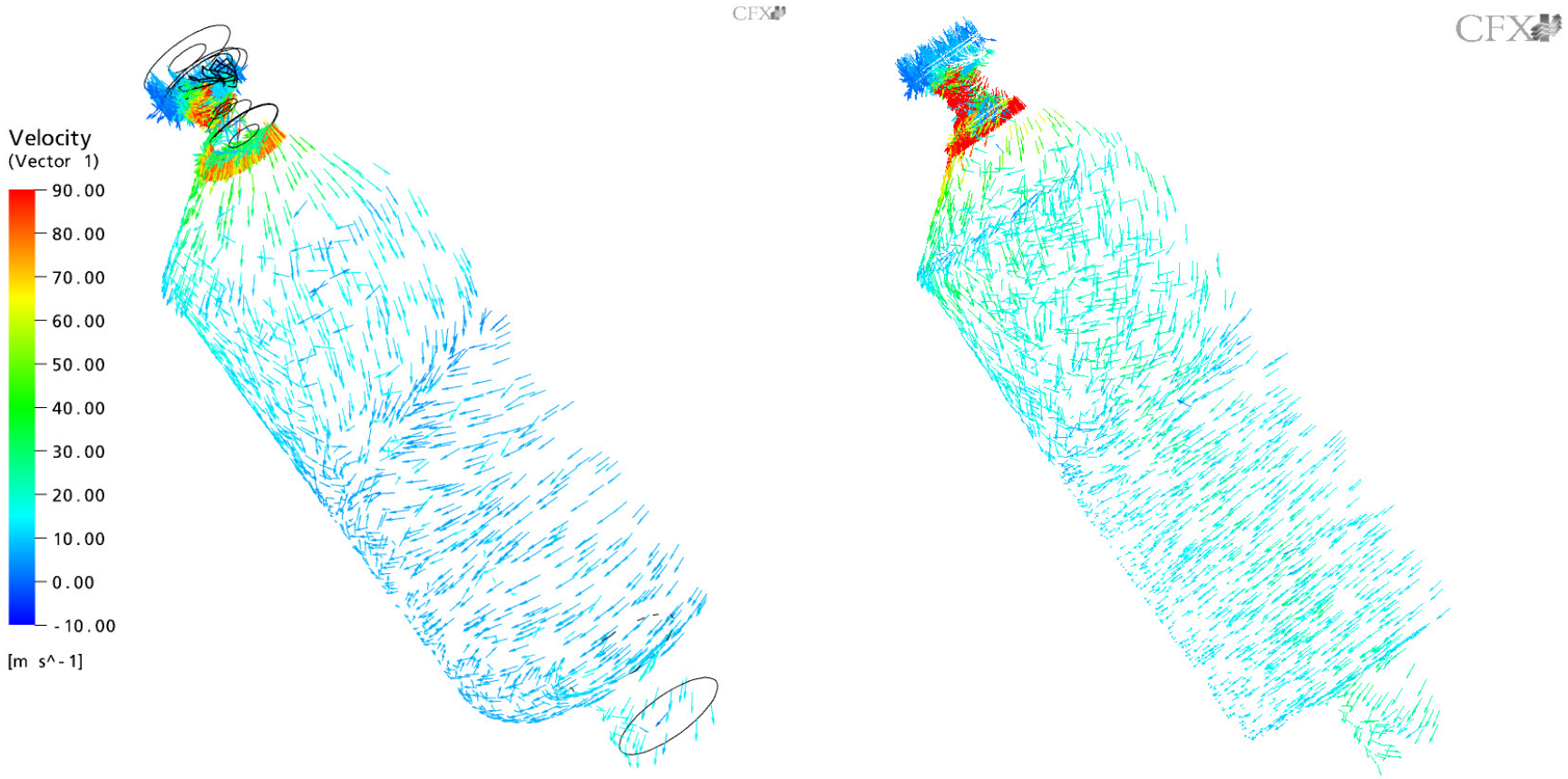

Figure 5-19: 3-D vector plot of velocity for the low swirl vanes (left), and high swirl vanes (right)

5.5.6 Comparing the Low and High Swirl Vorticities

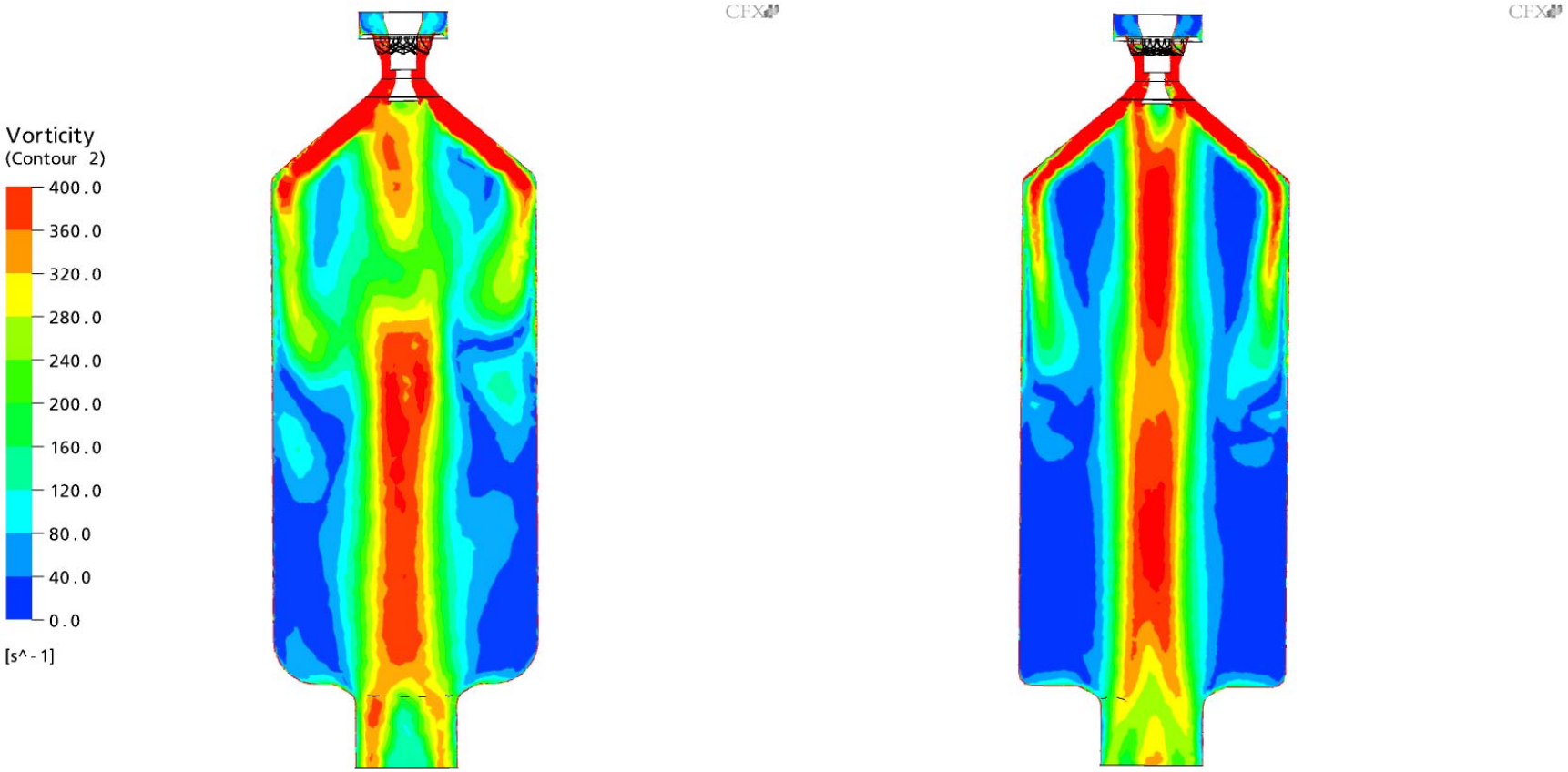

Figure 5-20: Plot of vorticity on a central plane for the low swirl vanes (left), and high swirl vanes (right)

There is a central hollow tube-shaped region of high vorticity ranging up to 400 s^{-1} in the high swirl plot. The low swirl plot shows less uniformity and no structured central core region of vorticity apart from in the lower section of the chamber. Both plots show a low region of vorticity between 80 – 120 s^{-1} in the central section of the chamber, with increasing vorticity towards the centre ranging from 280 – 320 $s^{-1}$and then from 360 to 400 s^{-1}.

5.5.7 Comparing the Low and High Swirl Particle Tracking

The aim was to simulate the particle tracks of dried sludge particles (15 μm < d_p < 1500 μm) using CFD, to ascertain what influence the two different swirl vanes have on the projection of the particles. It is to be noted that all particles simulated by the particle tracks terminate their tracking motion when they hit the wall in the top section of the primary chamber. 500 particles were simulated for each setup, and 50 of these particles were selected to visualise the particle path distributions in the chamber.

Figure 5-21 provides a side view, comparing the selected particle paths of the dried sludge particles for the high and low swirl vane setups. In the high swirl setup the smaller particles (~200 μm) are influenced and entrained by the swirling gas flow in the top section and are forced out to the sides of the chamber. The recirculation regions formed by the high swirl influence and entrain the particles as shown in Figure 5-21. In comparison the swirling motion generated by the low swirl does not influence the particles nearly as much as the high swirl. This is shown by the particles having a more rigid and straight path as they are less affected tangentially by the swirl. Figure 5-22 provides a tilted view (from the bottom of the primary combustion chamber), tracking the influence of the swirl on the dried sludge particles in both swirl setups, which reinforces that the smaller particles are influenced more so by the high swirl scenario.

Larger particles (~1000 μm) in both of the vane setups show a more rigid and straight path because they are less affected tangentially by the swirl and therefore take less time to hit the walls of the chamber. This is shown in Figures 5-21 and 5-22.

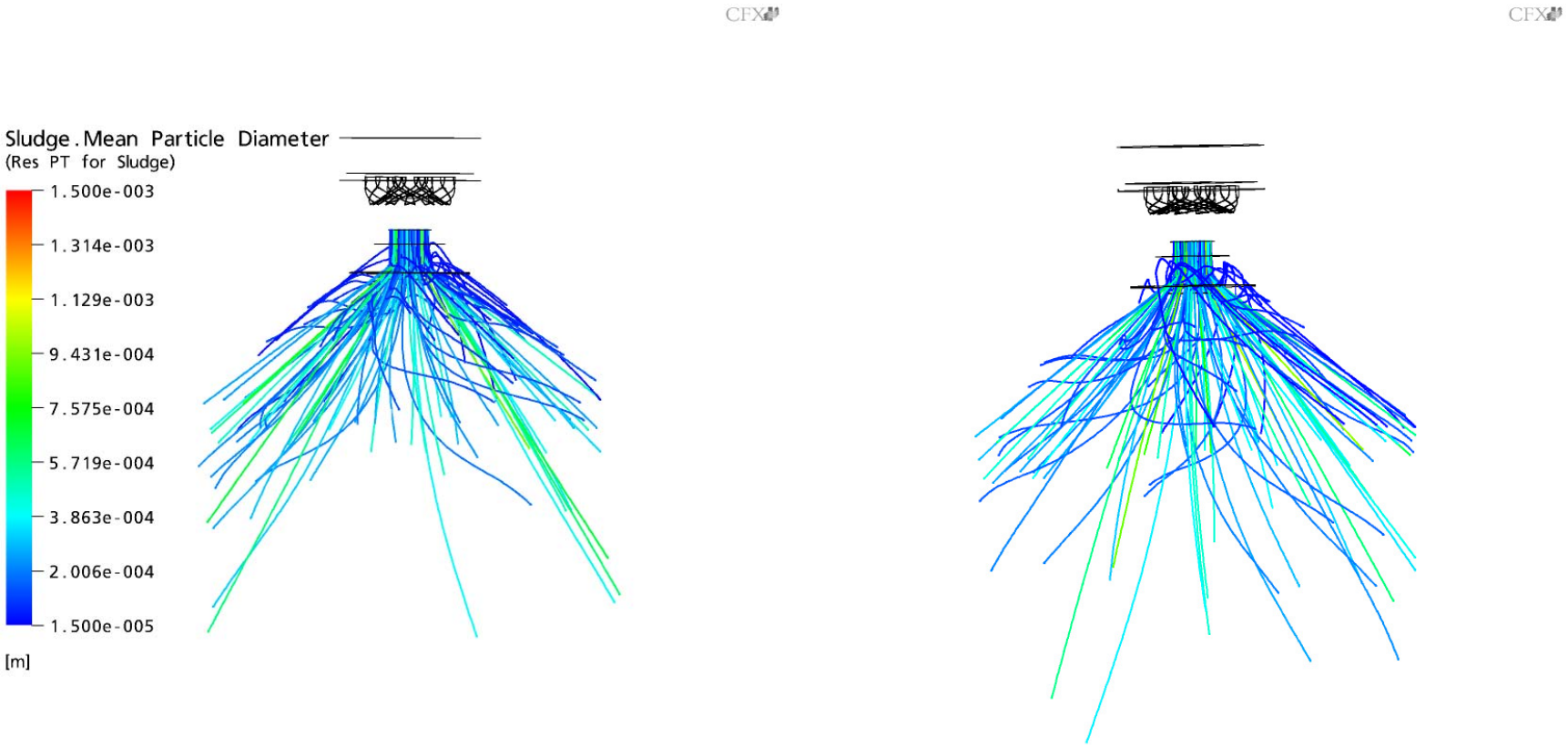

Figure 5-21: Selected particle paths coloured by particle diameter in metres. Low swirl vanes (left), and High swirl vanes (right)

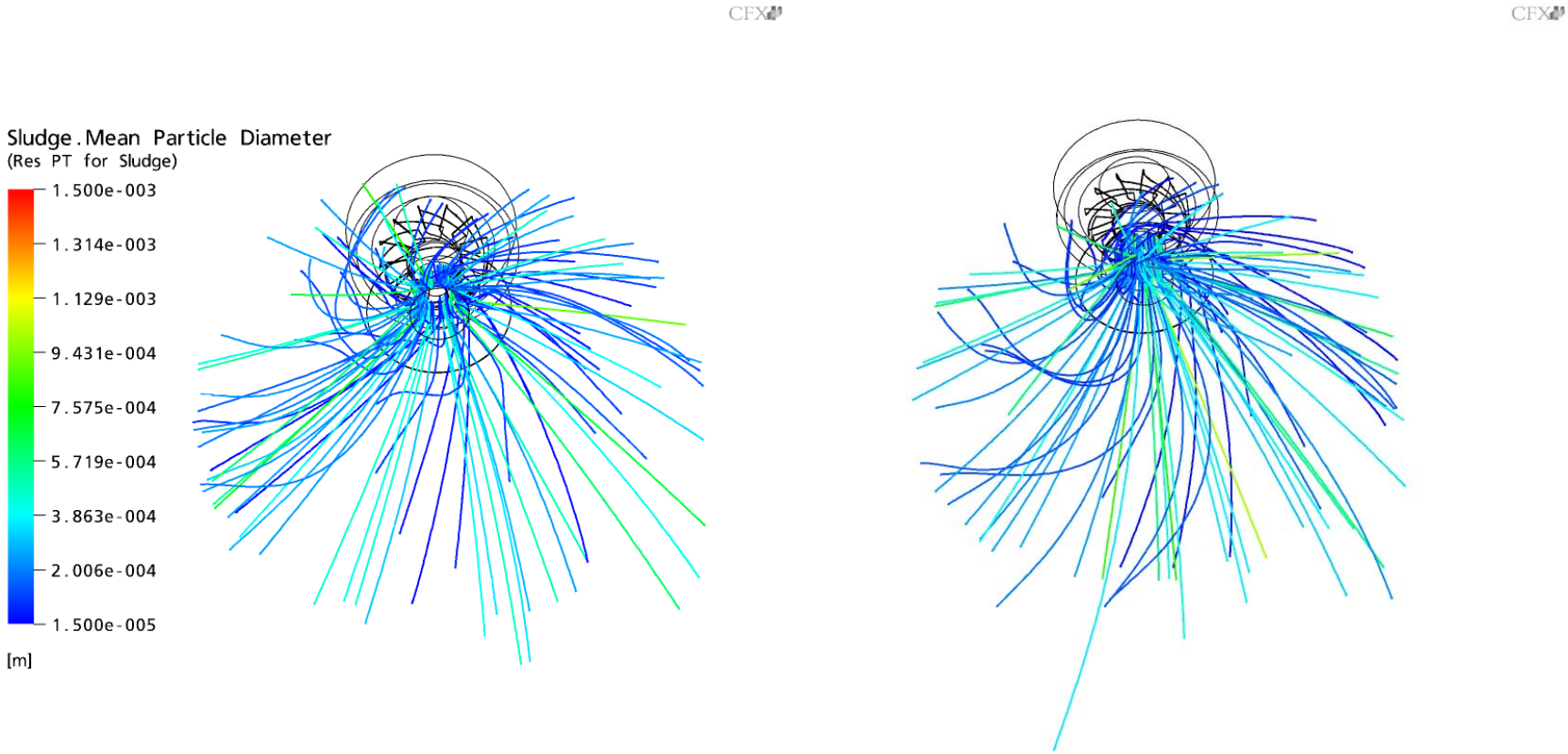

Figure 5-22: Particle path distributions looking up from the bottom and side of the primary combustion chamber. Low swirl vanes (left), and High swirl vanes (right)

5.6.1 Discussion of the Steady State Tangential Velocity Profiles for the High and Low Swirl Vane Modelling Results

With reference to Figures 5-7, 5-8, 5-10 and 5-12 it can be said that the high swirling flows from the high swirl vane setup illustrated the "Rankine vortex" consisting of an outer free vortex and a solid-body rotation at the core region – as described by Wakelin (1993) and shown in Figure 3-1. The high swirl tangential velocity in each of the Figures showed that the central region in the swirl burner rotated like a solid body where the tangential velocity and radius increased. The high swirl results also demonstrated that the tangential velocities in the flow field were moving towards zero at the axis of symmetry as also experienced by Wakelin (1993).

With the exception of Figures 5-9 and 5-12, all the low swirl tangential velocity graphs showed a resemblance of the "Rankine vortex". This showed the low swirl tangential velocity profile in the primary combustion chamber (0.300 m below the vanes) tending negative between approximately 0.2 and 0.25 m away from the chamber wall.

This resulting negative tangential velocity was questionable and was considered as an effect of the unsteadiness in the solution of the low swirl setup in the primary combustion chamber (0.300 m below the vanes). i.e. that the flow in this region was exhibiting cyclical behaviour. Many flows, particularly those driven by buoyancy, do not have a steady state solution, and therefore could indicate transient behaviour (Anon, 2005). The reason for simulating both the low and high swirl scenarios in steady state was to investigate whether the resultant swirl setups contained a steady state solution. The output results files from the steady state simulations were used to run the transient simulations. Further investigations into transient simulations are detailed in **Chapter 6 – Transient Simulations for the High and Low Swirl Vane Setups**.

5.6.2. Discussion of the Steady State Axial Velocity Profiles for the High and Low Swirl Vane Modelling Results

In Figure 5-7 the high and low swirl axial profiles displayed traits similar to Swithenbank et al's work (1969) where at a sufficient degree of swirl, an internal recirculation zone is generated. According to Ganesan, 1974, a recirculation zone is caused by an imbalance between the adverse pressure gradient along the jet axis and the kinetic energy of the fluid particles flowing in the axial direction.

Both the high and low axial velocity profiles in Figure 5-8 demonstrate an initial negative velocity indicating a reversal in flow and back mixing. This reversal in flow is due to the high swirl being generated by the swirl vanes below the fuel deflector cone.

When discussing Figure 5-8, the region in the primary combustion chamber (Figure 5-9) was described as being highly turbulent. Hence the swirl generated by both the high and low swirl vanes was high enough to generate an internal recirculation zone. Figures 5-15 and 5-16 show traits of a vortex breakdown in the high and low swirl vane setups, in particular a **'precessing vortex core' or PVC** in the primary combustion chamber as described by Syred and Beer (1972). Both profiles showed the presence of a distorted negative flow region causing a `kidney shape' recirculation zone to be formed which Syred et al also experienced in 1997.

The high and low swirl axial velocity profiles (Figures 5-11 and 5-13) again generated a negative region of velocity, indicating a reversal flow inside the core vortex and back mixing. The negative axial velocity regions generated by the high swirl and low swirl vanes reconfirm the findings of earlier studies and published literature by (Ganesan, 1974) and (Huang and Tsai, 2001).

Figures 5-18 and 5-19 showed the velocity vector plots on a central plane and the formation of the recirculation zones in the main body of the primary chamber for both swirl setups, by demonstrating a reversal of flow in the main chamber. This was demonstrated by the upward direction of the velocity vector arrows in the top half of the chamber. The high swirl setup demonstrated a more turbulent swirling motion in the chamber compared to the low swirl setup by the vector activity in opposing directions.

5.6.3 Discussion of the Steady State Particle Tracking for the High and Low Swirl Vane Modelling Results

The particle tracks of the dried sludge particles (15 μm < d_p < 1500 μm), using CFD, were simulated to ascertain what influence the two different swirl vanes had on the projection of the particles. Figures 5-21 and 5-22 illustrated that the high swirling flow generated by the high swirl setup influenced and entrained the smaller particles (~200 μm) and forced these particles out to the sides of the chamber, whereas the low swirl setup had a limited/non-existent influence over the particles. The low swirl lack of influence and entrainment is demonstrated by the particles following a more rigid and direct path due to the lower swirl generated. The larger particles (~1000 μm) in both of the vane setups showed a more rigid and straight path as the particles were not entrained and influenced by the swirling gas flow.

Further to simulating the particle tracks of dried sludge particles (15 μm < d_p < 1500 μm) using CFD, a separate case study was undertaken (requiring no CFD) to investigate the previous experimentation by Davis et al (1986 and 2002) – Refer to **Chapter 3 – Section 3.4 Background to the Mechanics of Small Particles Colliding with a Wet Surface**.

The theory and previous experimentation by Davis et al was applied to the particle impaction of the dried sludge particles (200 μm < d_p < 1000 μm) on Lemar's furnace wall. Davis et al. (1986) showed that the particles did not rebound when the Stokes number was less than a critical value ($St < St_c$), due to viscous dissipation of the initial kinetic energy of the sphere. Rebound was predicted for $St > St_c$.

A spreadsheet was created to determine the Stokes number (St), the critical Stokes number (St_c), and the elasticity parameter (ε) for a dried sludge particle impacting on a hot furnace wall at 1100 °C for the Lemar setup. This temperature of 1100 °C is where the slag is a viscous fluid and was the assumed value for film movement to occur provided by Lemar – Refer to Appendix 9.1. An impact velocity (Vo) for the dried sludge particle was assumed to be 30 m/s, which is the maximum gas velocity from the fuel entry determined by CFD modelling. As no data was available for Young's modulus of elasticity for dried sewage sludge or slag, the data used in this model was that for fly ash, which closely resembles the physical properties of dried sewage sludge, and soda-lime glass to resemble the vitrified viscous fluid. The viscosity of the viscous fluid was 18.7 Pa.s and this depended on the thickness of the viscous slag layer (Xo) being 0.002 m. Table 5-1 shows the Stokes Number, Critical Stokes Number, and the Elasticity Parameter for particles impacting a hot furnace wall at 1100 °C.

Table 5-1: Shows the Stokes Number, Critical Stokes Number, and the Elasticity Parameter for particles impacting a hot furnace wall at 1100 °C.

Particle Size (μm)	Stokes Number (St)	Critical Stokes Number (St_c)	Elasticity Parameter (ε)
200	0.043	5.57	5.38×10^{-7}
400	0.086	5.16	1.52×10^{-6}
600	0.128	4.92	2.79×10^{-6}
800	0.171	4.74	4.30×10^{-6}
1000	0.214	4.61	6.01×10^{-6}

From Table 5-1, the Stokes numbers determined for all particle diameters (200 μm < d_p < 1000 μm) were less than the Critical Stokes Number value ($St < St_c$), indicating that in theory the dried sludge particles (200 μm < d_p < 1000 μm) should stick to the furnace wall for a maximum impact velocity of 30m/s. However, in real life experimentation, when undertaking the Lemar Vitrification Process there is inefficient capture of the particles in the slag layer.

No transient CFD modelling was undertaken to investigate the transient nature of the particle tracking and to verify that particles between the diameters of 200 to 1000 μm would stick to the furnace wall. Investigating transient particle tracking, together with the results from this case study, would provide an overall interpretation as to whether or not the dried sludge particles bounced or stuck to the viscous slag layer and a commentary as to their movements in the chamber.

Hence, transient modelling of the particle tracks is recommended for the next phase of the project – refer to **Chapter 7 – Section 7.5 Recommendations for the Project**.

6. Transient Simulations for the High and Low Swirl Vane Setups

6.1 Background to Transient Simulations

Transient behaviour (i.e. non steady state circumstances) often occurs at start-up or by fluctuating flow characteristics. Transient simulations require real time information to determine the time intervals at which the ANSYS CFX-Solver calculates the flow field. Many flows, particularly those driven by buoyancy, do not have a steady state solution, and therefore may exhibit cyclical behaviour which will inhibit convergence, irrespective of the action taken with regard to mesh quality and time step size. These cyclical flow characteristics indicate transient behaviour. The drawbacks of transient simulations include high computational cost and large amounts of storage required to hold the transient data.

6.2 The CFX Simulation

3D simulations of the gas flow inside the primary combustion chamber were carried out using the commercial CFD package CFX 10.0. The transient simulations possessed the same physical parameters and inputs as the steady state simulations, described in Chapter 5. An unstructured mesh was used with five inflation layers at the walls to ensure boundary layer effects were properly captured. Unstructured meshing of the primary combustion chamber and swirl burner took place using the mesh building code ICEM CFD. The mesh density was increased in the region around the swirl vanes and the cone in the top section of the chamber where large gradients exist.

The maximum number of time steps was set at 500 and the simulations gave solutions that converged with good residuals. A convergence criterion of a maximum residual of 1×10^{-4} was used to terminate the coefficient iterations. Usually only two or three iterations at each time step were required when using a time step of 0.01s. This signified that the solution was converging successfully.

The chamber walls were treated with the default CFX 10.0 boundary conditions of no slip, with smooth, adiabatic walls. An average static pressure of 0 atmospheres was specified at the outlet air duct. A comparison took place for the high and low swirl at an isothermal temperature of 240 °C. Velocity components in the x, y and z directions, along with the vorticity and temperature were recorded for each time step.

CFD modelling of the primary chamber and swirl burner took place with the addition of an external heat source which caused the temperature to rise within the chamber. An energy source of 300,000 Wm^{-3} was simulated over the whole primary chamber. The low swirl vane setup was used in this study as this physical setup best represents the setup currently used at the Lemar Vitrification Plant.

Snapshot images were formatted and generated for tangential velocity, axial velocity, vorticity, and vector velocity plots for both the high and low swirl vanes. Table 6-1 shows the number of snapshot images generated for the velocity profiles.

Table 6-1: Shows the number of snapshot images generated for the velocity profiles

Velocity Profiles	Number of Snapshot Images Generated
Axial Velocity – High Swirl Vane Setup	220
Axial Velocity – Low Swirl Vane Setup	220
Tangential Velocity – High Swirl Vane Setup	219
Tangential Velocity – Low Swirl Vane Setup	219
Vorticity – High Swirl Vane Setup	220
Vorticity – Low Swirl Vane Setup	220
Vector Velocity – High Swirl Vane Setup	181
Vector Velocity – Low Swirl Vane Setup	181
External Heat Source Addition – Axial Velocity – Low Swirl Vane Setup	97
External Heat Source Addition – Tangential Velocity – Low Swirl Vane Setup	97
External Heat Source Addition – Vorticity – Low Swirl Vane Setup	97
External Heat Source Addition – Vector Velocity – Low Swirl Vane Setup	97

6.3 Velocity Profiles

Results of the two-phase CFD model of the primary chamber for both the high and low swirl vanes are presented below in a series of plots as well as 'movie files'. These 'movie' files can be viewed on the attached DVD which are in .avi format.

The following four .avi 'movie' files (bracketed and identified) are a comparison of the high and low swirl for the respective variables (for axial velocity, tangential velocity, vorticity, and vector velocity plots) at an isothermal temperature of 240 °C. In each of these four 'movies', the high swirl setup is located on the left-hand side and the low swirl setup is located on the right.

- Axial Velocity Comparison: **AxialVelComparison.avi**
- Tangential Velocity Comparison: **TangentialVelocityComparison.avi**
- Vorticity Comparison: **VorticityComparison.avi**
- Vector Velocity Comparison: **VectorVelocityComparison.avi**

The remaining four .avi 'movie' files (bracketed and identified below) are a comparison of both the low swirl results from above (isothermal temperature of 240 °C), and the results obtained from the addition of an external heat source (300,000 Wm^{-3}) and reached a maximum temperature of 1373 °C. In each of these four 'movies', the isothermal results are located on the left-hand side and the external heat source results are located on the right.

- Comparison between the Isothermal and Heat Source Simulations - Axial Velocity: **HeatSourceAxialVelComparisonLowSwirl.avi**
- Comparison between the Isothermal and Heat Source Simulations – Tangential Velocity: **HeatSourceTangentialVelocityComparisonLowSwirl.avi**
- Comparison between the Isothermal and Heat Source Simulations – Vorticity **HeatSourceVorticityComparisonLowSwirl.avi**
- Comparison between the Isothermal and Heat Source Simulations – Vector Velocity: **HeatSourceVectorVelocityComparisonLowSwirl.avi**

Figures 6-1 to 6-12 provide an overall representation of the respective transient simulation i.e. a cyclical change in the gas flow. It is recommended that the reader views the attached DVD as it simulates the entire process. The frame rate for each DVD is 29 frames/second.

Table 6-2 below shows the elapsed time and the number of cycles for each of the transient simulations.

Table 6-2: Shows the elapsed time and the number of cycles for each of the transient simulations

Simulation Type	Number of Cycles during Simulation	Simulation Elapsed Time (s)	Cycles per Second (Hz)
High swirl vane setup	10	7	1.43
Low swirl vane setup	16	7	2.29
External Heat Source Addition – Low swirl vane setup	5.5	3	1.83

The 'movie' for the high swirl transient simulation (on the left hand side) exhibited 10 cyclical surges every 7 seconds (1.43 Hz) compared to the low swirl simulation that showed 16 cyclical surges every 7 seconds (2.29 Hz).

The 'movie' for the isothermal transient simulation (on the left hand side) shows 16 cyclical surges every 7 seconds (2.29 Hz) compared to the addition of an external heat source simulation showing 5.5 cyclical surges in 3 seconds (1.83 Hz).

6.3.1 Axial Velocity Comparison

As mentioned previously, Figures 6-1 and 6-2 illustrate only one cycle of the process for the high and low swirl vane setups. This comparison between the high and low swirl axial velocities can be viewed on **AxialVelComparison.avi** (refer to attached DVD).

The low swirl setup illustrated a positive 'scrambled' gas velocity (between 0 to 5 m/s) in the lower central section of the chamber, which followed a cyclical trend. The top section of the chamber showed positive gas velocities near the wall (between 10 to 15 m/s) and halfway through the length of this particular simulation, there was evidence of high positive velocity (between 10 to 15 m/s) coming from the throat and extending one-third of the length of the chamber. The high positive velocity indicated positive mixing through the bottom end of the chamber and this was carried through to the lower chamber walls. Low negative velocities were also evident throughout the central region of the chamber and were constantly fluctuating and pulsating, indicating back mixing.

In comparison, the high swirl setup illustrated a negative velocity region between -15 to -5 throughout the centre of the chamber showing a precessing vortex and also indicating back mixing. A symmetrical gas flow, in the range between 0 to 5 m/s, similar to the 'scrambled' velocity evident in the low swirl setup, was present on the outside of the central core. The high swirl setup showed high positive gas velocities near the wall of the throat.

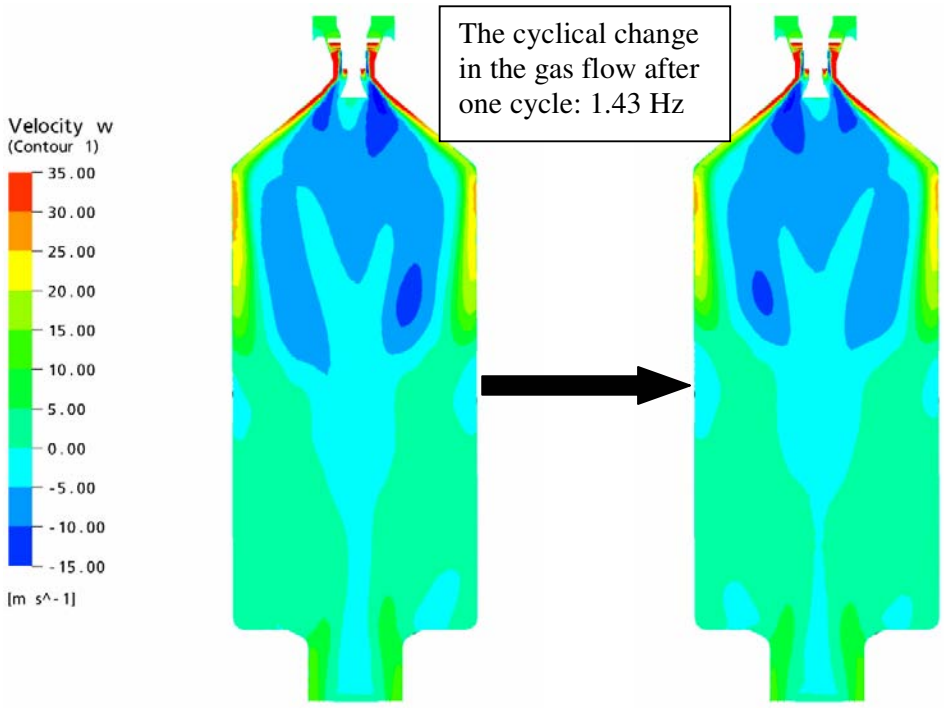

Figure 6-1: Shows one cycle of the axial velocity simulation for the high swirl vane setup.

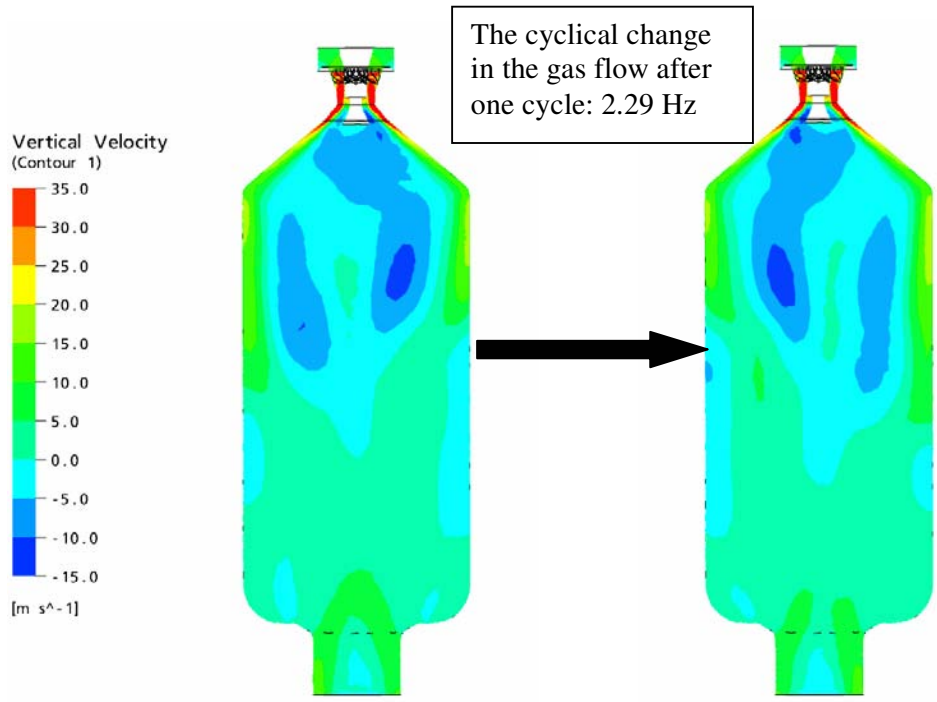

Figure 6-2: Shows one cycle of the axial velocity simulation for the low swirl vane setup.

6.3.2 Tangential Velocity Comparison

Figures 6-3 and 6-4 compare the tangential velocity for the high and low swirl vane setups for one cycle of the process. This can be viewed on **TangentialVelocityComparison.avi** (refer to attached DVD).

The high swirl setup showed a well defined central core region of gas flow from the top of the chamber to the throat. On either side of this strong central core region, there was a symmetrical surging gas flow (between 20 to 30 m/s), which pulsed vertically along the central plane. However there were traces of low flow (between 0 to 10 m/s) circulating vertically on the central plane inside the central core. The velocity near the wall in the top half of the chamber ranged from 0 to 10 m/s and between 10 to 20 m/s in the bottom section.

In comparison, the low swirl setup illustrated a thin central core region of flow between 0 to 10 m/s. As with the tangential velocity high swirl transient setup, the low swirl scenario contained two velocity regions on either side of this central core (between 10 to 20 m/s). However in the low swirl, the regions were not as well defined and were constantly changing shape and direction. This was because the low swirl setup exhibited a fluctuating motion which resulted in a more distinct and rapid change in the gas flow. The rest of the primary chamber had a gas velocity which was between 0 to 10 m/s.

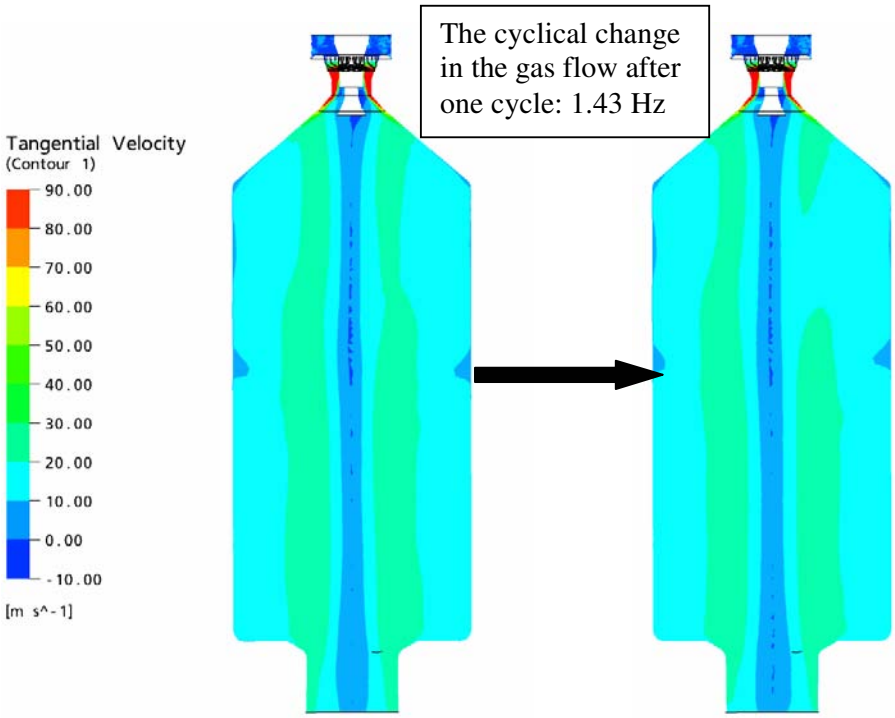

Figure 6-3: Shows one cycle of the tangential velocity simulation for the high swirl vane setup.

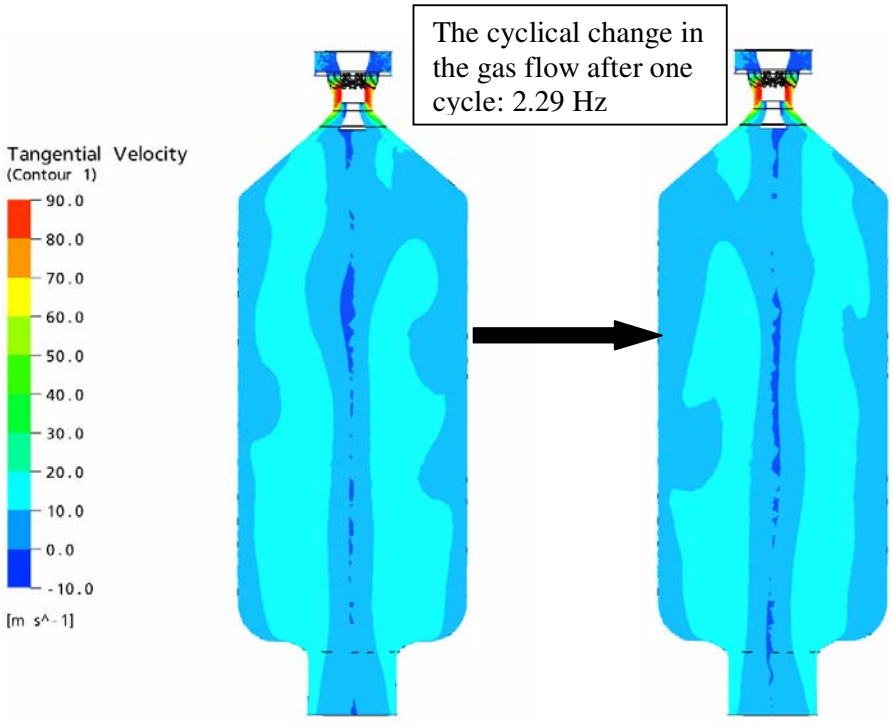

Figure 6-4: Shows one cycle of the tangential velocity simulation for the low swirl vane setup.

6.3.3 Vorticity Comparison

Figures 6-5 and 6-6 illustrate vorticity for one cycle of the process for both the high and low swirl vane setups and this comparison can be viewed on **VorticityComparison.avi** (refer to attached DVD).

The high swirl setup exhibited a very strong, symmetrical rigid central core region of vorticity of approximately 400 s^{-1}. This central core was made up of smaller vorticity regions of between 200 to 320 s^{-1} and on either side of it, in the top section of the chamber nearest the wall, were regions of similar strength vorticity. In the bottom section on either side of this central core, were small vorticity regions (between 0 to 80 s^{-1}).

In comparison, the low swirl setup showed a central core region of the same strength vorticity although this was not as prominent as with the high swirl which had a more solid core. The highest vorticity regions were present in the central and lower regions of the chamber, with the vorticity regions on either side of the central zone varying from 240 s^{-1} to approximately 360 s^{-1}. On either side of the top section of the chamber was a strong vorticity region that extended approximately one-third of the chamber length, and which was continually pulsing and surging. The vorticity throughout the chamber was not as stable as in the high swirl setup due to the low swirl's continuous high frequency that caused this instability.

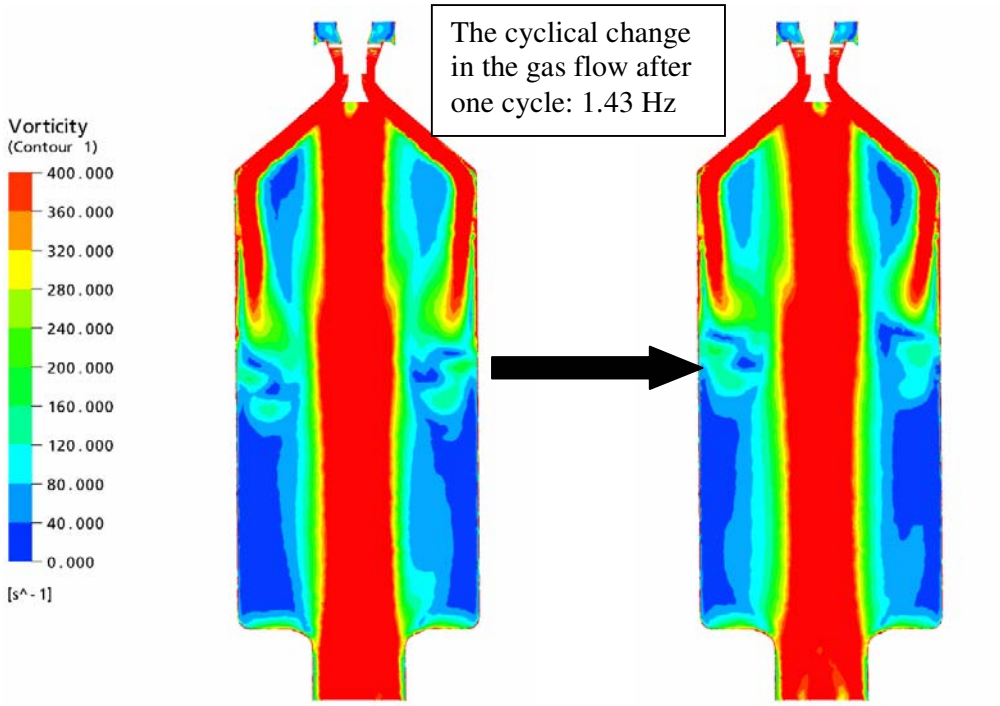

Figure 6-5: Shows one cycle of the vorticity simulation for the high swirl vane setup.

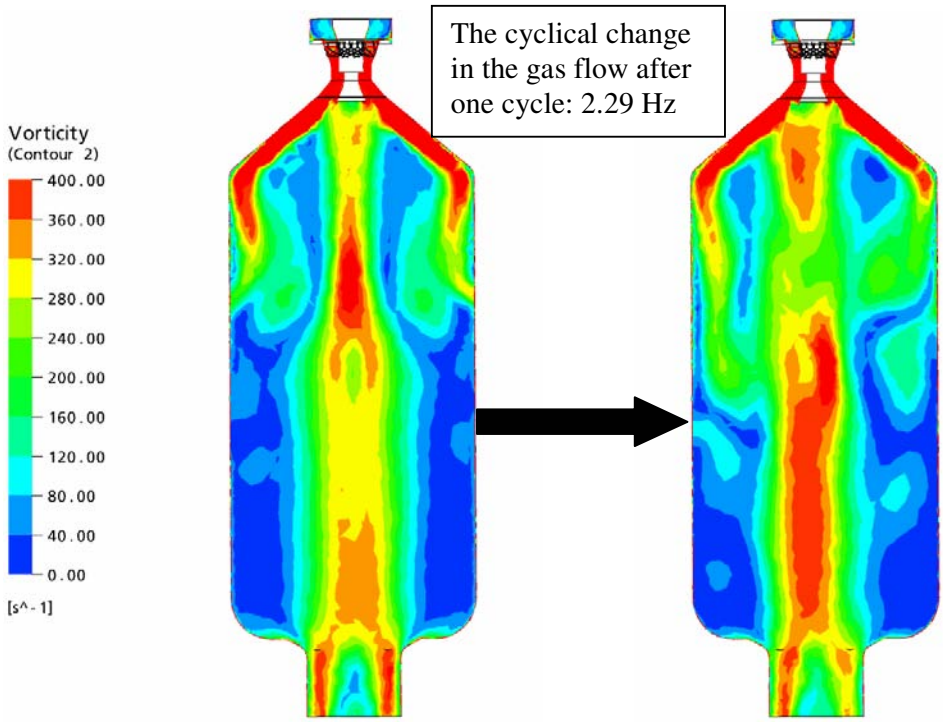

Figure 6-6: Shows one cycle of the vorticity simulation for the low swirl vane setup.

6.3.4 Vector Velocity Comparison

Figures 6-7 and 6-8 illustrate the vector velocity for one cycle of the process for both the high and low swirl vane setups. This comparison can be viewed on **VectorVelocityComparison.avi** (refer to attached DVD).

The high swirl setup showed recirculation of the gas velocity in the top half of the chamber by the constant vector activity in opposing directions. However, this movement was confined to the top half of the chamber due to the strong recirculation zones created.

In comparison the low swirl simulation showed rapid surges of recirculation in the central section of the chamber, which reinforced the point conveyed in the axial velocity simulation where there were rapid surges and recirculation zones that occurred in the central region. Again, there was intense pulsating behaviour and large variations in vector directionality, which extended two-thirds down the length of the primary chamber, indicating reversal of gas flow.

These vector profiles in both the high and low swirl comparisons illustrated the gas flow activity in the chamber more effectively than any of the other CFX-Post visual techniques.

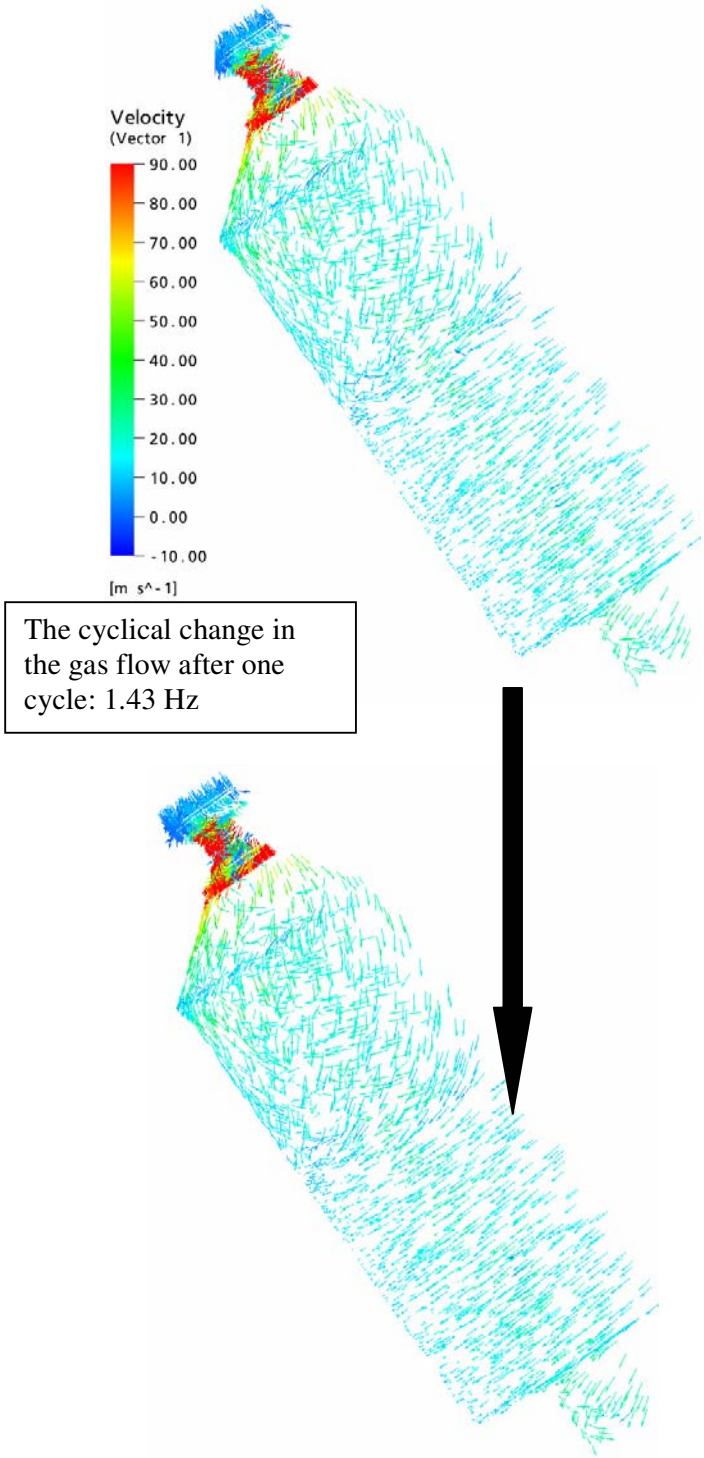

Figure 6-7: Shows one cycle of the vector velocity simulation for the high swirl vane setup.

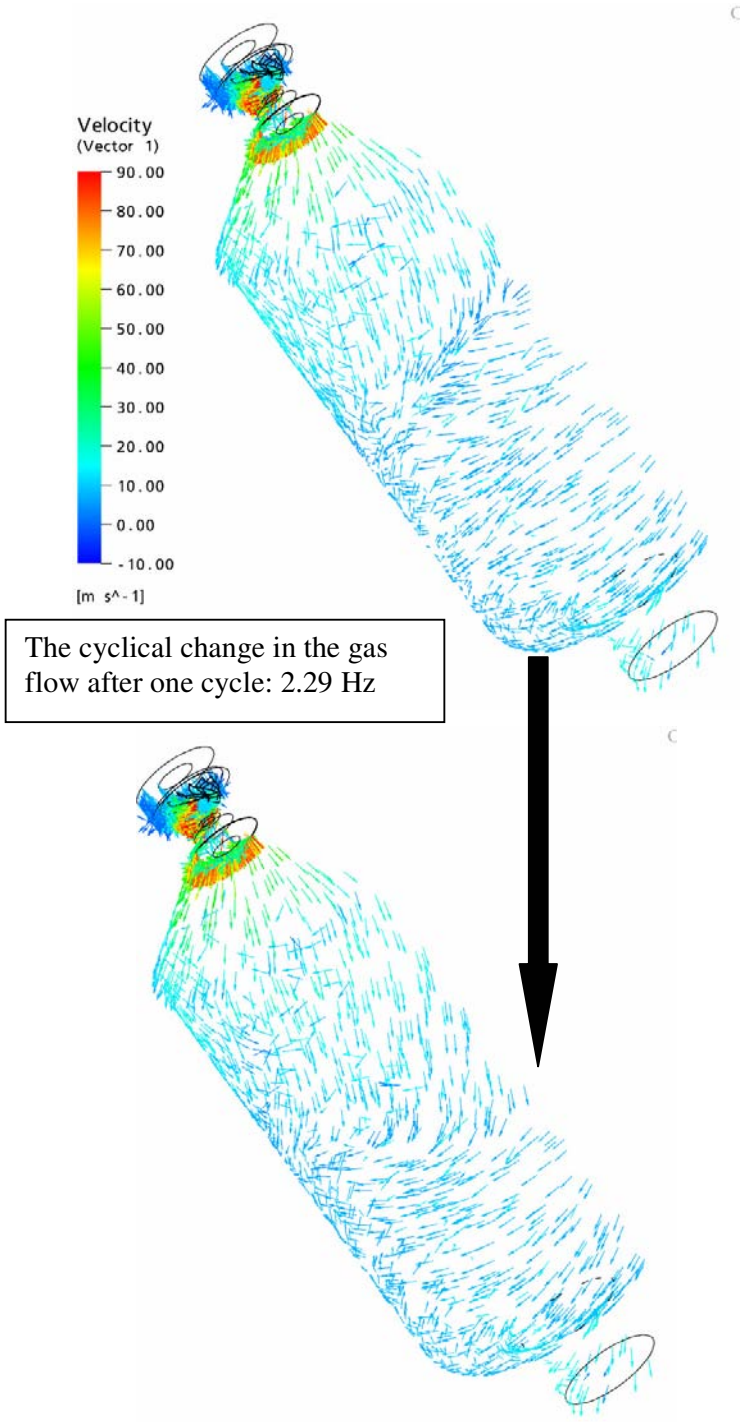

Figure 6-8: Shows one cycle of the vector velocity simulation for the low swirl vane setup.

6.3.5 Comparison between the Isothermal and Heat Source Simulations- Axial Velocity - Low Swirl Vane Setup

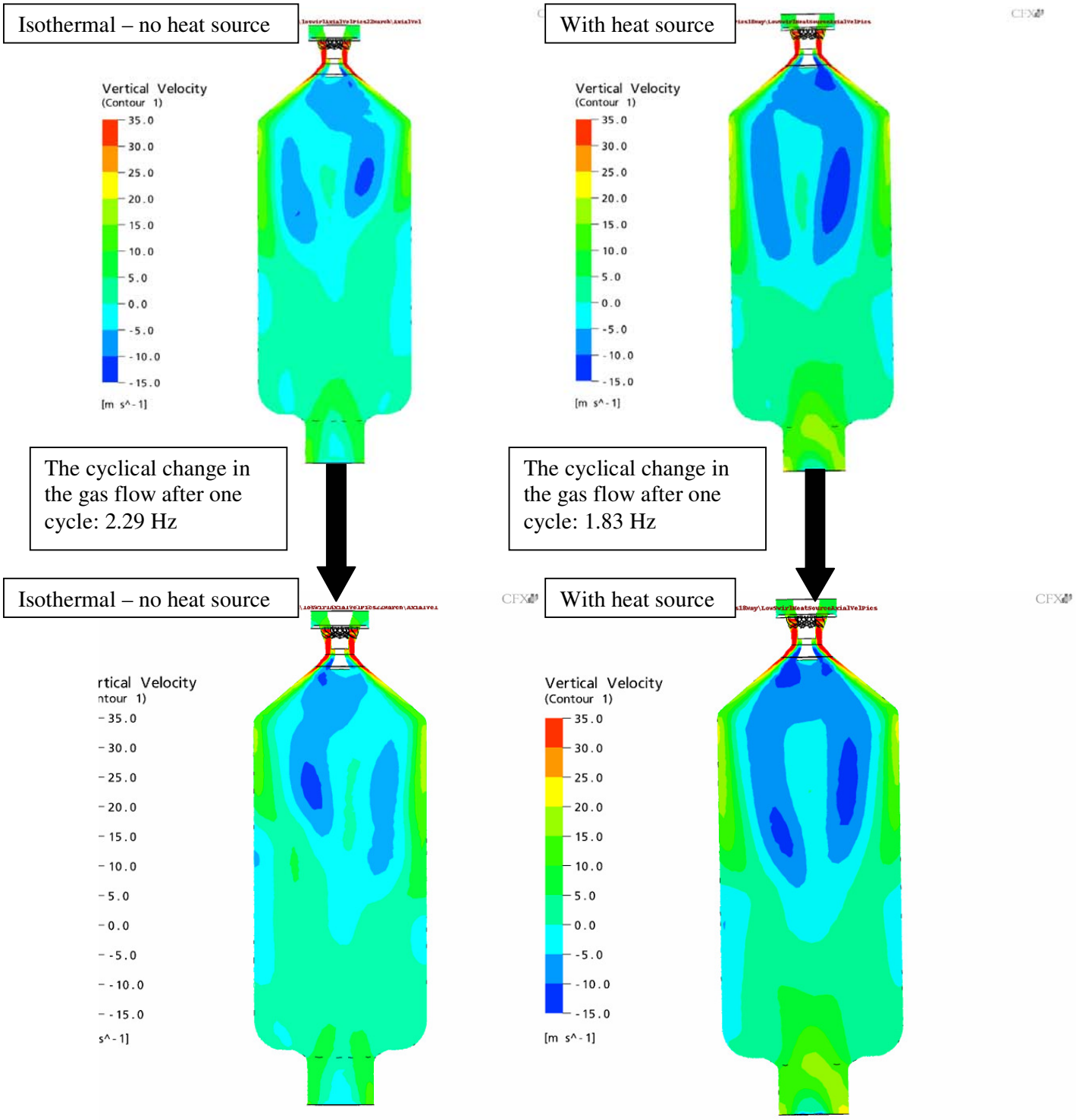

Figure 6-9: Shows one cycle for both the isothermal axial velocity (left), and heat source axial velocity (right)

Figure 6-9 compares the isothermal axial velocity and the heat source axial velocity for one cycle of the process for the low swirl vane setup. This comparison can be viewed on **HeatSourceAxialVelComparisonLowSwirl.avi** (refer to attached DVD).

The addition of the heat source stabilised the swirling flow causing the recirculation regions to increase and lengthen, and the frequency of the surges to decrease from 2.29 Hz to 1.83 Hz. With heat addition the recirculation regions intermixed more and lengthened and widened to up to three-quarters of the length of the primary chamber. This negative flow reached the side of the walls at the bottom of the chamber.

6.3.6 Comparison between the Isothermal and Heat Source Simulations- Tangential Velocity - Low Swirl Vane Setup

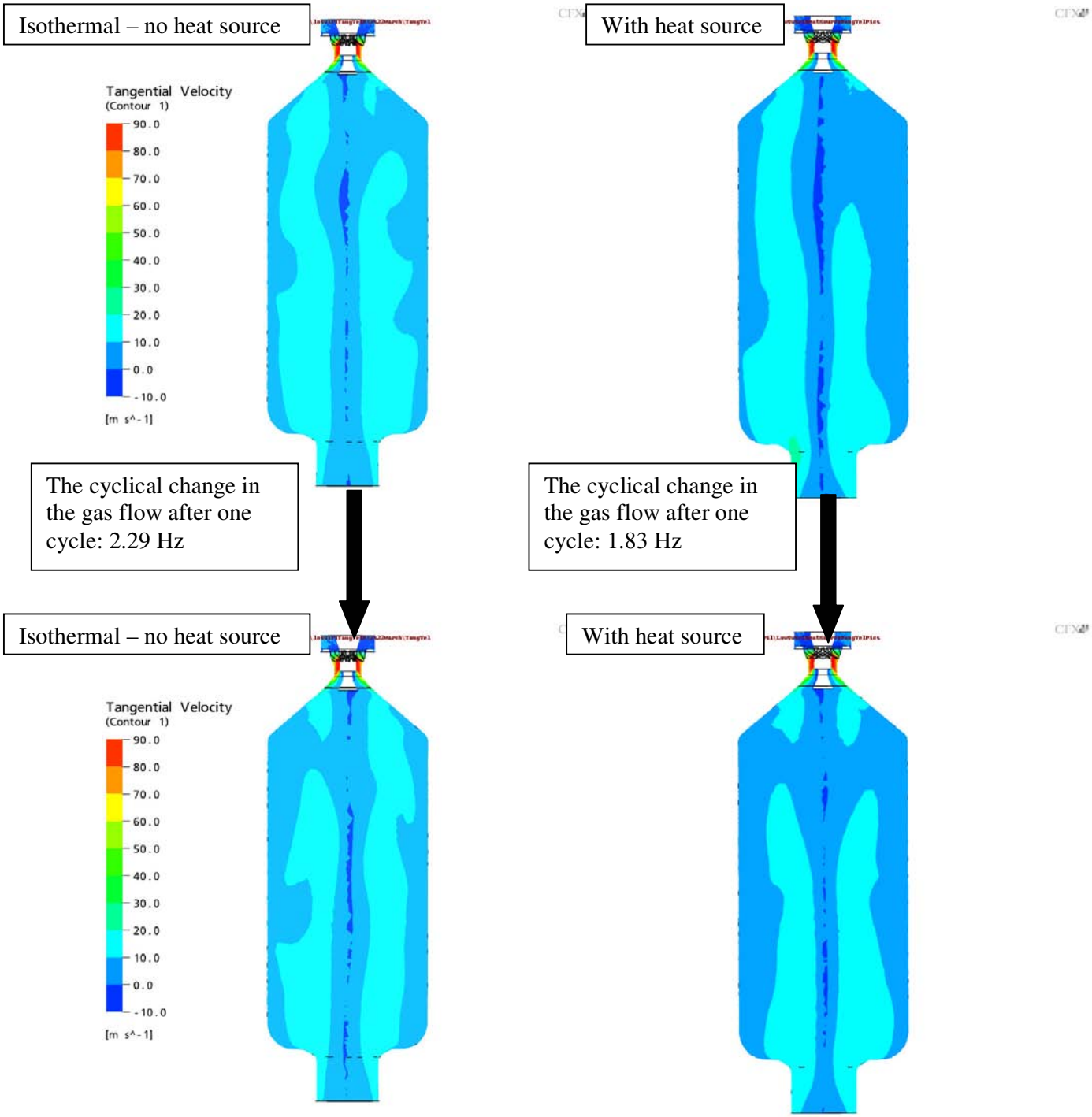

Figure 6-10: Shows one cycle for both the isothermal tangential velocity (left), and heat source tangential velocity (right)

Figure 6-10 compares the isothermal tangential velocity and the heat source tangential velocity for one cycle of the process for the low swirl vane setup. This comparison can be viewed on **HeatSourceTangentialVelocityComparisonLowSwirl.avi** (refer to attached DVD).

In this transient simulation the only difference identified was the positive surges of gas flow (approximately 50 m/s) from the throat region that were evident in the heat source setup. Therefore these simulations are very similar which indicates that the tangential velocity was not affected by the addition of an external heat source.

6.3.7 Comparison between the Isothermal and Heat Source Simulations- Vorticity - Low Swirl Vane Setup

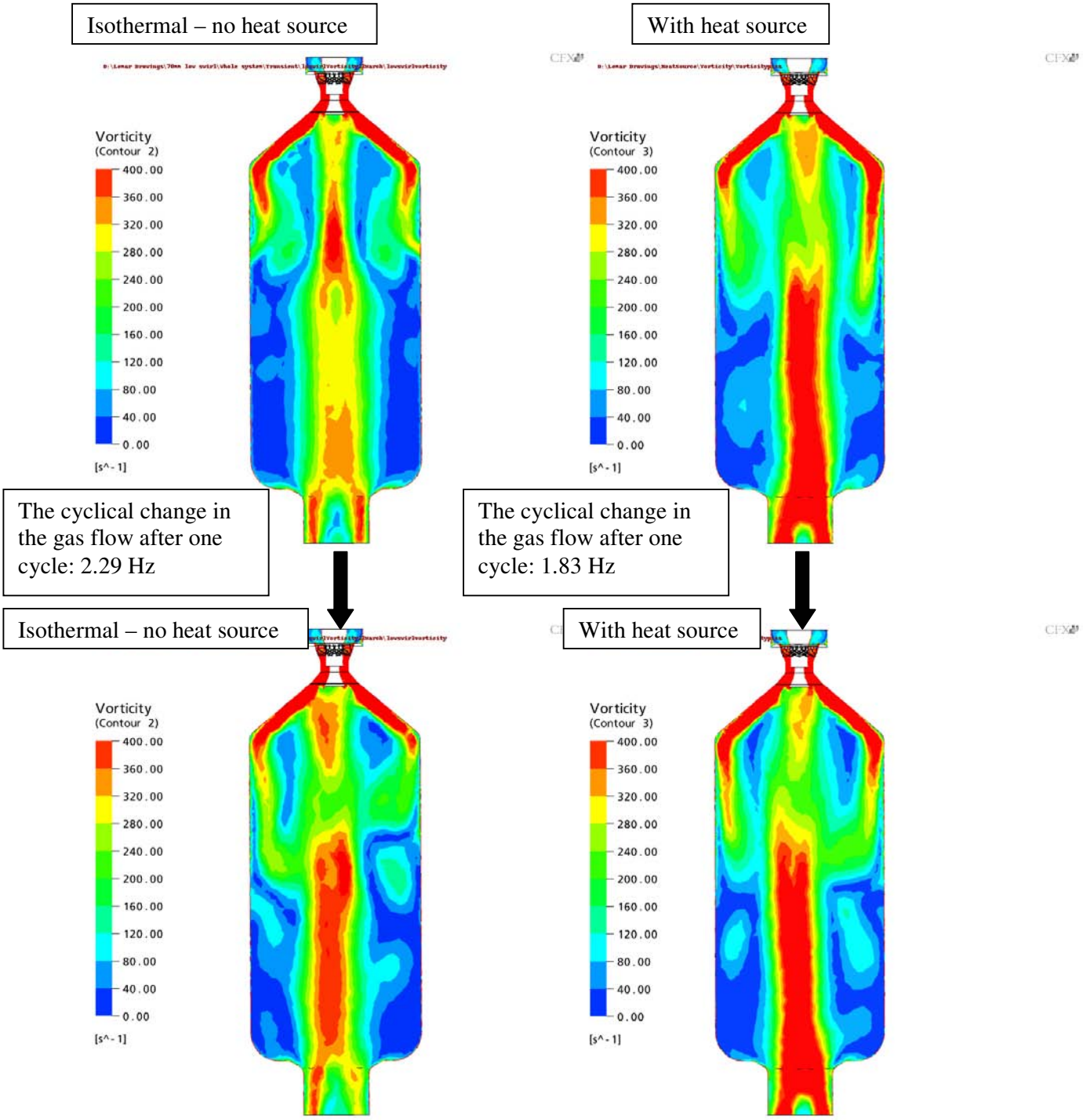

Figure 6-11: Shows one cycle for both the isothermal vorticity (left), and heat source axial vorticity (right)

Figure 6-11 compares the isothermal vorticity and the heat source vorticity for one cycle of the process for the low swirl vane setup. This comparison can be viewed on **HeatSourceVorticityComparisonLowSwirl.avi** (refer to attached DVD).

The addition of heat created a more solid region (approximately 400 s^{-1}) resulting in more uniformity and structure compared to the isothermal result. It was noted that the heat addition produced a more stable swirling flow, with a more prominent central core vortex that continued down to the throat. This occurred because the additional heat slowed down the cyclical regularity of the surges. Strong regions of vorticity on either side of the chamber in the top section were still prominent illustrating that the addition of heat does not add any 'strength' to the vorticity regions near the chamber wall.

6.3.8 Comparison between the Isothermal and Heat Source Simulations- Vector Velocity - Low Swirl Vane Setup

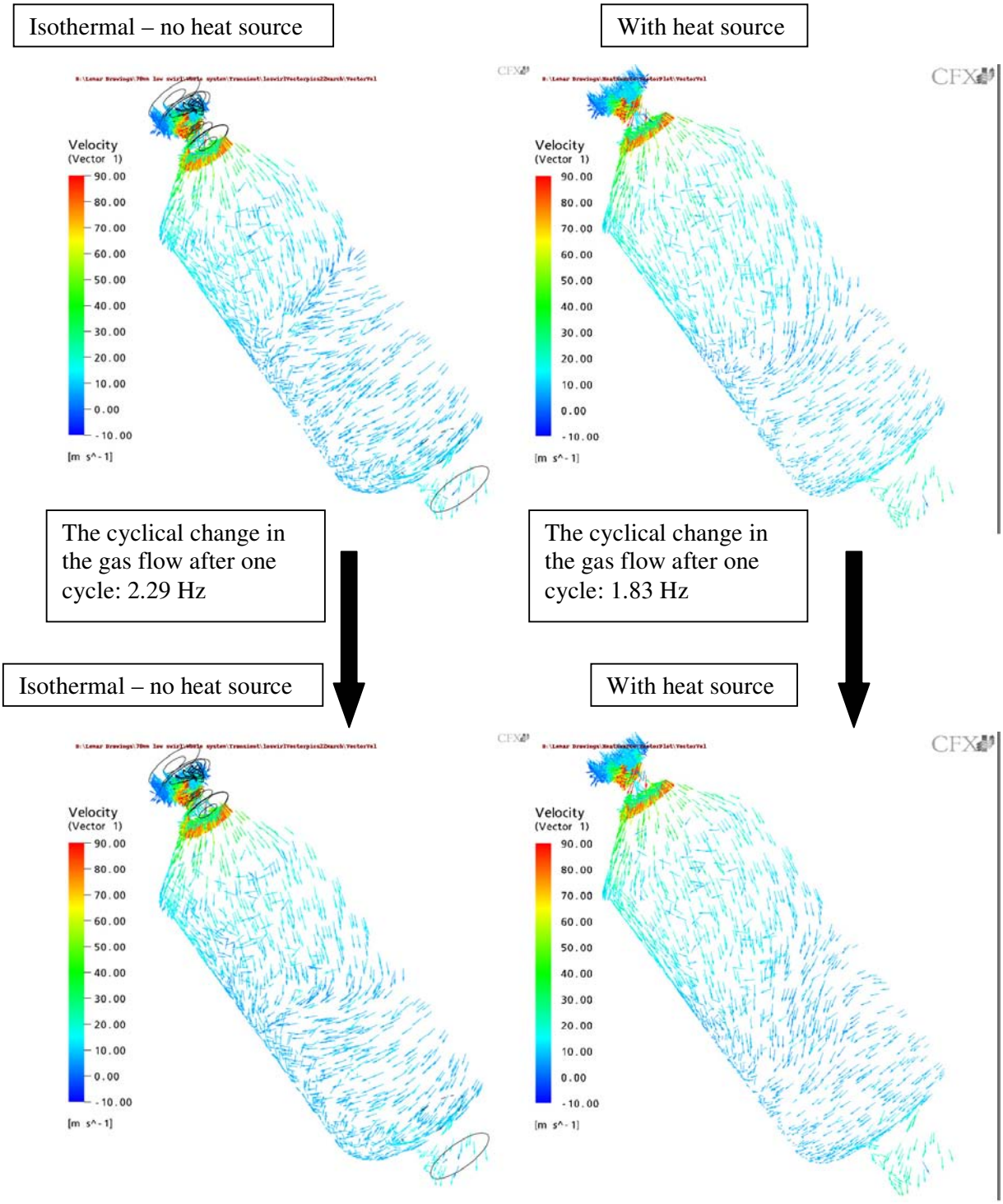

Figure 6-12: Shows one cycle for both the isothermal vector velocity (left), and heat source vector velocity (right)

Figure 6-12 compares the isothermal vector velocity and the heat source vector velocity for one cycle of the process for the low swirl vane setup. This comparison can be viewed on **HeatSourceVectorVelocityComparisonLowSwirl.avi** (refer to attached DVD).

The addition of heat lengthened the recirculation zones to include up to three quarters of the length of chamber, and produced greater variation of vector movement, compared to the more restricted vector movement in the isothermal simulation. The addition of the heat source also stabilised the swirling flow causing the frequency of the surges to decrease from 2.29 Hz to 1.83 Hz.

6.4 Discussion of the Transient Simulations for the High and Low Swirl Vane Setups

Figures 6-1 to 6-8 represent the transient results of the gas flow inside the primary combustion chamber for the isothermal temperature of 240 °C.

Figure 6-1 showed the high swirl axial profile displaying traits that have been described in previous literature, i.e. that high swirl causes a stabilising effect on the transient flow field compared to that of a low swirl setup (Swithenbank et al, 1969). This is illustrated in the 'movie' for the high swirl transient simulation which exhibited 10 cyclical surges every 7 seconds (1.43 Hz), compared to the low swirl simulation that exhibited 16 cyclical surges every 7 seconds (2.29 Hz).

Both the high swirl profile and low swirl profile (Figure 6-2) displayed traits of a vortex breakdown which is described as a **'precessing vortex core' or PVC** by Syred and Beer (1972). Both profiles indicated the presence of a distorted negative flow region resulting in a `kidney shape' recirculation zone being formed. This recirculation zone was an outcome of the imbalance between adverse pressure gradients along the jet axis and the kinetic energy of the fluid particles flowing in the axial direction (Huang and Tsai, 2001).

Figures 6-3 to 6-8 reinforced the point made above that a high swirl facilitates a more stabilising effect on the transient flow field (Swithenbank et al, 1969) in comparison to a low swirl setup. All the low swirl profiles continually pulsed and surged due to the low swirl's constant high frequency, which caused this instability.

Further CFD modelling of the primary chamber and swirl burner was undertaken with the addition of an external heat source, which resulted in the temperature rising within the chamber to 1373 °C. An energy source of 300,000 Wm^{-3} was simulated over the whole primary chamber. Figures 6-9 to 6-12 illustrated the effect of adding an external heat source to axial velocity, tangential velocity, vorticity, and vector velocity for a low swirl setup.

The addition of the external heat source stabilised the swirling flow of the profiles resulting in recirculation regions increasing and lengthening (to three quarters of the length of chamber).

In Figure 6-11 the addition of heat created a solid core that had a rotating frequency of approximately 400 s^{-1} and this had more uniformity and structure compared to the isothermal

result. There was also a more prominent central core vortex that continued down to the throat. This occurred because the heat addition associated with the low swirl slowed down the cyclical regularity of the surges. Strong regions of vorticity on either side of the chamber in the top section were still prominent, illustrating that the addition of heat did not add any 'strength' to the vorticity regions near the chamber wall.

In Figures 6-9 to 6-12 the additional heat source to the low swirl system resulted in the simulation resembling the high swirl scenario – i.e. showed a well defined, strong and symmetrical central core region of gas flow from the top of the chamber to the throat. The heat source decreased the frequency of the predicted surges (from 2.29 Hz to 1.83 Hz) and additionally caused positive surges of tangential gas flow (approximately 50 m/s) from the throat region. However, in general the additional heat source had an insignificant impact on the tangential velocity.

Based on the highly turbulent transient gas flow results obtained, the low swirl setup and the addition of an external heat source would be recommended for future modelling and running of the Lemar Plant. This recommended setup stabilised the swirling gas flow and consequently caused the recirculation zones to increase and lengthen (to three quarters of the length of chamber. A 70mm fixed sized fuel deflector cone would also be recommended as it assisted the particles to hit the wall in the top areas of the chamber (as seen in steady state in **Chapter 5 - Section 5.5.7 Comparing the Low and High Swirl Particle Tracking**).

From the steady state particle track modelling in Chapter 5 it was identified that the high swirling flow generated by the high swirl setup influenced and entrained the smaller particles (~200 μm) and forced these particles out to the sides of the chamber; whereas the low swirl setup had a limited/non-existent influence over the particles.

However as no transient CFD modelling has been undertaken to investigate the transient nature of the particle tracking and to verify that particles would stick to the furnace wall for the high or low swirl setups, no robust recommendations to the swirl vane setup and to the burner geometry can be made until further experimentation is carried out. This next phase of work would investigate transient particle tracking for both the high and low swirl setups and to use the results from the separate case study **(refer to Section 5.6.3)** to determine whether or not the dried sludge particles bounced or stuck to the viscous slag layer and their movements in the chamber.

Only the gas flow has been modelled for the high and low swirl setups and this has impacted on the aim of the Project which was to optimise the capture of the sludge particles in the slag layer by the use of CFD modelling. It was intended to use the Projects results to recommend modifications to the combustion chamber and burner geometry - specifically to those parts of the plant immediately downstream, namely the secondary chamber and the separating chamber. However as discussed above, recommendations were based solely on transient modelling of the gas flow and did not include transient modelling of the particles. Therefore further modelling is required before recommendations can be made to modify Lemar Environmental Ltd's swirl burner design and Plant equipment to enable better ash capture.

7. Conclusions and Recommendations

7.1 Overview

Lemar had concerns with the efficiency and effectiveness of the primary combustion chamber of their vitrification plant situated on the site of the Kapiti Coast Waste Water Treatment Plant. Their concerns were in relation to the inefficient capture of the particles in the slag layer of their combustion chamber.

Lemar considered that the CFD modelling undertaken by this Project would enable them to improve the functionality of this area of the plant, specifically those areas of the plant immediately downstream; namely the secondary and separating chambers. The intended outcome of the CFD modelling was to demonstrate to Lemar that it was possible to use computer generated scenarios to model variations of swirl flow generated by the burner, and particle motion within the gas flow.

Analysis of these results would indicate where modifications to the burner geometry or the chamber would improve capture.

7.2 Conclusion - Grid Independence Study

A grid independence study was undertaken to prove grid independence for the high (H 70 Series) and the low swirl vanes (L 70 Series) both using a 70 mm fuel deflector cone. For this study at least two other meshes were created – one being coarser and the other being finer than the working mesh. To check mesh independence, axial velocities across two lines were compared for the different meshes created. For both the H 70 and L 70 Series' grid independence was evident as consistent axial velocities were obtained.

Another grid independence study was undertaken using a series of meshes, the results of which were compared to a previous study by CSIRO involving the H 100 series.

An analysis of the results indicated that:

- In both models, (Figures 4-9 to 4-12) a strong region of downward flowing gas at the outer walls in the top section of the chamber was identified.

- The CSIRO model demonstrated a lower tangential velocity zone in the centre of the primary chamber compared to the recreated model.
- There was evidence of high axial velocities near the wall in the swirl vane section in both models.
- Recirculation zones in both the swirl vane section and in the primary chamber were also evident in both models.
- The tangential and axial velocity profiles taken within the annulus (Figures 4-13 and 4-14) for both models were comparable in that:
    - The tangential velocity profiles in both models resembled a "Rankine Vortex" – as indicated in Figure 3-1.
    - The tangential velocity profiles in both models tended towards zero at the axis of symmetry, which was typical of the research conducted by Wakelin (1993).
    - Both models commenced with a negative axial velocity – indicating a reversal of flow.

The variations in the outcomes of the two models were due to the CSIRO model:

- Containing more data points; and
- Using a more refined mesh to simulate the high turbulent region (the CSIRO model contained ~3,500,000 tetrahedron elements, whilst in comparison the recreated model contained ~2,500,000 elements).

7.3 Conclusion - CFD Comparison Study between the Steady State High and Low Swirl Vane Modelling Results

A CFD comparison study was undertaken between the steady state high and low swirl modelling results, at an isothermal temperature of 240 °C for the respective variables (axial velocity, tangential velocity, vorticity, vector velocity plots and particle tracking).

An analysis of the results indicated that:

- The high swirling flows from the high swirl vane setup confirmed the presence of the "Rankine Vortex".
- The high swirl tangential velocity in all the Figures illustrated that the central region in the swirl burner rotated like a solid body where the tangential velocity and radius increased.

- The high swirl results also demonstrated that the tangential velocities in the flow field were moving towards zero at the axis of symmetry.
- All the low swirl tangential velocity graphs demonstrated a resemblance of the "Rankine Vortex" apart from the low swirl tangential velocity profile in the primary combustion chamber (0.300 m below the vanes), which tended negative between approximately 0.2 and 0.25 m away from the chamber wall.
- This resulting negative tangential velocity was questionable and was considered as an effect of the unsteadiness in the solution of the low swirl setup in the primary combustion chamber (0.300 m below the vanes).
- At sufficient degree of swirl, an internal recirculation zone was generated for both the high and low swirl profiles.
- Axial velocity plots for both the high and low swirl vane setups showed traits of a **precessing vortex core' or PVC** in the primary combustion chamber. Both profiles showed the presence of a distorted negative flow region causing a `kidney shape' recirculation zone to be formed.
- The high swirling flow generated by the high swirl setup influenced and entrained the smaller particles (~200 μm) and forced these particles out to the sides of the chamber, whereas the low swirl setup had a limited/non-existent influence over the particles. The low swirl lack of influence and entrainment was demonstrated by the particles following a more rigid and straight path due to the lower swirl generated. The larger particles (~1000 μm) in both of the vane setups showed a more rigid and straight path as the particles were not entrained and influenced by the swirling gas flow.
- The Critical Stokes numbers determined for all particle diameters were less than the Stokes Number value ($St < St_c$), indicating that in theory the dried sludge particles (200 μm < d_p < 1000 μm) should stick to the furnace wall for a maximum impact velocity of 30m/s.

7.4 Conclusion - Transient Simulations for the High and Low Swirl Vane Setups

The final section of the Project entailed modelling transient simulations of the gas flow. The transient simulations possessed the same physical parameters and inputs as the steady state simulations, described in Chapter 5. A comparison took place for the high and low swirl at an isothermal temperature of 240 °C.

The main outcomes of the models were that:

- The high swirl axial profile displayed a stabilising effect on the transient flow field compared to that of a low swirl setup. All the low swirl profiles continually pulsed and surged due to the low swirl's constant high frequency, causing instability.
- Both the high swirl and low swirl profiles displayed traits of a vortex breakdown. Both profiles indicated the presence of distorted negative flow region resulting in a `kidney shape' recirculation zone being formed.

CFD modelling of the primary chamber and swirl burner also took place with the addition of an external heat source resulting in a rise in the temperature within the chamber. A simulation of the low swirl setup currently in use at Lemar was modelled. The main outcomes were that:

- The addition of the external heat source stabilised the swirling flow of the profiles resulting in recirculation regions increasing and lengthening (to three quarters of the length of chamber).
- The heat source affected the frequency of the predicted surges, decreasing them from 2.29 Hz to 1.83 Hz, causing the low swirl system to resemble the high swirl scenario – i.e. it showed a well-defined, strong and symmetrical central core region of gas flow from the top of the chamber to the throat. This occurred because the heat addition associated with the low swirl slowed down the cyclical regularity of the surges.
- With the exception of some positive surges of gas flow (approximately 50 m/s) from the throat region, the tangential velocity was not affected by the heat source.

Overall from the transient modelling of the highly turbulent gas flow, the low swirl setup with the addition of the external heat source is recommended for modelling and running the plant. This setup effectively stabilised the swirling gas flow which caused the recirculation regions to increase and lengthen (to three quarters of the length of chamber. The use of a 70 mm fixed sized fuel deflector cone is also recommended as it assisted the particles to hit the wall in the top areas of the chamber (as seen in steady state in **Chapter 5** - **Section 5.5.7 Comparing the Low and High Swirl Particle Tracking**).

Due to time constraints of this Project (Lemar wished to utilise the outcomes of this research in its forward planning commencing January 2008), no transient CFD modelling was undertaken to investigate the transient nature of the particle tracking and to verify that particles would stick to the furnace wall.

The aim of the Project was to identify the most effective setup by CFD modelling for capturing the sludge particles in the slag layer. It was hoped that these results would highlight possible modifications that could be made to the primary combustion and burner geometry (specifically to those parts of the plant immediately downstream - namely the secondary chamber and the separating chamber). Currently in practice at Lemar, the sludge particles that are not captured in the slag layer travel downstream into the separating and secondary chambers causing pressure build-ups and fouling and for the vitrification process not to function properly, resulting in the requirement to shut the plant down. Transient modelling of the particles is required before any recommendations can be made on how to modify the combustion chamber and burner geometry to enable improvements in Lemar's ash capture.

As only the gas flow has been modelled in transient mode, recommendations and suggested modifications to the burner geometry and plant equipment would need to be considered in conjunction with further experimentations on the transient particle motion in the gas flow.

7.5 Recommendations for the Project

To assist Lemar in utilising the outcomes of this research project, which is to achieve more efficient capture of particles in the slag layer of their vitrification process it is recommended that Lemar:

Recommendation 1 - Note that it is possible to use computer-generated scenarios to model variations of swirl flow generated by the burner and particle motion within the resulting gas flow.

Recommendation 2 - Note that additional refinement, in the regions of high gradient, specifically the swirler region, of the recreated model is required in order to confirm compatibility with the CSIRO model

Recommendation 3 – Note that additional CFD modelling is required to investigate transient particle tracking, as only the transient gas flow has been modelled.

Recommendation 4 – Note that the transient particle tracking results together with the results from the separate case study to investigate the previous experimentation by Davis et al (1986 and 2002) would provide an overall interpretation of the particle motion within the gas flow and

confirm whether or not the dried sludge particles bounced or stuck to the viscous slag layer and their movements were able to be tracked in the chamber.

Recommendation 5 – Undertake an analysis of the transient particle tracking results to determine where possible modifications to the burner geometry and plant equipment would occur, the outcome of which would improve the ash capture for the Lemar Vitrification Process.

Recommendation 6 – Include in the scope of any additional modelling a review, which validates this CFD project. This would be done by undertaking a series of practical experiments inside the primary combustion chamber at the Lemar Plant to obtain Pitot tube measurements (without particles or combustion), which would indicate the CFD model's performance to capture the length of the vortex and the strength of the recirculation.

Recommendation 7 – Include the effects of the particle combustion in CFD modelling.

Recommendation 8 – Further investigate the grid independence study for the modelling undertaken by CSIRO (H 100 Series).

8 References

Abrahamson, J. (1981). Mechanisms of dust collection in cyclones. Christchurch. (Chapter only)

Anon. (2005). "Ansys CFX Release 10.0 Documentation." from www.ansys.com/cfx.

Borzone, L. A., G. E. Klinzing, et al. (1990). "Energy losses and particle--wall interactions on rough surfaces." Powder Technology 62(3): 277-290.

Boysan, F., R. Weber, et al. (1986). "Modelling Coal-Fired Cyclone Combustors." Combustion and Flame 63(1-2): 73-86.

Chanaud RC. Observations of oscillatory motion in certain swirling flows. J Fluid Mech 1965; 21:111-27.

Davis, R. H., Serayssol, J.-M. & Hinch, E. J. 1986 The elastohydrodynamic collision of two spheres. J. Fluid Mech. **163**, 479{497.

Davis, R. H., D. A. Rager, et al. (2002). "Elastohydrodynamic rebound of spheres from coated surfaces." Journal of Fluid Mechanics **468**: 107-119.

Dobbs, R. (2003). "LEMAR Environmental."

Dobbs, R. (2006). Technical Report 14/03/06. Christchurch, New Zealand, Lemar Environmental Ltd.

Dorgan, A. J. and E. Loth (2004). "Simulation of particles released near the wall in a turbulent boundary layer." International Journal of Multiphase Flow 30(6): 649-673.

Froud DY, Beale AJ, O'Doherty T, Syred N. Studies of Helmholtz resonance in a swirl burner furnace system. 26th International Symposium on Combustion, 1996. pp. 3355-62.

Ganesan V., Recirculation and turbulence studies in an isothermal model of a gas turbine combustor chamber, Ph.D. Thesis, I.I.T.-Madras-Chennai, India, 1974

Gondret, P., Lance, M. & Petit, L. 2002 Bouncing motion of spherical particles in fluids. Phys. Fluids **14**, 643{652.

Gorham, D. A. and A. H. Kharaz (2000). "The measurement of particle rebound characteristics." Powder Technology 112(3): 193-202.

Gupta AK, Lilley DJ, Syred N. Swirl flows. Tunbridge Wells, UK: Abacus Press; 1984.

Gupta, R. P., T. F. Wall, et al. (1998). "Computer-controlled scanning electron microscopy of minerals in coal--Implications for ash deposition." Progress in Energy and Combustion Science 24(6): 523-543.

Hartman, M., K. Svoboda, et al. (2005). "Combustion of dried sewage sludge in a fluidized-bed reactor." Industrial & Engineering Chemistry Research 44(10): 3432-3441.

Harvey JK. Some observations of the vortex breakdown phenomenon. J Fluid Mech 1962; 14:585-92.

Hii, M. J. W. (2004). Kiwifruit Flower Pollination. University of Canterbury, Chemical and Process Engineering Department. Christchurch, University of Canterbury.

Huang R.F., Tsai F.C. Observations of swirling flows behind disks, AIAA Journal 39 (2001) 1106-1112

Hussainova, I., J. Kubarsepp, et al. (1999). "Investigation of impact of solid particles against hardmetal and cermet targets." Tribology International 32(6): 337-344.

Joseph, G. G., Zenit, R., Hunt, M. L. & Rosenwinkel, A. M. 2001 Particle{wall collisions in a viscous fluid. J. Fluid Mech. **433**, 329{346.

Kaftori, D., G. Hetsroni, et al. (1998). "The effect of particles on wall turbulence." International Journal of Multiphase Flow 24(3): 359-386.

Leibovich, S., 1978. Structure of vortex breakdown. Annual Review of Fluid Mechanics 10, 221–246.

Lucca-Negro O. Modelling of swirl flow instabilities. PhD thesis, University of Wales, UK, 1999.

Miles, T. R., L. L. Baxter, et al. (1995). Alkali Deposits Found in Biomass Power Plant: A Preliminary Investigation of their Extent and Nature.

Mueller, C., M. Selenius, et al. (2005). "Deposition behaviour of molten alkali-rich fly ashes-development of a submodel for CFD applications." Proceedings of the Combustion Institute 30(2): 2991-2998.

Nguyen, A. V. and C. A. J. Fletcher (1999). "Particle interaction with the wall surface in two-phase gas-solid particle flow." International Journal of Multiphase Flow 25(1): 139-154.

O'Doherty T, Griffiths AJ, Syred N, Bowen PJ, Fick W. Experimental analysis of rotating instabilities in swirling and cyclonic flows. DCEMP 1998;7(3/4):245-68.

Ranz, W. E., G. R. Talandis, et al. (1960). "Mechanics of Particle Bounce." A.I.Ch.E. Journal.

Rhie, C. M. and W. L. Chow (1983). "Numerical study of the turbulent flow past an airfoil with trailing edge separation." AIAA J(21): 1527-1532.

Sarpkaya T. On stationary and travelling vortex breakdowns. J Fluid Mech 1971; 45(3):545-59.
Stephens, D. W. (2006). CFD Modelling of Lemar Sludge Vitrification - Stage 1. Melbourne, CSIRO Minerals.

Saruchera, T. (1998). Measurement and Modelling of Particle Residence Time in a Return-Flow Cyclone. Department of Chemical and Process Engineering. Christchurch, University of Canterbury.

Swithenbank J, Chigier NA. Vortex mixing for supersonic combustion. 21st International Symposium on Combustion, 1969. p. 1154-62.

Syred N, Beer JM. Combustion in swirling flows: a review. Combust Flame 1974; 23:143–201.

Syred N, Beer JM. The damping of precessing vortex cores by combustion in swirl generators. Astronautica Acta 1972; 17:783-801.

Syred N, Fick W, O'Doherty T, Griffiths AJ. The effect of the precessing vortex core on combustion in a swirl burner. Combust Sci Tech 1997; 125:139-57.

Syred N, Hanby VI, Gupta AK. Resonant instabilities generated by swirl burners. J Inst Fuel 1973:402-7.

Versteeg, H. and W. Malalasekera (1995). An introduction to computational fluid dynamics: the finite volume method. New York, Longman Scientific & Technical.

Vonnegut RC. Experiments concerning the vortex whistle. J Acoust Soc Am 1954; 35:933-8.

Wakelin, R. F. (1993). Vortex Breakdown in dust collecting return-flow cyclones. Department of Chemical and Process Engineering. Christchurch, University of Canterbury.

Wang, H. and J. N. Harb (1997). "Modeling of ash deposition in large-scale combustion facilities burning pulverized coal." Progress in Energy and Combustion Science **23**(3): 267-282.

Wang, X. H., D. Q. Zhao, et al. (2007). "Modeling of a coal-fired slagging combustor: Development of a slag submodel." Combustion and Flame **149**(3): 249-260.

Weber R, Boysan F, Swithenbank J, Roberts PA. Computation of near field aerodynamics of swirling expanding flows. 21st International Symposium on Combustion,1986. p. 1435-43.

Zhou, H., P. A. Jensen, et al. (2007). "Dynamic mechanistic model of superheater deposit growth and shedding in a biomass fired grate boiler." Fuel 86(10-11): 1519-1533.

9 Appendices

Appendix 9.1 Spreadsheet to determine the Stokes Number, Critical Stokes Number and the Elasticity Parameter for a particle impacting a wet viscous wall surface

Spreadsheet to determine the Stokes Number, Critical Stokes Number and the Elasticity Parameter for a particle impacting a wet viscous wall surface
Author: David Walker

Furnace at 1100 ℃

Stokes number calculation (St Number)

Calculating the viscosity of the slag

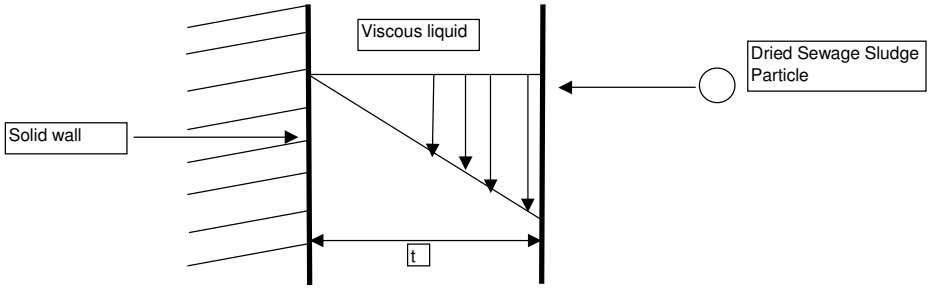

radius of particle	**a**	0.0005000	m	
density of particle	**ρ_s**	1200.000	kg/m^3	
gravity	**g**	9.810	ms^{-2}	
mass flow slag	**$m_{particle}$**	0.0038000	kg/s	
volumetric flow rate of slag	**Q_{slag}**	0.0000032	m^3/s	
volumetric flow rate per metre	**$Q_{per\ m}$**	0.0000017	m^2/s	$Q_{per\,m} = \frac{\rho g}{\mu}\frac{t^3}{3}$
diameter of chamber	**D**	0.600	m	
circumference of chamber	**Circ**	1.885	m	
area	**area**	0.003769911	m^2	$Vel_{avg} = \frac{Q_{slag}}{area}$
average velocity (at centre of film)	**Vel_{avg}**	0.0008400	m/s	
fluid viscosity	**μ**	18.6860608	Pa.s	$\mu = \frac{\rho g}{Q_{per\,m}}\frac{t^3}{3}$
mass of particle	**m**	0.0000006	kg	$m = 4\pi a^3 \rho_s / 3$
impact velocity	**Vo**	30.0000000	m/s	
Stokes Number	**St**	0.21406		$St = mv_o/(6\pi\mu a^2)$

Elasticity parameter calculation (ε)

fluid viscosity	**μ**	18.68606	Pa.s	
radius of particle	**a**	0.00050	m	
impact velocity	**Vo**	30.00000	m/s	
	Xo	0.00200		
Young's Modulus for particle (fly ash)	**E_1**	8.20E+10	Pa	Elastic constants at 1100 ℃
Young's Modulus for soda-lime glass	**E_2**	2.51E+10	Pa	
Poission Ratio for particle (fly ash)	**v_1^2**	0.098596		
Poission Ratio for soda-lime glass	**v_2^2**	0.0484		
	θ	1.55689E-11		$\theta = (1-v_1^2)/(\pi E_1) + (1-v_2^2)/(\pi E_2)$
	ε	6.01239E-06		$\varepsilon = 4\theta\mu v_o a^{3/2} / x_o^{5/2}$
	1/ε	166323.3154		

Critical Stokes Number (St_c)

Critical Stokes Number (St_c)	**St_c**	4.608675543	$St_c = 0.4\ln(1/\varepsilon) - 0.20$